Optical quantification of multiphase flow near a hydrogen-evolving electrode

Master of Science Thesis

H.W. Haverlag

Delft University of Technology

TU Delft

This page is intentionally left blank

Optical quantification of multiphase flow near a hydrogen-evolving electrode

MASTER OF SCIENCE THESIS

For obtaining the degree of Master of Science
at the Delft University of Technology

H.W. Haverlag

September 22, 2023

Faculty of Mechanical Engineering · Delft University of Technology

TU Delft

The work in this thesis was supported by the Process and Energy section at the faculty of Mechanical Engineering at Delft University of Technology. Their cooperation is gratefully acknowledged.

DELFT UNIVERSITY OF TECHNOLOGY
FACULTY OF MECHANICAL, MARITIME AND MATERIALS ENGINEERING
DEPARTMENT OF PROCESS AND ENERGY

GRADUATION COMMITTEE

Dated: September 22, 2023

Committee members:

Dr.Ir. G.E. Elsinga

Supervisor: Dr.Ir. J.W. Haverkort

Dr. A. Laskari

Abstract

In this research project, multiphase behaviour in zero gap alkaline water electrolyzers is investigated, focusing on the influence of various parameters including current density, electrode-wall distance and electrode height. This involves a cell containing a vertical electrode pair separated by a membrane submerged in an electrolyte that has a liquid-air interface near the top of the electrodes. The study aims to identify and understand turbulent phenomena through different analysis methods. Additionally, the outcomes derived from the conducted experiments serve as validation data for concurrent modeling research. The analysis begins by examining vortex formation on the cathodic side, where hydrogen bubbles originate, using Particle Image Velocimetry (PIV). The results indicate the presence of bubble vortices, especially near the top of the channel. At electrode-wall distances of 1.0 cm or more, the bubbles that fail to reach the liquid-air interface tend to circulate extensively within the channel without exhibiting any noticeable discrepancies, such as small vortices. It should be noted that some low-velocity vortices, typically on the order of millimeters per second, can be observed within the bulk of the channel. As a general rule, shorter electrode-wall distances lead to increased vortex formation throughout the entire channel. Additionally, higher current densities induce a greater amount of these vortices or chaotic and irregular motion of the bubbles in the bulk region. In modern configurations, elastic elements, such as materials of thin wires with high porosity and low solid volume fraction, are strategically incorporated into the electrolyzer design to enhance mechanical resilience and accommodate variations in pressure and temperature. These elements serve to ensure the stability and reliable performance of the electrolyzer system under diverse operational conditions. Much of the chaotic behaviour of the bubbles seems to be counteracted when the electrode-wall distance is large (1.5 cm) while an elastic element is placed in between the cathode and opposing wall. When the whole channel is filled by the elastic element (0.6 cm electrode-wall distance), this results in more small-velocity vortices than without the element.
Another examined phenomenon is the presence of a bubble mist. This mist arises when the bubbles that originate at the electrode do not escape the channel at the liquid-air interface, but recirculate towards the opposing wall and downwards from there. Light intensity coming from the bubble clouds is used to gain and calibrate results. Increasing the current density and decreasing the electrode-wall distance lead to deeper bubble mist plumes. Surprisingly, elevated electrolyte height directly influences mist depth, with larger electrolyte heights showing the highest mist depths, even when dividing these by the exposed electrode height. For these measurements, diamond shaped apertures on the electrodes are used. For another series of experiments where higher current densities are examined, slotted apertures are used and the effect of lowering the electrode-wall distance on the bubble mist depth is diminished. Whether this is due to the type of electrodes or the different measurement circumstances (for example lighting) can not be concluded from the results. This emphasizes the need for consistent experimental conditions.
Thirdly, the continuous release and upward movement of gas bubbles originating at the cathode, i.e. the bubble plumes, are investigated. The effect of changing the current density is investigated along different heights of the electrodes. The analysis performed employs three different strategies to assess turbulent behaviour. This includes the PIV method used initially to depict vortices, the light intensity coming from the bubble clouds and visual analysis to find discrepancies like bubble bursts and big bubble trajectories. The PIV method shows capabilities in tracking the plume width and depicting turbulent behaviour. The light intensity analysis however proves challenging due to disparities in lighting. Improved lighting and higher-resolution cameras could yield more reliable results, enabling further investigation into correlations between parameters and turbulence, such as bubble bursts.

Preface

Dear reader,

I am hugely grateful for all the support and contributions that have made this research endeavor a truly enriching journey. It is with pleasure and great appreciation that I extend my gratitude to the members of the J. Willy Bubble Brigade, the research group I have been part of for the last nine to ten months, for their unwavering commitment and collaboration. First and foremost, I want to express my appreciation to my supervisor, J.W. Haverkort, whose guidance and encouragement have been inspiring. Our discussions in his office were enlightening, and a source of inspiration and ideas. I would also like to extend my sincerest thanks to my friends and family for their support during this journey. Their emotional encouragement provided the strength to persevere when times seemed challenging. Special acknowledgment goes to my girlfriend, who, despite not always fully grasping the complexities of my work, was a constant source of enthusiasm and support, cheering me on every step of the way. Furthermore, I wish to express my gratitude to all the remarkable PhD students and Post Docs, both within and outside the lab, for their expertise and camaraderie. Your guidance and willingness to engage in stimulating discussions have been a key factor in shaping this research project. Special thanks to PhD student Nikhilesh Kodur Venkatesh for discussions and giving feedback on written work. I would like to thank fellow Msc-student Emile Craye for taking time to help with the PIV script and the fun times gossiping in the lab. Thanks to Gilles, Mehmet, Kris, Dirk and Lotte for spending time in the lab with me and (to different extents) helping me with keeping the spirits high. The weekly meetings with the research group were not only enlightening but also created a strong sense of unity and shared purpose. I value the bonds created during these interactions and am grateful for the collaborative spirit.

In conclusion, I am pleased to have been surrounded by such a remarkable group throughout this journey.

Delft University of Technology — Hein Haverlag
September 22, 2023

List of Figures

2.1 Conductivity of aqueous solutions of KOH for different temperatures and weight percentages (wt.%) KOH . Data from 4

2.2 By systematically targeting individual contributions to cell voltage, a methodical approach is enabled for reducing the overall cell voltage. This technique enables a specific focus on each contribution, thereby facilitating the implementation of highly effective voltage reduction strategies. From 5

2.3 Electrochemical Tafel slope showing the relationship between overpotential and current density (logarithmic scale). Adapted from 5

2.4 Schematic representation of alkaline water electrolyser with traditional non-zero gap (left) and the modernly used zero-gap (right) configuration. From 7

2.5 Schematic representation of alkaline water electrolyser with elastic element between wall/bipolar plate and electrodes. From 7

2.6 (1) Bubbly, (2) slug, (3) churn-turbulent, (4) annular drop and (5) falling film flow regimes for two-phase flows. From 8

2.7 Left: Bubble trajectory wavelength (a) and mean vertical rise velocity (b) of larger ($d_b >$ 1.5 mm) bubbles. Right: Trajectory multiple large bubbles. From 9

2.8 Electrodes in traditional configuration, where the diaphragm splits two channels. From . . 10

2.9 Mass transfer coefficient versus cell gap. Different effects of convection induced by bubbles while varying gap are visible. From 11

2.10 Theoretical transition height from laminar to turbulent flow along two parallel vertical plates for different temperatures of 1M KOH electrolyte and bubbles with 50 micron diameter. See eq. (2.12). The value for dynamic viscosity μ is 1.5713 $\cdot 10^{-3}$ Pa·s and a density of 1307.2 kgm^{-3}. Data from 13

2.11 Evolution of turbulent intensity within the bubble layer along the cathode length for three distinct current densities: $j = 500$ (◆), 1000 (■), and 2000 (▲) A/m^2, within a Na_2SO_4 solution (50 g/l). The turbulent intensity at the channel center is provided for the current density $j = 1000$ A/m^2 (╳), while vertical solid lines demarcate the positions of the channel's inlet and outlet. From 13

2.12 Transitional range $Gr_x \cdot Pr$ versus angle. From 14

2.13 Transitional height versus height based on critical Archimedes number for bubbles with 50 microns diameter. Based on 15

2.14 Schematically, the change of velocity gradients at the boundary layer between bubble plume and liquid ($y = \delta$) and at the wall opposite to the gas-evolving electrode ($y = s$). From 16

2.15 (a): The velocity and void fraction profiles for the quasi-steady regime. (b): Liquid velocity and void fraction in the quasi-turbulent regime . Both single channel. 17

2.16 Theoretical transition point according to Alexiadis to pseudo-turbulence and quasi-steady regime for current density versus electrode-wall distance for 1M KOH solution. For a temperature of roughly 25 °C, the value for dynamic viscosity μ is 1.5713 $\cdot 10^{-3}$ mPa·s and a density of 1307.2 kgm^{-3} is used. It should be noted that a hydrogen bubble diameter of 50 microns is assumed. 18

2.17 A hydrogen bubble curtain near the electrode. A zoomed sequence shows the coalescence occurring between 22 ms and 23 ms. At the right, the velocity profile mirrors the wavy profile of the curtain. From 18

2.18 Schematic overview of observed bubble envelope shapes for small cell gap of < 4 mm (left) and bigger cell gaps of 8 mm (right). From 19

3.1 Overview types of phenomena researched during the research project with (a) vortices observable at different heights along the channel, (b) the mist cloud reaching a certain depth inside the channel in fully developed state (60 seconds after applying current), and (c) a bubble plume originating at the cathode, filmed with a high speed camera. 22

4.1 Overview of experimental setup. 24

4.2 Elastic element used in channel in between cathode and opposing wall. 26

5.1 Cathodic side. 500 A/m^2. Captured at a frame rate of 1000 fps. Electrode-wall distance = 1 cm. Zp200705 electrode. 60 seconds after startup. Stokes velocity subtracted. 30

5.2 Cathodic side. From left to right: 200, 400, 800 and 1600 A/m^2. Electrode-wall distance 0.5 cm. The electrolyte level at 7.5 cm. Zp200705 electrode. 60 seconds after applying current. 31

5.3 Cathodic side. Left to right: 100, 500, 1100, 1900 A/m^2. The electrolyte level at 7.5 cm. Electrode-wall distance 1.0 cm. Zp200705 electrode. 60 seconds after applying current. . 32

5.4 Cathodic side. 200, 400, 800, 1600 A/m^2. Electrode-wall distance 1.5 cm. The electrolyte level at 10.0 cm. Zp200736 electrode. 33

5.5 Cathodic side with elastic element attached to electrode at 200, 400, 800, 1600 A/m^2. Electrode-wall distance 1.5 cm. The electrolyte level at 10.0 cm. Zp200736 electrode. . . 34

5.6 Cathodic side. 1600 A/m^2. Electrode-wall distance 0.6 cm. Bubble encountering elastic element in bottom of channel. 36

5.7 Cathodic side. Five different time stamps with big bubble propagating trough the channel upwards (left in figure). 1600 A/m^2. Electrode-wall distance 0.6 cm. 20 frames (0.02 seconds) in between successive frames. Zp200736. 37

5.8 Cathodic side. Five different time stamps with big bubble propagating trough the channel upwards (left in figure). 1600 A/m^2. Electrode-wall distance 0.6 cm. 20 frames (0.02 seconds) in between successive frames. Effect on velocity field visible. Zp200736. . . . 37

5.9 Cathodic side. Typical bump against elastic element. Current density of 1000 A/m^2. Large electrode-wall distance to have clear view of elastic element effect. Zp200736 electrode. 38

5.10 Cathodic side. Fully developed electrolysis, from left to right, 100 - 600 A/m^2. Electrode-wall distance 1.2 cm. Electrolyte height 14.5 cm. Zp200699 electrode. 60 seconds after applying current. Red dots denote centimeters. 39

5.11 Cathodic side. Intensity overview of fully developed electrolysis, 100 - 600 A/m^2 with contour lines. Zp200699 electrode. Electrolyte height 14.5 cm. 60 seconds after applying current. 40

5.13 Comparison for lower current densities up to 600 A/m^2 (a) and higher current densities to 1600 A/m^2 (b). The ratio of the maximum depth divided by the channel depth is provided next to the respective value. 41

5.12 Mist heights for the different electrode-wall distances 1.0 - 2.4 cm, different electrolyte heights (9 - 14.5 cm) for a range of current densities. The electrode is placed on the bottom of the cell. 41

5.14 Zp200699 cathode. Irregularities in the form of bubble bursts at different heights along the cathode at 550 A/m^2. A large bubble ($\sim$ 2.1 mm) trajectory is shown in (c). Time between first and last frame equals 0.15 seconds 43

5.15 Cathodic side. Bubble plume when using the average light intensity over a whole 0.6 second movie. Electrode-wall distance large ($\sim$ 3 cm) to prevent back-flow interference. Zp200699 electrodes. 44

5.16 Cathodic side. Bubble plume PIV. Current densities of 200 (left) and 550 (right) A/m^2. Electrode-wall distance large ($\sim$ 3 cm) to prevent back-flow interference. Zp200699 electrodes. 45

A.1 Gas evolution in channels. Anodic (electrode-wall distance 6 mm) and cathodic (electrode-wall distance 5 mm) side at the left and right of the membrane respectively. Current densities of 100 (left), 1000 (middle) and 6000 A/m^2. 54

A.2 Gas fraction ε for a range of current densities of 0 to 6000 A/m^2. Gas fraction values given at different j. 55

B.1 Veco Samples properties 57

C.1 Cathodic side. Average vector field 500 A/m^2. Captured at a frame rate of 1000 fps. Gap to wall = 1 cm. No subtraction Stokes velocity 59

C.2 Cathodic side. Average vector field 500 A/m^2. Captured at a frame rate of 1000 fps. Gap to wall = 1 cm. Stokes velocity subtracted. 59

C.3 Average vector field 400 A/m^2. Captured at a frame rate of 30 fps. The red lines denote the location of the wall (top) and the cathode (red). Velocities are also notable below the cathode as also a small portion of the anodic side is filmed. The electrolyte level was at 105 mm. 60

C.6 Cathodic side. Left: 500 A/m^2. Right: 1100 A/m^2. Electrode-wall distance 1.0 cm. The electrolyte level at 7.5 cm. Zp200705 electrode. Lower area highlighted. Different movement patterns visible. 60

C.4 Cathodic side. Left: 200 A/m^2. Right: 400 A/m^2. Electrode-wall distance 0.5 cm. The electrolyte level at 7.5 cm. Zp200705 electrode. Additionally, the results without color map are given. 61

C.5 Cathodic side. Left: 800 A/m^2. Right: 1600 A/m^2. Electrode-wall distance 0.5 cm. The electrolyte level at 7.5 cm. Zp200705 electrode. Additionally, the results without color map are given. 62

C.7 Cathodic side. 800 A/m^2. No elastic element. Electrode-wall distance 1.5 cm. 60 seconds after applying current. 63

C.8 Cathodic side. From left to right: 200, 400, 800, 1600 A/m^2. No elastic element. Electrode-wall distance 0.6 cm. 60 seconds after applying current. 64

C.9 Cathodic side. From left to right: 200, 400, 800, 1600 A/m^2. Elastic element. Electrode-wall distance 0.6 cm. 60 seconds after applying current. 65

C.10 Cathodic side. 400 A/m^2. Left: no elastic element. Right: elastic element. Electrode-wall distance 0.6 cm. 60 seconds after applying current. 66

C.11 Cathodic side. Elastic element. Left: 400 A/m^2. Right: 800 A/m^2. Electrode-wall distance 0.6 cm. 60 seconds after applying current. 67

C.12 Cathodic side. Elastic element. 800 A/m^2. Left: 50 microns diameter bubbles. Right: 100 microns diameter bubbles. Electrode-wall distance 0.6 cm. 60 seconds after applying current. Stokes velocity 4x higher for 100 microns. Clear effect on the vectors. Vortices still visible. Centre of vortices depicted in green. 68

E.1 Bubble plume 20, 70, 200, 550 A/m^2. Electrode height 2-5 cm. 76

E.2 Bubble plume 20, 70, 200, 550 A/m^2. Electrode height 5-8 cm. 77

E.3 Bubble plume 20, 70, 200, 550 A/m^2. Electrode height 8-11 cm. 78

E.4 Bubble plume 20, 70, 200, 550 A/m^2. Electrode height 11-14 cm. 79

E.5 Bubble plume 20, 70, 200, 550 A/m^2. Electrode height 14-17 cm. At the top, one of the bolts connecting the cathode to the membrane and anode is visible. 80

List of Tables

4.1 Veco electrode properties. 23

4.2 Maximum current densities Veco samples. 23

4.3 Configuration analysed with PIV. 25

4.4 Configuration analysed with PIV. This configuration is analysed for an elastic element attached to the cathode and a regular cathodic side. 25

4.5 Configurations Veco zp200699 and zp200736 for mist depth analysis 26

List of Symbols

Latin symbols

Symbol	Definition	Unit
°C	Degree Celsius	-
c	Concentration	mol/L
d, d_b	Bubble Diameter	m
D_b	Hydrodynamic Dispersion Coefficient	m^2/s
E_0	Standard Cell Potential	V
F	Faraday's Constant, 96,487	$\mathrm{A} \cdot \mathrm{smol}^{-1}$
g	Gravitational Acceleration Earth	$\mathrm{m/s}^2$
G_0	Gibbs Free Energy	kJ/mol
h	Electrode Height	m
I	Current	A
i_0	Exchange Current Density	$\mathrm{A/m}^2$
j	Current Density	$\mathrm{A/m}^2$
l	Channel Thickness	m
L	Height	m
M	Molecular Mass Gas	u
n	Number of Electrons in Reaction	-
Q_gas	Volume Flow Rate	m^3/s
$\mathcal{R}$	Universal Gas Constant, 8.31446	$\mathrm{J} \cdot \mathrm{K}^{-1} \cdot \mathrm{mol}^{-1}$
r	Bubble Radius	m
R	Resistance	Ω , $\frac{\mathrm{kg} \cdot \mathrm{m}^2}{\mathrm{s}^3 \cdot \mathrm{A}^2}$
T	Temperature	K, °C
u_gas	Interstitial gas Velocity	m/s
U_gas	Superficial Gas Velocity	m/s
v	Velocity	m/s
V	Volume	m^3
w	Electrode-wall Distance	m
w_e	Width Electrode	m
wt.%	Weight Percentage	%
z	Number of Electrons in Reaction	-
Ar	Archimedes Number	
Fr	Froude Number	
Gr	Grashof Number	
Pr	Prandtl Number	
Pr_α	Prandtl-equivalent Number	
Ra	Rayleigh Number	
$\mathrm{R}\alpha_\mathrm{f,e}$	Rayleigh-equivalent Number	
Re	Reynolds Number	
Sc	Schmidt Number	

Greek symbols

Symbol	Definition	Unit
α	Charge Transfer Coefficient	
β	Volumetric Dispersion Coefficient	
η	Overpotential	V
ε	Volume Fraction Gas	
κ_d	Local Mass Transfer Coefficient	
λ	Wavelength	m
μ	Dynamic Viscosity	Pa·s, $\frac{\text{kg}}{\text{m·s}}$
ν	Kinematic Viscosity	$\frac{\text{m}^2}{\text{s}}$, $\frac{\text{N·m}}{\text{kg}} \cdot \text{s}$
ρ	Density	$\text{kg} \cdot \text{m}^{-3}$
τ	Viscous Stress	Pa, N/m^2

Contents

Preface vii

List of Figures ix

List of Tables xiii

List of Symbols xv

List of Symbols xix

1 Introduction 1

2 Theory and Literature Review 3

2.1 Hydrogen from Electrolysis . . . 3

2.1.1 Basic Concepts Alkaline Water Electrolysis . . . 3

2.1.2 Cell configurations . . . 6

2.2 Hydrogen production performance . . . 7

2.2.1 Bubbles in alkaline water electrolysers . . . 8

2.2.2 Bubbles in electrolysers . . . 8

2.2.3 Mass transfer and bubble influence . . . 9

2.3 From laminar to turbulent flow . . . 11

2.3.1 Theoretical transition laminar-turbulent flow . . . 11

2.3.2 Experimental results turbulent flow . . . 12

2.4 Backflow and Vortex Formation . . . 15

2.5 Wavy Bubble Plume . . . 18

3 Research Project 21

4 Methods 23

4.1 Data Analysis . . . 24

4.2 Vortex formation . . . 25

4.3 Mist height versus electrode-wall distance, electrode height and current density . . . 26

4.4 Bubble Plume Analysis . . . 27

5 Results 29

5.1 Vortex formation . . . 29

5.1.1 Zp200705 . . . 29

5.1.2 Elastic element . . . 32

5.2 Mist height versus electrode-wall distance, electrode height and current density . . . 39

5.3 Bubble Plume Analysis . . . 42

6 Conclusions and Discussion 47
6.1 Conclusions 47
6.2 Discussion and Further Research 48

Appendices 51

A Gas Fraction 53

B Veco Samples 57

C Vortex Analysis 59

D Mist Height Analysis 69

E Bubble Plume Analysis 75

Bibliography 81

List of Symbols

Latin symbols

Symbol	Definition	Unit
°C	Degree Celsius	-
c	Concentration	mol/L
d, d_b	Bubble Diameter	m
D_b	Hydrodynamic Dispersion Coefficient	m^2/s
E_0	Standard Cell Potential	V
F	Faraday's Constant, 96,487	$\mathrm{A} \cdot \mathrm{smol}^{-1}$
g	Gravitational Acceleration Earth	$\mathrm{m/s}^2$
G_0	Gibbs Free Energy	kJ/mol
h	Electrode Height	m
I	Current	A
i_0	Exchange Current Density	$\mathrm{A/m}^2$
j	Current Density	$\mathrm{A/m}^2$
l	Channel Thickness	m
L	Height	m
M	Molecular Mass Gas	u
n	Number of Electrons in Reaction	-
Q_gas	Volume Flow Rate	m^3/s
$\mathcal{R}$	Universal Gas Constant, 8.31446	$\mathrm{J} \cdot \mathrm{K}^{-1} \cdot \mathrm{mol}^{-1}$
r	Bubble Radius	m
R	Resistance	Ω , $\frac{\mathrm{kg} \cdot \mathrm{m}^2}{\mathrm{s}^3 \cdot \mathrm{A}^2}$
T	Temperature	K, °C
u_gas	Interstitial gas Velocity	m/s
U_gas	Superficial Gas Velocity	m/s
v	Velocity	m/s
V	Volume	m^3
w	Electrode-wall Distance	m
w_e	Width Electrode	m
wt.%	Weight Percentage	%
z	Number of Electrons in Reaction	-
Ar	Archimedes Number	
Fr	Froude Number	
Gr	Grashof Number	
Pr	Prandtl Number	
Pr_α	Prandtl-equivalent Number	
Ra	Rayleigh Number	
$\mathrm{R}\alpha_\mathrm{f,e}$	Rayleigh-equivalent Number	
Re	Reynolds Number	
Sc	Schmidt Number	

Greek symbols

Symbol	Definition	Unit
α	Charge Transfer Coefficient	
β	Volumetric Dispersion Coefficient	
η	Overpotential	V
ε	Volume Fraction Gas	
κ_d	Local Mass Transfer Coefficient	
λ	Wavelength	m
μ	Dynamic Viscosity	Pa·s, $\frac{\text{kg}}{\text{m·s}}$
ν	Kinematic Viscosity	$\frac{\text{m}^2}{\text{s}}$, $\frac{\text{N·m}}{\text{kg}} \cdot \text{s}$
ρ	Density	$\text{kg} \cdot \text{m}^{-3}$
τ	Viscous Stress	Pa, N/m^2

1 Introduction

Energy is in constant need of efficiency improvement. Growth of population, living standards and therefore increased consumption mean that current energy sources can not deliver enough to facilitate our needs and more importantly, not in the green manner we strive towards. In 2015, to battle climate change, many governmental bodies agreed to achieve a reduction of 45% carbon emissions by 2030 and reach net zero by 2050 [1]. Because of the growing contribution of intermittent energy sources as solar and wind energy, storage is more important than ever. Batteries, hydro-pumped energy storage and other conventional methods normally lead to solid short-term storage while seasonal energy surpluses (think of solar energy in summer months) can not be covered by these techniques in a sufficient manner. Chemical bonds are well known to have great potential in terms of long term production and therefore seem to be a solution for these storage issues. Hydrogen is a commonly used chemical element in numerous applications because of its high energy-to-weight ratio, namely a Lower Heating Value (LHV) of 120 MJ kg^{-1} and an Upper Heating Value (UHV) of 142 MJ kg^{-1} [2]. As the byproduct created during production is oxygen without any carbon emissions [3], water electrolysis is an attractive option for reducing greenhouse gas emissions, fulfilling our storage needs and powering applications for vehicles. Hydrogen is considered an affordable, secure and versatile form of energy carriage and usage. However, hydrogen energy faces many challenges like efficiency losses and therefore additional production costs [4]. Although significant research has been conducted on hydrogen energy, there are still many unknowns regarding its full potential.

Alkaline Water Electrolysis (AWE) is one technique that produces hydrogen and oxygen from an alkaline solution and electricity. This technique is favourable because it utilizes water, which is renewable and abundant, as a source of hydrogen. Additionally, electrolysis can be powered by renewable energy sources such as wind or solar, making it a carbon-free process.

The aim of this research project is to quantify and visualize flow patterns inside alkaline water electrolysers. Especially, the transition to turbulence while varying configuration parameters is a concept which is vital to get understanding of. When researchers are able to model flow patterns accurately inside different electrolyser cells while varying several parameters like the distance of the electrode to the opposing non-conducting wall, current density on the electrodes or electrode height, many improvements can be made and much time is saved when designing new electrolysers for particular industrial purposes. To verify the obtained flow patterns, it is necessary to conduct experiments in addition to model-making. To achieve this quantification, three phenomena are considered. These are the formation of bubble vortices at the top and in the bulk (i.e. lower regions) in the channel, the depth of the bubble mist resulting from electrolysis and the bubble plume originating at the cathode when applying a certain current. Firstly, the formation of vortices is studied with the help of Particle Image Velocimetry (PIV) to investigate the actual occurrence of vortices while varying the (exposed) electrode height, current density and the distance between the cathode and the opposing non-conducting wall. Modern electrolysers gradually make more use of elastic elements being placed inside the channel to withstand mechanical stresses. The influence on the bubble flow of these elements is tested in different configurations as well. The depth of the bubble mist resulting from recirculation at the liquid-air interface is also examined while varying the same parameters. The analysis is performed by examining the light intensity of these clouds and comparing this to other configurations. Lastly, the different analysing methods are implemented on the bubble plume that originates at the cathode, while also visually depicting various exceptions like bubble burst or larger bubbles trajectories.

Transition to turbulence in electrolysers is dealt with in several earlier studies. In chapter 2, the field of

knowledge is categorized, and an overview of known experiments and outcomes is given. Furthermore, the aim and research questions of this research project are described in more detail in chapter 3. The methods, appliances and strategies used to obtain the results and comparisons to models are outlined in chapter 4. The results are given in chapter 5. These are elaborated upon in chapter 6 while discussing both the advantages and shortcomings of the chosen methods and strategies. This automatically leads to recommendations in order to improve further research.

2
Theory and Literature Review

The purpose of this theory and literature section is to gain more insight into relevant research fields that are related to the research aim discussed further in chapter 3. First of all, the concept of electrolysis is discussed together with basic concepts of fluid dynamics in section 2.1. Main concepts like flow regime types, bubbles and their influence on electrolysis are discussed in section 2.2. In section 2.3, a theoretical condition and practical experiences considering transition from laminar to turbulent flow are listed. Theory and earlier performed research about backflow and vortex formation is summarized in section 2.4. Then, earlier findings of a different reviewed result of turbulence, namely the formation of a wavy plume, are discussed in section 2.5.

2.1. Hydrogen from Electrolysis

Electrolysis is a technique which is used to induce a non-spontaneous chemical reaction with the use of an applied current. In general, the positive electrode (anode) attracts negatively charged ions or the negative electrode (cathode) receives positive ions. This ensures the availability for gaining electrons. To gain understanding of electrolysis, in this section, the basic concepts like the chemical reactions during alkaline water electrolysis, configuration and fluid flow dynamics are outlined.

2.1.1. Basic Concepts Alkaline Water Electrolysis

Water electrolysis splits water (H_2O) into hydrogen (H_2) and oxygen (O_2). An alkaline electrolyte like potassium hydroxide (KOH) or sodium hydroxide (NaOH) is added to the water in 20-40 wt.% (weight percentage) concentrations to ensure ionic activation at temperatures up to around 80 °C and a maximum pressure of 30 bar [5]. Figure 2.1 illustrates the conductivity values of aqueous solutions of KOH at various temperatures and weight percentages. The data clearly indicates that the utilization of KOH in the range of 20-40 wt.% is justified to increase conductivity, particularly at room temperature. Typically in industry, electrolysis processes are commonly carried out with a weight percentage of approximately 30% to ensure maximum efficiency.

At the cathode hydroxide ions are produced. These ions carry charges which are brought to the anode (typically across a membrane or diaphragm) and discharged there while producing oxygen [8]. In short, the following reactions contribute to this process. At the cathode [9]:

$$2H_2O + 2e^- \rightarrow H_2 + 2OH^- \tag{2.1}$$

and at the anode:

$$4OH^- \rightarrow O_2 + 2H_2O + 4e^- \tag{2.2}$$

Therefore the sum reaction:

$$2H_2O \rightarrow 2H_2 + O_2 \tag{2.3}$$

As one can see, four moles of hydroxide ions oxidize to oxygen and water, during which four mole electrons are released [10]. The standard potential of the cell E_0 can be found by using:

$$E_0 = -\frac{\Delta G_0}{zF} \tag{2.4}$$

Where the Gibbs free energy ΔG_0 value of 237.2 kJ/mol is used [11]. Here, $F = 96.487\ \mathrm{A \cdot s\ mol^{-1}}$ is the Faraday constant, z is the number of electrons involved in the reaction. For alkaline water electrolysis,

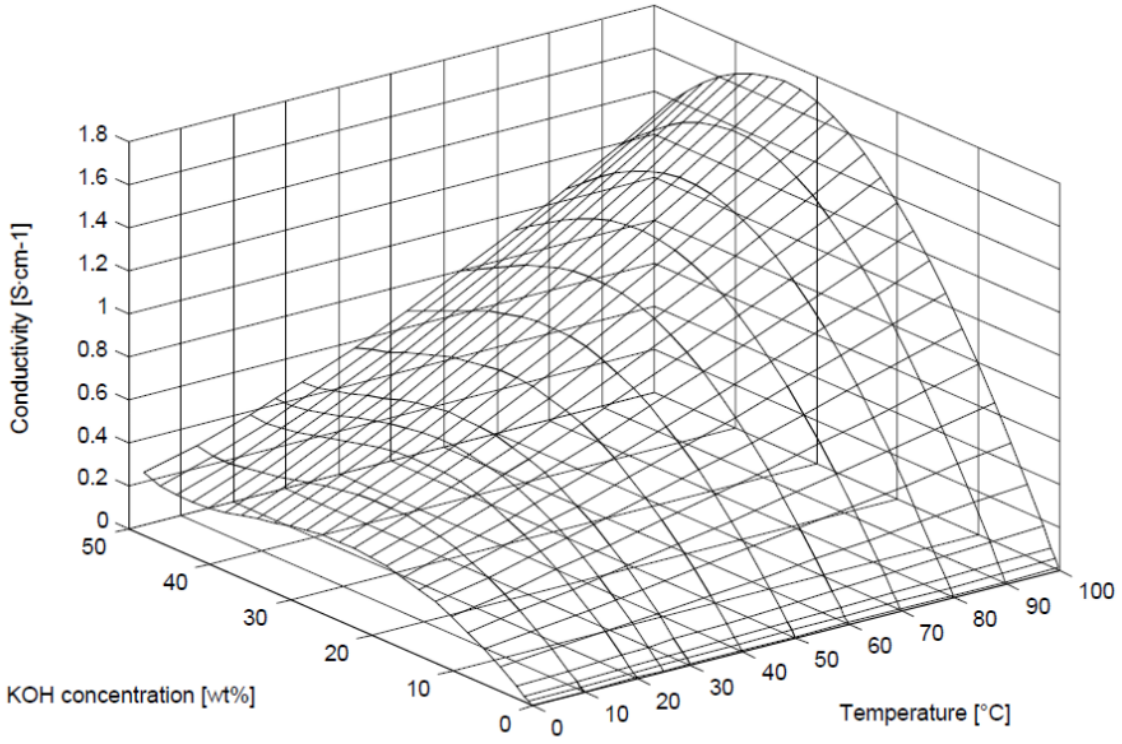

Figure 2.1: Conductivity of aqueous solutions of KOH for different temperatures and weight percentages (wt.%) KOH [6]. Data from [7].

the standard cell potential can be found by:

$$E_0 = -\frac{237.2 \cdot 10^3}{2 \cdot 96485}$$
$$E_0 = -1.228 \text{ V} \tag{2.5}$$

From this, as water electrolysis is a non-spontaneous reaction, one can see that at least 1.23 V is needed from an additional power source to perform water electrolysis.

Butler Volmer and Tafel Slope In practice, the applied potential needs to be larger than the standard cell potential E_0. The overpotential is the difference between the applied potential and the theoretical equilibrium potential of the reaction. The overpotential which needs to be applied is (among other factors) dependent on the electrolyte resistance. The obtained current when applying a certain overpotential is derived by the Butler Volmer equation, see eq. (2.6).

$$\frac{i}{i_0} = \exp\left(\frac{(1-\alpha)nF}{\mathcal{R}T}\eta\right) - \exp\left(\frac{\alpha nF}{\mathcal{R}T}\eta\right) \tag{2.6}$$

where i_0 is the exchange current density, $\mathcal{R}$ is the universal gas constant of $8.31446\,\text{J}\cdot\text{K}^{-1}\cdot\,\text{mol}^{-1}$, n the number of electrons involved in the reaction, α is the charge transfer coefficient and η is the overpotential at the electrode surface. In some instances, chemical reactions at an electrode-electrolyte interface involve intermediate steps, where one step is significantly slower than the others. This slower step is termed the rate-determining step (RDS). Often, when the RDS involves the transfer of a single electron, the Butler-Volmer equation is a suitable and accurate approximation. It is important to note that the RDS rarely, if ever, encompasses the simultaneous transfer of multiple electrons [12]. Therefore, here $n = 1$. The efficiency of the electrolysis process depends on the overpotential η. As can be seen in Figure 2.2, the potential that needs to be applied to deliver a certain current density in the system is highly dependent on these factors.

Notably, the Tafel slope is a measure of the electrochemical kinetics governing a chemical reaction. It represents the rate of the electrochemical reaction as a function of the overpotential. Mathematically,

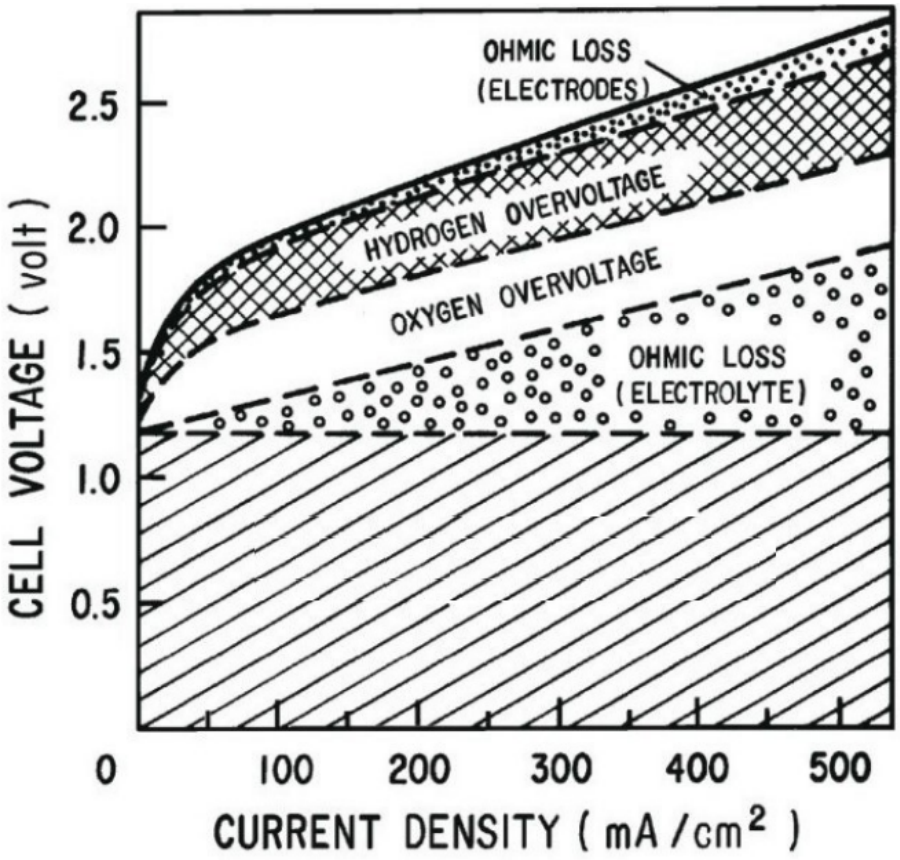

Figure 2.2: By systematically targeting individual contributions to cell voltage, a methodical approach is enabled for reducing the overall cell voltage. This technique enables a specific focus on each contribution, thereby facilitating the implementation of highly effective voltage reduction strategies. From [13].

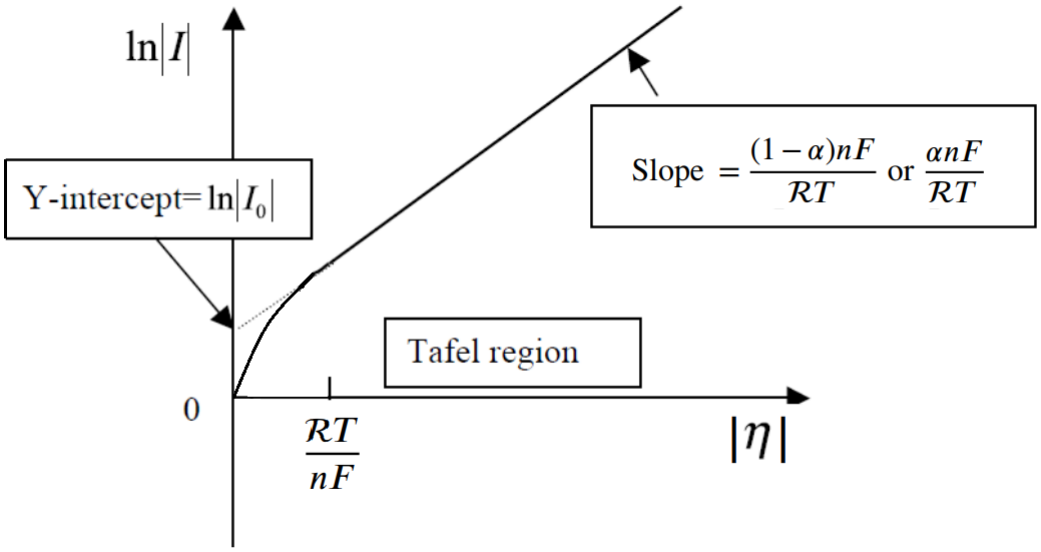

Figure 2.3: Electrochemical Tafel slope showing the relationship between overpotential and current density (logarithmic scale). Adapted from [14].

the Tafel slope is defined as the logarithm of the ratio of the current density to the absolute value of the overpotential. This slope, as depicted in Figure 2.3, is linked to the activation energy of the reaction, which is the energy required for the reaction to occur. It provides valuable insights into the mechanism and efficiency of the reaction.

Various factors, including the type of electrode, the concentration, and the temperature of the electrolyte, influence the Butler-Volmer equation, and consequently, the Tafel slope. A steep Tafel slope may indicate that the reaction is limited by the kinetics of the hydrogen or oxygen evolution reaction. On the other hand, a flat Tafel slope might suggest that the reaction is constrained by mass transport or the availability of reactants. In summary, understanding and analyzing the Tafel slope plays a crucial role in deciphering the electrochemical behaviour of a system and optimizing its performance. In case of this project, it is important that the electrodes have a homogeneously distributed voltage. When assuming a Tafel slope of 50 mV [15] we expect a linear relationship between the logarithm of the current and the overpotential with a slope of 50 mV for every tenfold change in current. Specifically, there should not be a significant difference in voltage distribution between the lowest and highest points of the electrode. The value for the contribution of the activation losses is found by using $e^{\frac{n\alpha F\eta}{RT}}$. Ideally, this is a value close to 1. For $\alpha = 0.5$, we find $e^{\frac{n\alpha F\eta}{RT}} \approx 1.45$, when applying an overpotential of 20 mV, which is well below 50 mV. As the activation losses only contribute partly to the total resistance losses, this loss (45%) can be considered an acceptable in-homogeneity. Achieving this uniform voltage distribution is dependent on several factors, including the size of the electrode, its ohmic resistance $R(\Omega)$, and its surface area. This means that a conducting Nickel bar can be attached to ensure homogeneous current distribution. However, it is important to consider that attaching a conducting Nickel bar may affect the flow dynamics of the electrolyte. When acknowledging the maximum voltage drop of 20 mV, the maximum applied current over an electrode pair is:

$$I_{\text{max}} = \frac{20\ \text{mV}}{R_{\text{electrode}}}, \tag{2.7}$$

where $R_{\text{electrode}}$ is the electrode resistance of that particular shape and material.

2.1.2. Cell configurations

In Figure 2.4 an overview of a traditional and a zero-gap AWE-setup is shown. The configuration consists of two electrodes (anode and cathode), an electrolyte, and a reactor-cell consisting of two chambers separated by a membrane or diaphragm. As stated, electrolytes like NaOH and KOH are used for ionic activation. These might cause some corrosion at the surface of the electrodes, and therefore neutralizing chemicals might be needed to avoid this. These electrodes are placed against a membrane (or diaphragm) and this creates two separate chambers. The membrane is designed to support the transport of created hydroxide (OH^-) ions from the cathode to the anode. The membrane preferably copes well with corrosion in alkaline media, has high conductivity and possesses high water permeation [8]. From Figure 2.4, one can see that the conventional AWE setup, which typically includes a gap between the membrane and electrodes, is commonly substituted with the zero-gap cell configuration. The primary motivations for this shift is that reducing the gap between electrodes significantly reduces the ohmic resistance losses normally caused by the electrolyte between the electrodes, when instead of an electrolyte-filled gap, only membrane separates the electrodes [16]. Because of this, zero-gap electrolysers need less energy to drive the chemical reaction. This can be seen as the ohmic losses and are significantly reduced when electrolyte resistance can be dismissed, see Figure 2.2. This way, the energy efficiency is improved and operating costs are lowered.

This makes zero-gap electrolysers an attractive option for industrial applications that require large-scale hydrogen production. This is the reason that for this experimental research, (near) zero-gap electrolysis is considered.

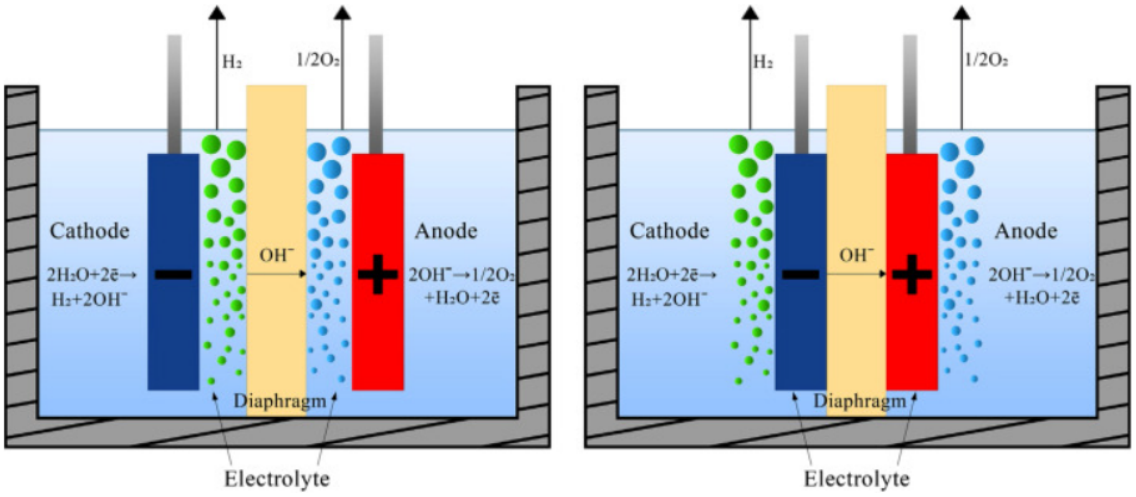

Figure 2.4: Schematic representation of alkaline water electrolyser with traditional non-zero gap (left) and the modernly used zero-gap (right) configuration. From [17].

Elastic Element

In AWE, the use of an elastic element is often used to control gaps between an electrode and a wall or bipolar plate. In Figure 2.5, an example of a configuration containing an elastic element is given. This is an element made of thin wires with high porosity and low solid fraction. With deteriorating electrodes or thermal expansion due to high temperatures during electrolysis, having an elastic element to compensate for these circumstances is convenient. Even pressure differences caused by big bubbles may affect electrode-wall distances as well. When there is no elastic element present, changes in these electrode-wall distances may lead to mechanical stress inside electrolysers operating with high pressures. In some cells with a planar configuration, short circuit might occur more easily without having an elastic element in place to control the electrode-wall distances. This is why it is interesting to see what the effect is of such elastic elements to the fluid flow.

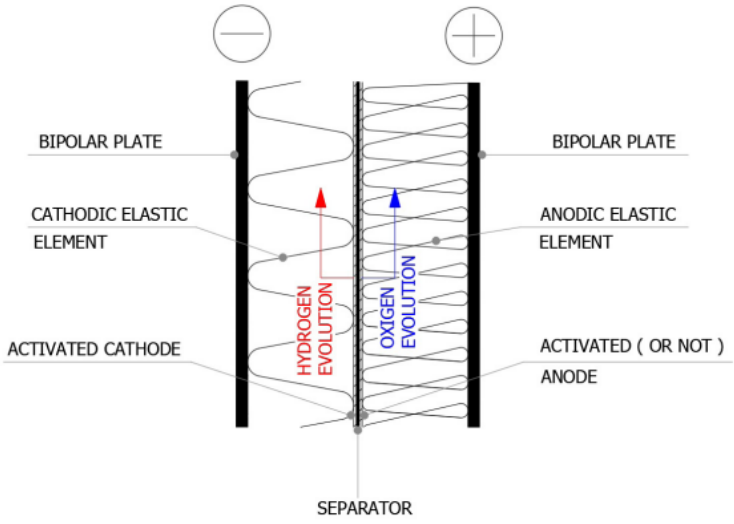

Figure 2.5: Schematic representation of alkaline water electrolyser with elastic element between wall/bipolar plate and electrodes. From [18].

2.2. Hydrogen production performance

In this section, the different types of flow regimes that could be encountered during this research and might be relevant for the modelling are listed. Secondly, the influence of bubbles on the flow inside the channel is examined. After this, the influence on the performance of alkaline water electrolysers of these

bubbles is discussed.

2.2.1. Bubbles in alkaline water electrolysers

A factor affecting the mass transfer (here the electrolyte replenishment against the electrode surface) and therefore the electrolysis's performance, is the formation of gas bubbles deposited on the surface of an electrode. The void fraction (referred to as gas fraction) ε denotes the fraction of the volume occupied by gas. This means:

$$\varepsilon = \frac{V_{\text{gas}}}{V_{\text{gas}} + V_{\text{liq}}} \tag{2.8}$$

Where V_{gas} and V_{liq} are the local volumes of the gas and liquid respectively in the cathodic channel. The result of applying current to an electrode pair is illustrated in Figure A.1 in the appendices. Clearly, the void fraction rises with the current density and we see that the total volume rises within the channel. For this range of current densities (0 - 6000 A/m^2), the gas fraction in the cathodic side of the channel rises to 0.23 as can be seen in Figure A.2. The superficial flow velocity U_{gas} can be regarded as the velocity of the gas flow if the flow of the bubbles is the only moving phase in the medium. This can be found by multiplying the interstitial gas velocity u_{gas} with the gas fraction ε. The volume flow rate of the gas Q_{gas} is needed to determine U_{gas}:

$$U_{\text{gas}} = \frac{Q_{\text{gas}}}{A} \tag{2.9}$$

It is found that gas liquid flow is generally divided into five types of flow regimes, namely bubbly, slug, churn-turbulent, annular drop and falling film flow [19, 20], see Figure 2.6. A flow regime is generally determined by the velocity and the quantities of the liquid and gas in multiphase flow. For this research, the most relevant regimes are the bubbly flow and the slug flow. Bubbly flow, regime (1) in the figure, is characterized by the cell that contains mostly liquid with small bubbles of free gas rising within it. The liquid comes in contact with the wall surface while the bubbles simply serve to decrease the density and increase viscosity. When the flow rate of the liquid is increased, the bubbles become more uniformly dispersed throughout the pipe's cross-sectional area. As gas bubbles rise, they might expand and merge (coalesce) into larger bubbles called slugs, see regime (2) in the figure. This happens while the liquid remains in continuous phase. The liquid film surrounding the slugs may descend downwards. Both the gas and liquid phases have a significant impact on the pressure gradient.

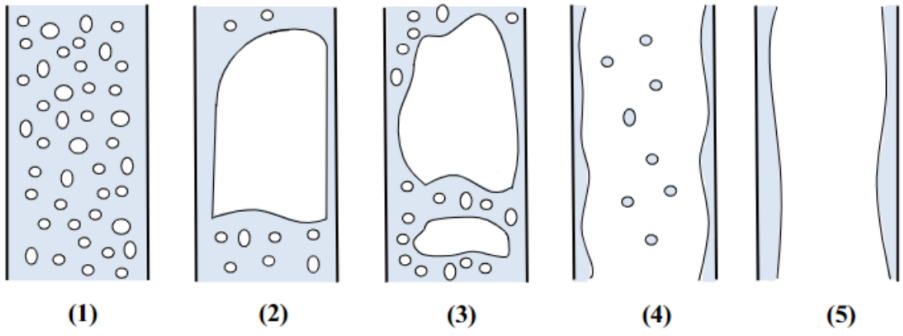

Figure 2.6: (1) Bubbly, (2) slug, (3) churn-turbulent, (4) annular drop and (5) falling film flow regimes for two-phase flows. From [21].

2.2.2. Bubbles in electrolysers

The presence of gas bubbles, acting as the dispersed phase, introduces changes to both the electrical and thermal characteristics of the electrolyte, as well as altering the diffusion of electro-active substances and the distribution of current density. These factors subsequently have implications for the overall performance of the cell at a macroscopic level. The influence of bubbles on the fluid dynamics is studied by Luo

et al. [22]. They found that the presence of bubbles induced strong convection of electrolyte within the cell gap. The primary reason for this increased velocity is the drag force exerted by the bubbly flow. They compared the velocity of the fluid while having no working electrode pairs (only pumped induced flow) and a 440 A/m^2 current density over the electrodes and found a nine times higher velocity in the latter case. Here, the bubble flow was deemed as the main reason for recirculation of the electrolyte. Even at lower Reynolds numbers, oscillatory motions of the bubbles adjacent to the electrodes, induced local turbulence, expressed in velocity fluctuations, also found by Shah and Jorne [23]. It must be stated that near the anode, much more turbulent behaviour was found than at the cathode. The average size of hydrogen bubbles formed at the cathode is several tens of microns [24]. In a research by Baczyzmalski [25], it was found that larger bubbles ($d_b > 1.5$ mm) often propagate in an oscillatory trajectory. In particular, the presence of impurities or salts might cause these paths. They analysed the speed and trajectory (including wavelength) of multiple large bubbles. These can be found in Figure 2.7. In this figure, we can see that a linear relation exists between the bubble size and wavelength, where $\lambda \approx 10 \cdot d_b$. A significant influence of the current density is not visible. Logically, the bubble rise velocity grows with bubble size. This is elaborated on in subsection 2.3.2.

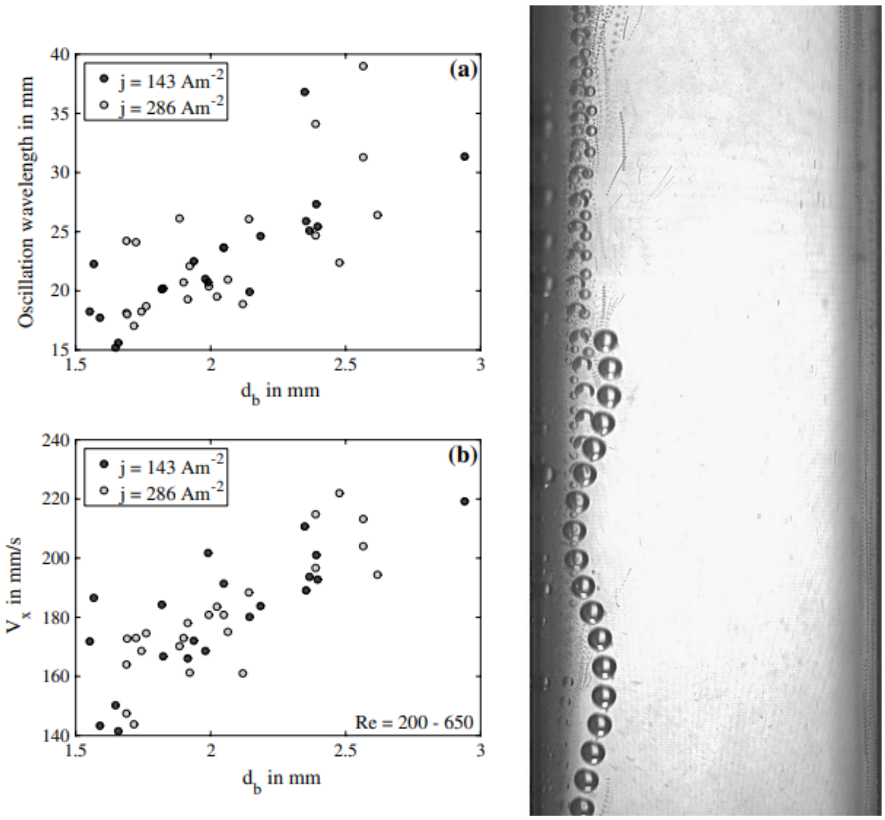

Figure 2.7: Left: Bubble trajectory wavelength (a) and mean vertical rise velocity (b) of larger ($d_b > 1.5$ mm) bubbles. Right: Trajectory multiple large bubbles. From [25].

2.2.3. Mass transfer and bubble influence

The rate of mass transfer from the bulk to electrode surface is influenced by various factors such as the concentration of the ions in the solution, the viscosity of the solution and the surface area of the electrodes. If the mass transfer rate is slow, it can lead to reduced efficiency of the electrolysis process, and in some cases, can even lead to reduced selectivity of the desired product. In many industrial applications, the optimization of mass transfer is crucial to achieve high yields of the desired product and to minimize the production of undesired by-products.

Bubble formation can reduce the hydrogen production as a blockage forms of the electrocatalyst surface. It has been reported that removal of bubbles can result in a potential decrease of 10%-25% [26, 27]. It

is believed however that mass transfer rates might increase due to bubble formation, especially micro-mixing caused by the bubble induced fluctuations in the flow field. It is believed that especially diffusion transition contributes to ion transfer mechanisms. From a high to a low concentration region hydrogen molecules are diffused as heat diffuses from high to low temperatures. One can assume that the emitted particles in these diffusion processes are described by random and frequent collisions [28, 29]. By comprehending this concept, it becomes possible to devise approaches that reduce the negative impact of bubbles on energy conversion efficiency and stability, while also harnessing the advantages offered by bubble-related phenomena.
The effect of gas along electrodes is also examined by Fouad and Sedahmed in 1972 [30]. They varied the rate of gas evolution, the electrode height and the electrode-diaphragm separation in a traditional non-zero gap configuration, see Figure 2.8. They depicted two streams of gas, namely the flow of bubbles near

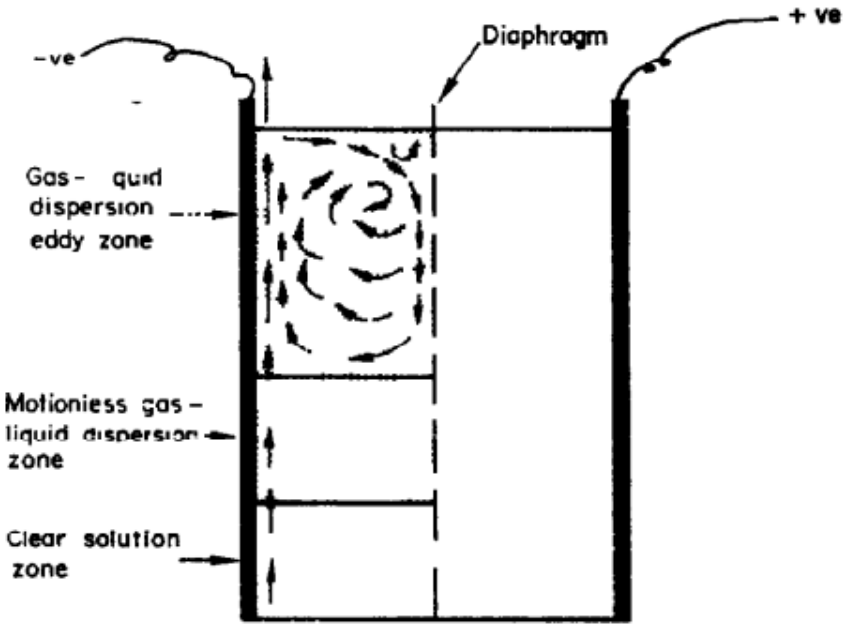

Figure 2.8: Electrodes in traditional configuration, where the diaphragm splits two channels. From [30].

the electrode, and one flow near the diaphragm. These bubbles arrive there as a result getting dragged by the displaced solution. This results in the formation of the "eddy-zone", which is similar to a vortex visible in this report. These eddies are believed to complement the mass transfer from the bulk to the surface of the electrode. They found that the formed vortices become larger in height as the current density was increased. When decreasing the electrode-diaphragm spacing, the eddy motion is intensified. The zone where eddy motions took place extended in the direction of the electrode. This led to an increase of mass transfer, as the vortex reached deeper levels as well. When the spacing became very small, the upward stream at the electrode collided with the vigorously downward-moving eddy current. This decreased the so-called convection effect and the rate of mass transfer. The effect of decreasing the electrode height (from 50 to 2.5 cm) led to a full vortex over the whole channel height instead of only the upper part being circulating. Obviously, the results of these experiments are determined using a non-zero gap and electrode-diaphragm distance is varied instead of electrode-wall distance. This causes a possible difference in bubble distribution compared to this project's case. Also the surface of the opposing wall is smoother when the opposing wall is not a porous diaphragm. However, both experiments relate to a electrode towards a non-reacting wall, and so are relevant to compare.

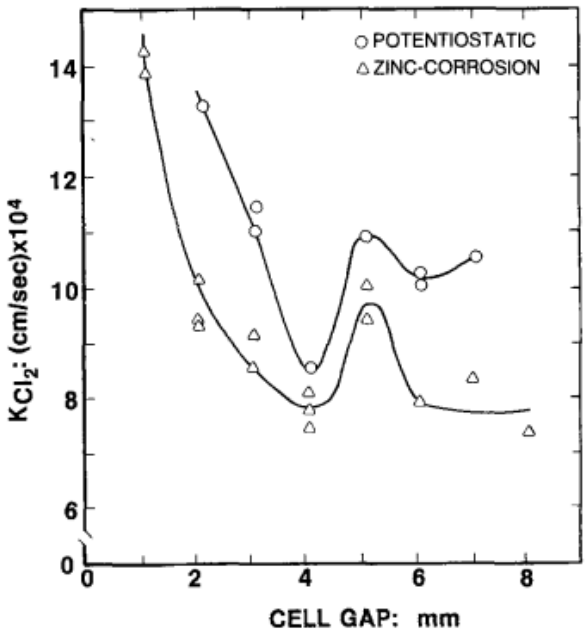

Figure 2.9: Mass transfer coefficient versus cell gap. Different effects of convection induced by bubbles while varying gap are visible. From [23].

Shah and Jorne in 1989 [23] also examined the influence of electrode geometry on the mass transfer of the electrolysis process and especially the convection that arose by the bubbles. They found that, when increasing the cell gap in a small range (up to 10 mm), a local maximum in mass-transfer occurred, see Figure 2.9. Namely, when adjusting the cell gap from 0 to 4 mm, the mass transfer decreases with gap. They stated this is caused by the fluid motion that becomes less intense with increasing the gap. A well-defined return flow occurs when the gap is between 4 and 5 mm. This does not interfere with the upstream of the (in this case chlorine) bubbles. Although the experiments of Fouad [30] and Shah [23] describe significantly different measurement circumstances, the effect of changing parameters on the mass transfer is relevant to this research project.

2.3. From laminar to turbulent flow

The Reynolds number quantifies the balance between the forces related to a fluid's inertia and its viscosity when it undergoes internal motion due to varying fluid velocities. The transition point from laminar flow to turbulence can be categorized in two ways. Namely, the theoretical transition value depending on the Grashof number $\mathrm{Gr_L}$ between two plates for example and practical transition point in electrolysis from earlier research.

2.3.1. Theoretical transition laminar-turbulent flow

Visco-elastic effects lower values of critical Reynolds numbers of parallel shear flows. The empirical critical Reynolds number of planar Poiseuille flow, which is flow between two parallel plates, is around 1700 [31]. The Reynolds number is given by:

$$\mathrm{Re} = \frac{\rho \upsilon L}{\mu} \tag{2.10}$$

This makes use velocity of the fluid flow υ, fluid density ρ, dynamic viscosity μ and the characteristic length L. That means that, for verifying the transitional Reynolds number, forced convection and a set fluid flow velocity is needed. For natural convection, the Grashof number between vertical plates $\mathrm{Gr_L}$ gives the transition point between laminar and turbulent flows:

$$\mathrm{Gr_L} = \frac{g\beta\,(T_\mathrm{s} - T_\infty)\,L^3}{\nu^2} \tag{2.11}$$

where g is the acceleration of 9.81 m/s^2, β is the coefficient for thermal expansion, T_s and T_∞ are the surface and bulk temperatures respectively, L is the vertical height along the plates and finally, ν is the kinematic viscosity of the electrolyte. The theoretical value of the Grashof number for the threshold between laminar and turbulent flow lies in the range of $4 \cdot 10^8$ [32]. In case of electrolysis the influence of the bubbles on the surface of the electrodes can be approximated. The rise in temperature causes a certain difference in electrolyte density due to the formation of gas bubbles. When working with high current densities, this relation can be approximated by

$$\frac{\Delta\rho}{\rho} = \beta\Delta T \qquad \text{with} \qquad \frac{\Delta\rho}{\rho} \sim 0.5$$

the simplified Grashof number becomes

$$\mathrm{Gr_L} \approx \frac{gL^3}{2\nu^2}$$

with

$$\nu = \frac{\mu}{\rho}$$

During this research, typically a KOH concentration of 1M (~5 wt.%) is used. This is relatively a low concentration, but for the purposes of this project -which is flow quantification- larger weight percentages are not needed. With a temperature of roughly 25 °C, the value for dynamic viscosity μ is $1.5713 \cdot 10^{-3}$ Pa·s and a density of 1307.2 kgm^{-3} [33]. Note that these values are found for a molarity of 1.0121 mol $\cdot L^{-1}$. From there, one can find the theoretical value for the height along the electrode where turbulence should occur.

$$L = \sqrt[3]{\frac{8 \cdot 10^8}{g}} \cdot \left(\frac{\mu}{\rho}\right)^{\frac{2}{3}} \tag{2.12}$$

For these values the transition height to turbulence along vertical parallel plates $L = 4.90$ cm. This equation shows that only the dynamic viscosity μ and density ρ have an influence on the transition height towards turbulent flow. These values are influenced by the temperature. The values of the theoretical transition height to turbulence versus the temperature between 15 and 60 °C is shown in Figure 2.10. Several data points from Guo et al. [33] are taken for the dynamic viscosity μ and density ρ leading to various values for L for different temperatures. One can see that as temperature rises, the transition height to turbulence becomes lower.

2.3.2. Experimental results turbulent flow

In the year 2000, Boissonneau and Byrne did research towards velocity profiles versus current density applied at different heights between the electrodes when pumped from the bottom [34]. The used techniques in this paper are Microscope Enhanced Visualisation (MEH), Laser Doppler Velocimetry (LDV) and Particle Image Velocimetry (PIV). They found that transition between laminar and turbulent flows occurs at different locations along the cathode lengths, depending on the respective current densities, see Figure 2.11. Note that this figure does not denote the zero-gap configuration, as well as a KOH solution, but a Na_2SO_4 (50 g $\cdot l^{-1}$) solution.

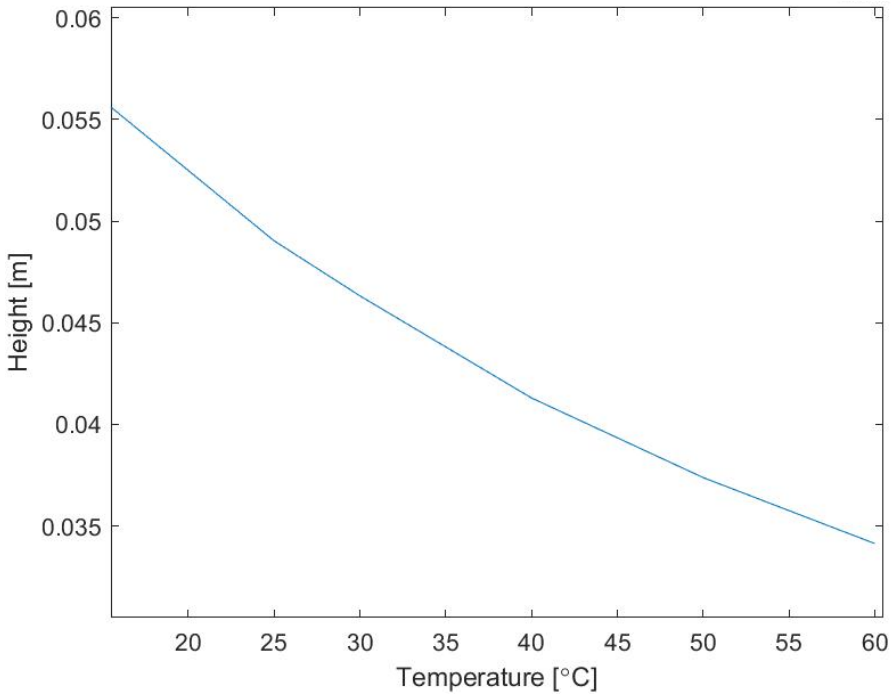

Figure 2.10: Theoretical transition height from laminar to turbulent flow along two parallel vertical plates for different temperatures of 1M KOH electrolyte and bubbles with 50 micron diameter. See eq. (2.12). The value for dynamic viscosity μ is 1.5713 $\cdot 10^{-3}$ Pa·s and a density of 1307.2 kgm^{-3}. Data from [33].

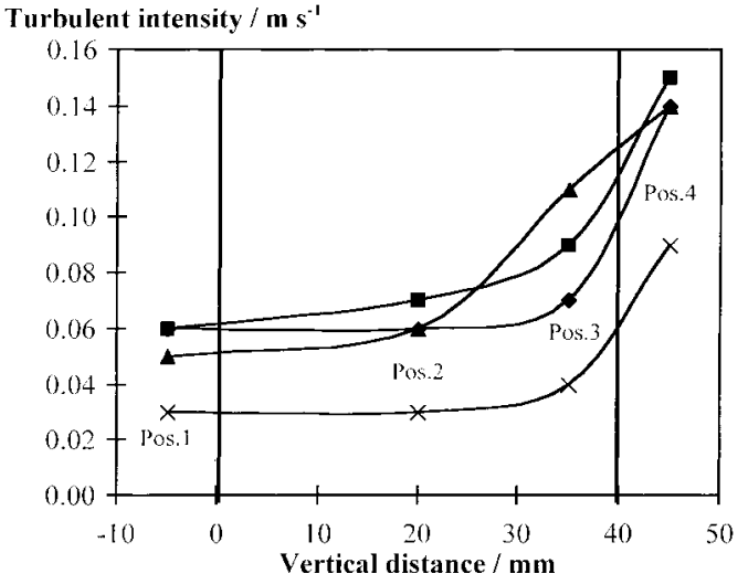

Figure 2.11: Evolution of turbulent intensity within the bubble layer along the cathode length for three distinct current densities: $j = 500$ (◆), 1000 (■), and 2000 (▲) A/m^2, within a Na_2SO_4 solution (50 g/l). The turbulent intensity at the channel center is provided for the current density $j = 1000$ A/m^2 (╳), while vertical solid lines demarcate the positions of the channel's inlet and outlet. From [34].

They also depicted that both turbulence and laminar behaviour can exist across the cell channel at the same horizontal plane. This is possible as in the middle of the channel, there are less bubbles and therefore less turbulence. This is an example of the bubble induced turbulence discussed in subsection 2.2.2. Pang et al. (2020) researched the influence of the Reynolds number on the turbulence and plume widths [35]. They found with the help of *in situ* High Speed Videography (HSV) a crossover to turbulence occurs when the Reynolds number exceeds 1200. This is in contrast to empirical higher values of 1700 described earlier. It is believed that internal force promoting bubble detachments causes this difference. When

Re exceeds 1000, the plume width expands and the bubble void fraction decreases because of decreased residence time of bubbles due to higher fluid velocity. The bubble sizes decreased monotonically with increasing Re. In 1975, Vliet and Ross [36] estimated the effect of inclining angles on transition height

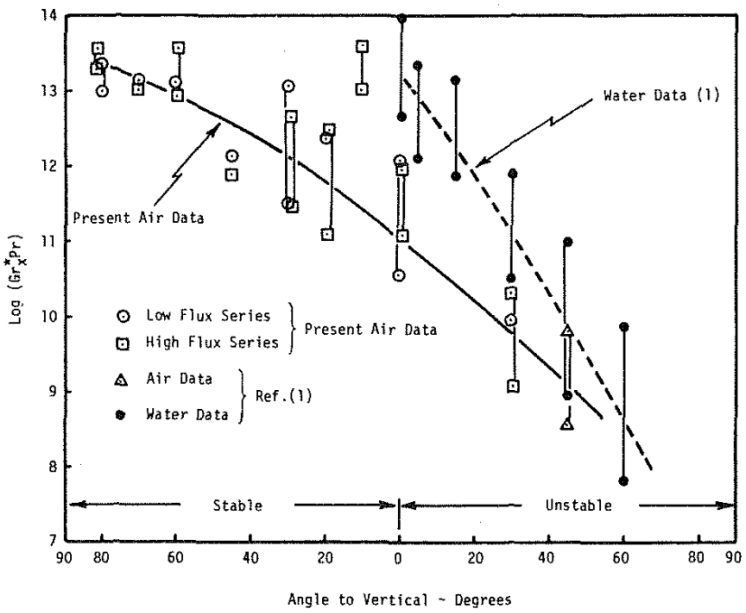

Figure 2.12: Transitional range $\mathrm{Gr_x} \cdot \mathrm{Pr}$ versus angle. From [36].

to turbulence. For a 90 degree hot plate in water they estimated the transition range in terms of Grashof number. Figure 2.12 shows shows these approximate transition regions in terms of $\mathrm{Gr_x} \cdot \mathrm{Pr}$ as a function of angle. This transition of 10^{13} for $\mathrm{Gr_x} \cdot \mathrm{Pr}$ is denoted by the Archimedes number Ar. Ar is given by [37]:

$$\mathrm{Ar} = g \frac{L^3}{\nu^2} \frac{(\rho - \rho_0)}{\rho_0} \tag{2.13}$$

If the variation of density is primarily due to a change in temperature (ΔT), then for small temperature differences $(\rho - \rho_0)/\rho_0 \approx \beta \Delta T$ (where β is the volumetric expansion coefficient), the Archimedes number can be related to the Grashof number (Gr).

The critical Archimedes number can be described as:

$$\mathrm{Ar}^* = \frac{g U_{\mathrm{gas}} z^4}{D_\mathrm{b} \nu^2} \tag{2.14}$$

with U_{gas}, the superficial flow velocity:

$$U_{\mathrm{gas}} = \frac{j \mathcal{R} T}{p n F} \tag{2.15}$$

This suggests that turbulence scales with height like $z \propto j^{-1/4}$. Here p denotes the atmospheric pressure in Pa. The hydrodynamic dispersion coefficient, D_b, can be estimated by multiplying the Stokes velocity v_{Stokes} and characteristic length r, which is the bubble radius. The Stokes velocity is given by (2.16). With, assuming a bubble size of 50 microns [24], equals 1.1 mm per second.

$$v_{\mathrm{Stokes}} = \frac{\rho_\mathrm{l} g d^2}{18 \mu} \tag{2.16}$$

In this case, D_b equals $2.833 \cdot 10^{-8}$ m^2/s. The critical Archimedes number was found to be $\mathrm{Ar}^* = 10^{12}$. For different values of the current density this leads to theoretical values for transitional height. In Figure 2.13, the values for the transitional height are outlined versus current density. These are thus found by:

$$z = \left(\frac{\mathrm{Ar}^* D_\mathrm{b} \nu^2}{g U_{\mathrm{gas}}} \right)^{\frac{1}{4}} \tag{2.17}$$

It is clear that the height values for transition to turbulence are different than the heights found by Boissonneau and Byrne (Figure 2.11). The differences in height can be linked to the fact that Boisseneau and Byrne used a downcomer where flow recirculated towards the bottom of the channel, creating a mix of natural and forced convection.

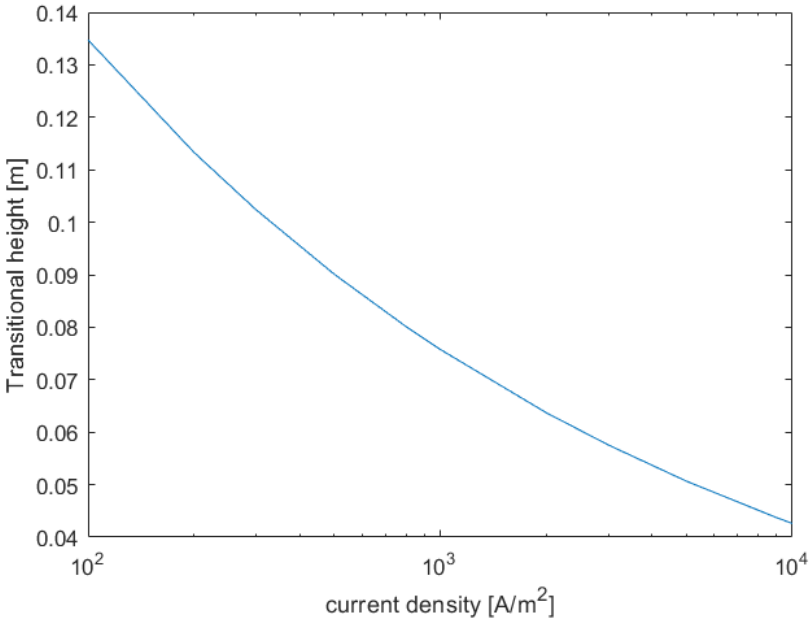

Figure 2.13: Transitional height versus height based on critical Archimedes number for bubbles with 50 microns diameter. Based on [36].

2.4. Backflow and Vortex Formation

A widely occurring phenomenon is the backflow in electrolysers. The liquid and bubbles have a positive (upwards) velocity along the electrodes and when this arrives the liquid-air interface, the gas escapes the surface but the liquid is held by the gravitational forces so a vortex originates.

Weier and Landgraf examined two-phase flow at gas-evolving electrodes and especially convection driven by Lorentz forces and found that Lorentz forces are a flexible tool to shape flow fields in the electrode gap [38]. They mainly varied the parameters current density and gap width and found that a recirculation region is observed. Equation (2.3) states twice as much hydrogen is produced compared to oxygen in terms of volume. This means the liquid momentum on the cathodic side is larger than on the anodic side. The liquid motion is deflected and Weier and Landgraf found that the larger hydrogen bubbles were able to penetrate trough the liquid-gas interface, while the smaller bubbles were entrained in the fluid flow. Recirculation was also depicted by Shah and Jorne [23]. They found recirculation near the top of the electrode with a cell gap of 5 mm using $ZnCl_2$ to extract chlorine gas. While these findings were generated using a traditional, non-zero gap configuration, it is essential to consider the behaviour of bubbles with various sizes to gain a comprehensive understanding of the flow characteristics. Riegel et al. [39] in 1998, examined the influence of varying the cathode height (from 40-400 mm), the current density up to 6250 [A/m^2] and mean electrolyte velocity on flow regimes. Backflow, which (according to them) limits the efficiency of a electrolytic process as the void fraction and electrical resistance increase considerably, is found at currents higher than:

$$I = -3.79 + 128v \tag{2.18}$$

Where I[A] denotes the current and v the mean velocity of the electrolyte in m/s.
Backflow occurrence is thoroughly investigated by Vogt [40, 41] towards an explanation and the conditions for the abrupt change from a bubble dispersed layer and layer free of bubbles towards a cross-sectional layer of bubbles in case of a gas-evolving electrode and an inter-electrode gap towards either a membrane or wall. He states that as the thickness of the bubbly plume δ increases, the velocity v_0 at the

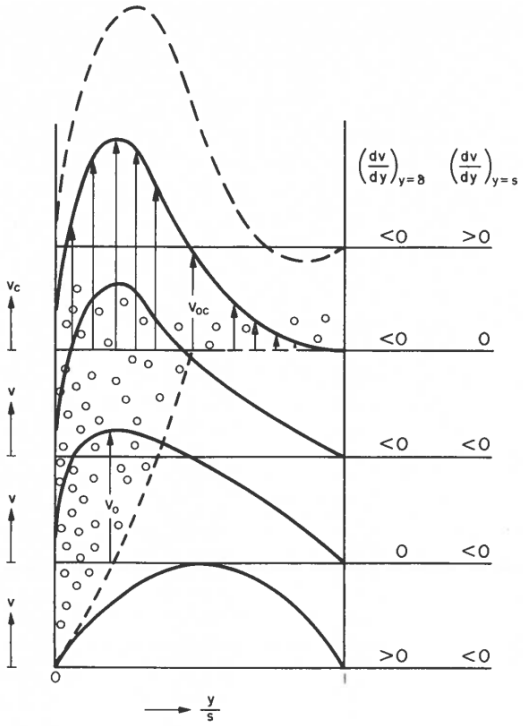

Figure 2.14: Schematically, the change of velocity gradients at the boundary layer between bubble plume and liquid ($y = \delta$) and at the wall opposite to the gas-evolving electrode ($y = s$). From [42].

boundary of both layers increases as well. The liquid flow rate in the bubble layer increases as much as the liquid flow rate in the liquid layer decreases and, because of this, the velocity gradient $\mathrm{d}v/\mathrm{d}y$ decreases at the boundary (at $y = \delta$).

At the opposing wall, this causes the velocity gradient to increase, see Figure 2.14. Here, $\mathrm{d}v/\mathrm{d}y = 0$ denotes the critical condition of disappearance of the bubble street combined with a sudden change in flow pattern.

In 2012, Alexiadis et al. derived that, while having laminar flow, vortices arose and linked this to pseudo-turbulence [43, 44]. They researched the occurrence of those vortices as a function of current density, bubble diameter and channel thickness. They found a quasi-steady regime when applying a low current density and saw large bubbles. In the bulk, the void fraction was low, as only recirculating bubbles were present, and the velocity predominantly in the negative y-direction (downwards). This is depicted in Figure 2.15 (a). We see that, as Vogt described as well, a counteracting flow exists in the bulk as well to compensate for the upward flow at the electrode. This is denoted by "bulk downstream" in the figure. When increasing the current density or decreasing the bubble diameter considerably, bursts from the gas blanket occur towards the bulk. The frequency of these bursts is directly related to the severity of these increases. At a certain level of current density or bubble diameter, the velocity profile in the channel changes completely. The vortices increase the mixing in the channel and the void fraction. The bubbles are dragged into the vortices instead of released at the top. This way, the efficiency of the whole cell might be affected in a positive way due to the mixing. This reduces the concentration gradients at the cathode. However, the electrical resistance might be increased. In equation (2.19) the relation is given for the theoretical transition point between the quasi-steady regime and the pseudo-turbulent regime. This relation is denoted as:

$$\frac{U_{\mathrm{gas}}\,(\mu_1/\rho_1)^{11/3}}{d^4 l^2 g^{7/3}} = K \tag{2.19}$$

with

$$U_{\mathrm{gas}} = \frac{jM}{zF\rho_{\mathrm{g}}} \tag{2.20}$$

Where d is the bubble diameter, l the channel thickness, M is the molecular mass of the gas ($2 \cdot 1.00784$ g/mol), j is the current density, F is Faraday's constant, and z is the number of electrons involved in the chemical reaction, which for this type of electrolysis equals 2. This means superficial velocity U_{gas} directly linked to current density j. A quasi-steady flow occurs for K-values of less than 1.07 x 10^{-4} and a pseudo-turbulent regime occurs for K is higher than 2.34 x 10^{-4}. During the modelling, the bubble diameter has a maximum size for the occurrence of pseudo-turbulence. When having a small diameter, there are more bubbles and the density in the bulk is decreased. This creates a higher density ratio between the blanket and the bulk, which creates more unstable flow. If U_{gas} is increased, a larger number of bubbles is recirculated. The bulk density is decreased, and so a larger instability region exists. A lower channel depth leads to a higher impact of recirculating bubbles due to the lower amount of liquid in between the electrode and the wall. The density ratio is increased as well by this and this means a smaller electrode-wall distance leads to a destabilized flow.

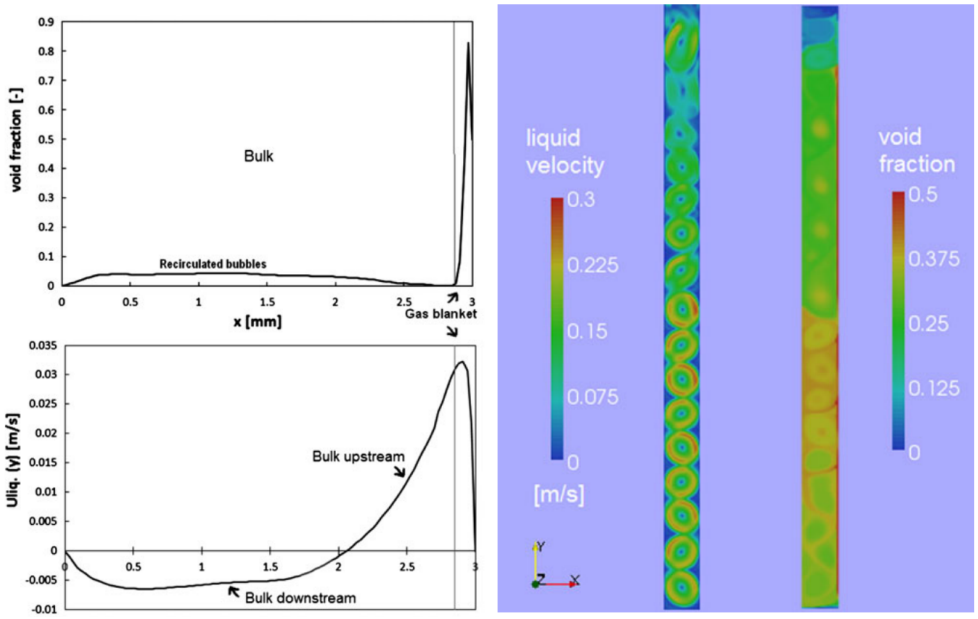

(a) (b)

Figure 2.15: (a): The velocity and void fraction profiles for the quasi-steady regime. (b): Liquid velocity and void fraction in the quasi-turbulent regime [43]. Both single channel.

As stated the found that the transition between the quasi-steady regime and pseudo-turbulent regime is affected by the gas flux at the wall U_{gas} and the bubble diameter d [44]. A relation can be given for the theoretical transition current density j_{trans} to pseudo-turbulence:

$$j_{\text{trans}} = \frac{U_{\text{trans}} \cdot z \cdot F \cdot \rho_{\text{g}}}{M} \tag{2.21}$$

Here, a value of $0.0813 \cdot 10^{-3}$ [kg/L] is taken for the density of the hydrogen gas ρ_g [45]. For a 1M KOH solution, when using theoretical values for the dynamic viscosity and the density of the KOH-solution derived in [33], the theoretical transition point towards pseudo-turbulence is given in Figure 2.16. This is interesting to examine experimentally, see chapter 4. The assumed value for the dynamic viscosity μ equals $1.5713 \cdot 10^{-3}$ [mPa·s] and the density of the electrolyte equals 1307.2 [kg·m^{-3}][33].

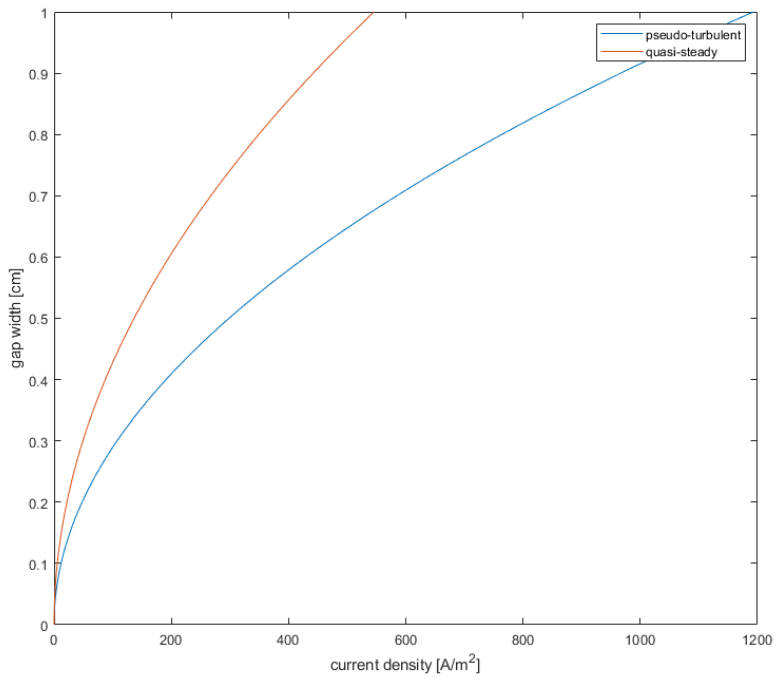

Figure 2.16: Theoretical transition point according to Alexiadis [43] to pseudo-turbulence and quasi-steady regime for current density versus electrode-wall distance for 1M KOH solution. For a temperature of roughly 25 °C, the value for dynamic viscosity μ is 1.5713 $\cdot 10^{-3}$ mPa·s and a density of 1307.2 kgm^{-3} [33] is used. It should be noted that a hydrogen bubble diameter of 50 microns is assumed.

2.5. Wavy Bubble Plume

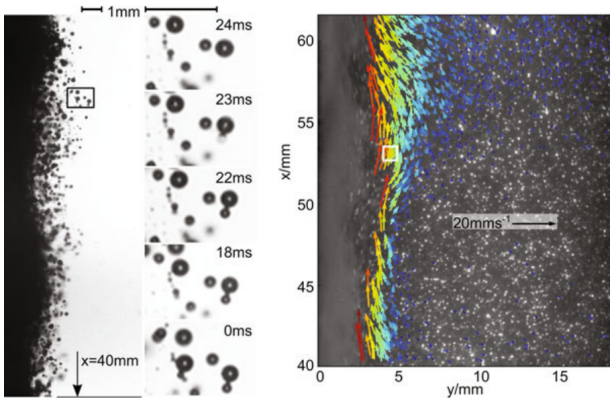

Figure 2.17: A hydrogen bubble curtain near the electrode. A zoomed sequence shows the coalescence occurring between 22 ms and 23 ms. At the right, the velocity profile mirrors the wavy profile of the curtain. From [38].

One phenomenon occurring in alkaline water electrolysis, is the wavy bubble plume. A wavy bubble plume refers to the formation of a pattern of oscillating gas bubbles on the electrode surface when performing electrolysis. Weier and Landgraf clearly found a wavy bubble curtain layer near the cathode of H_2 bubbles [38], see Figure 2.17. However, they reported that they were not able to determine liquid phase velocities close to the electrode, since the light emitted by the tracer particles was blocked due to the high void fraction in the region. The reported bubble sizes were ranging up to 400 μm, with outlier bubbles up to 3 mm. This is also observed in visualizations of Boissonneau and Byrne [34] and Aldas [46]. Earlier in 1989, Shah and Jorne [23] examined the bubble envelope shape when altering the gap width. These differences can be seen in Figure 2.18. They stated that the velocity of the electrolyte does not significantly affect the shape of the envelope for small cell gaps. When the distance between the electrodes is increased, the bubble layer near the bottom of the cell expands vertically in a linear fashion. The

circulating motion within the cell becomes more pronounced and elevated compared to situations with smaller electrode gaps. In contrast to small electrode-wall distances, the configuration of the bubble layer is influenced by the speed of the liquid flow.

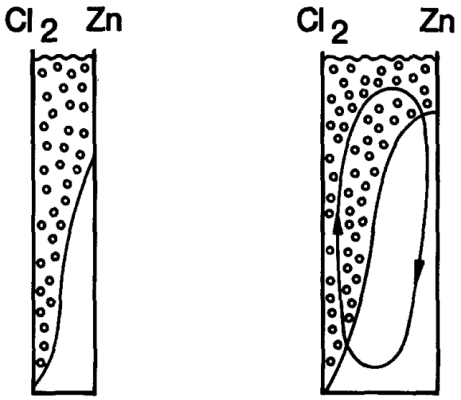

Figure 2.18: Schematic overview of observed bubble envelope shapes for small cell gap of < 4 mm (left) and bigger cell gaps of 8 mm (right). From [23].

3
Research Project

This chapter elaborates on the research project in terms of the objectives and overall approach. The main research objective of this thesis is to enhance our understanding of multiphase flow patterns in electrolysis. This is done by creating overviews of vortex formation, mist heights and bubble plumes at cathodes while altering several parameters like the current density j, electrode-wall distance w and electrode height h. The whole research project can be divided into three different sub-projects as listed below.

Vortex formation The main idea of this research project is to create a way to distinguish flow patterns during water electrolysis. Varying the current density, height of the electrolyte and electrode-wall distance, the aim was to create a comprehensive overview of the types of vortices occurring inside the electrolyte, especially the quantity, size and shape of the vortices varying different parameters. An example of such vortex formation is shown in Figure 3.1a as circular bubble motion is visible. To address this, extensive research is being conducted to explore different methodologies, such as ultrasound detection and particle imaging. Additionally, various factors, including lighting conditions and sample timing, are being tested to identify the optimal measurement techniques. More on these different strategies can be found in chapter 4. Finding optimal measurement configurations should help research initiatives in the future to gain insights concerning fluid dynamics more easily. In addition to developing an analysis strategy, the research project explores various configurations to examine the effects of altering the mentioned parameters. This leads to the research question:

- How does manipulation of current density, electrolyte height and electrode-wall distance influence the quantity, size, and shape of vortices within the electrolyte during zero-gap water electrolysis?

Mist height In parallel with the vortex formation study, a series of experiments is conducted to complement existing simulations and gain insights into bubble cloud (mist) height variations in zero-gap electrolysers under different conditions. Key parameters, such as electrode-wall distance, current density and electrode height exposed to the KOH solution are varied to identify the potential correlations with the size of the recirculating bubbles. An interesting observation is the variation in intensity of the bubble mist, where differences in brightness may be attributed to variations in gas fraction, see Figure 3.1b for an example of a mist cloud reaching a certain depth. This investigation aims to uncover fundamental relationships between the mentioned parameters and bubble behaviour, providing valuable qualitative data that complements (or contradicts) simulation work.

- How do variations in electrode-wall distance, current density, and electrode height influence mist height in zero-gap electrolysers?

Bubble plume analysis Another significant aspect of the research project involves analyzing bubble plumes formed at the cathode during water electrolysis, see Figure 3.1c for a plume originating at the cathode. Detailed mapping of the plume thickness along the electrode at various heights allows for an observation of potential turbulence transitions. Varying the current density facilitates verification of existing empirical values for turbulence along vertical plates, providing valuable insights into the behaviour of multiphase flow compared to forced convection for example. This is examined by using both computational analysis methods and visual analysis. Especially big bubble trajectories are investigated individually. Understanding the dynamics of bubble plumes is crucial, as they significantly influence mass transfer rates, species distribution, and overall process performance. Combining experimental techniques and computational simulations, it is interesting to see how this matches in practice.

- How does varying parameters like current density and height along the cathode influence the thickness and turbulent behaviour of the bubble plume originating?

In conclusion, this research project seeks to advance our comprehension of flow patterns and bubble dynamics during water electrolysis. By exploring fundamental phenomena and providing validation data to complement model-making, the study contributes to the development of enhanced and efficient electrolysis processes, furthering the progress of clean and sustainable energy technologies.

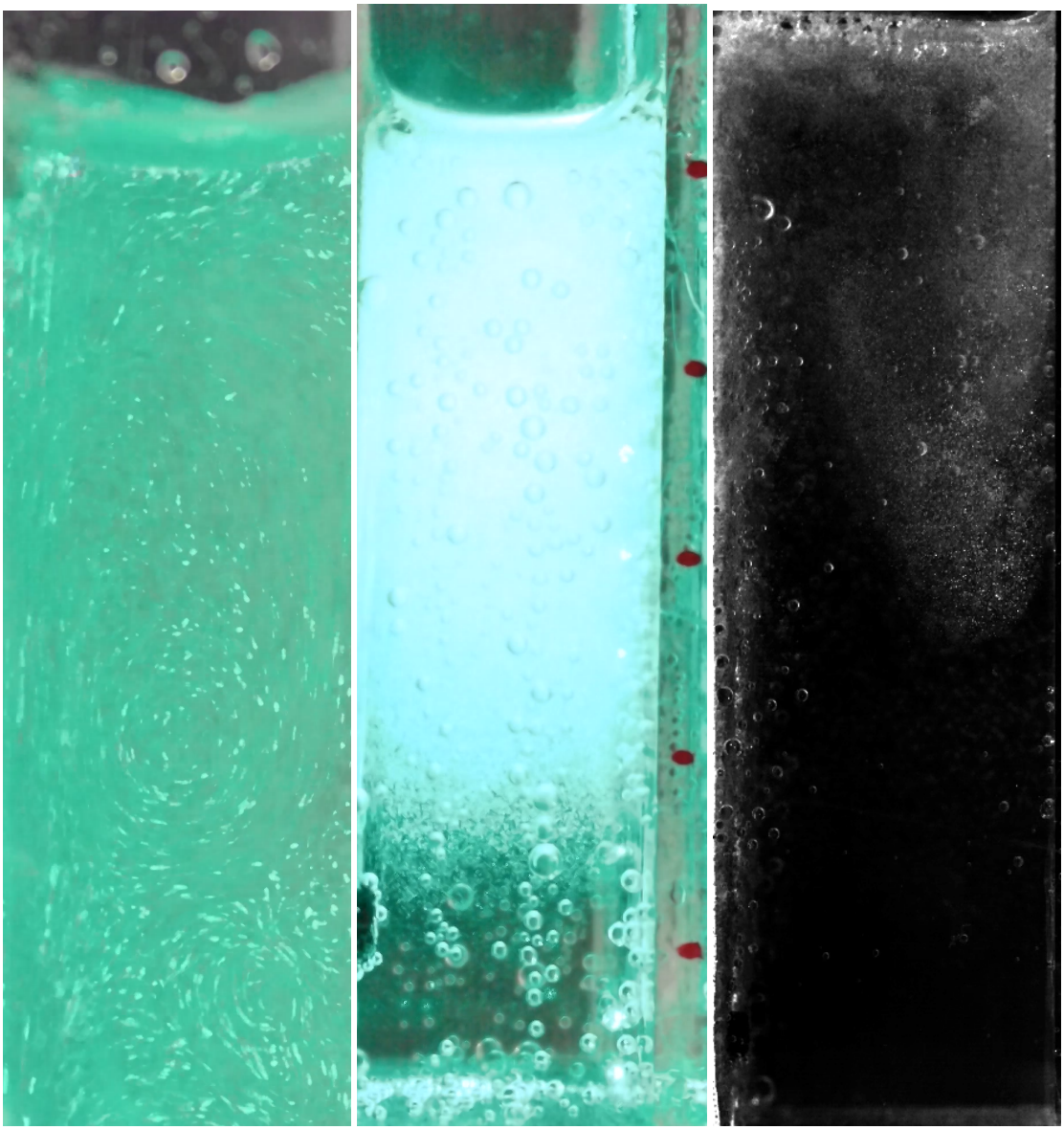

(a) Vortex formation in the bulk of the channel. Zp200736 electrode. Electrode-wall distance 1.2 cm. Current density 800 A/m^2

(b) Mist depth inside channel. Zp200736 electrode. Electrode-wall distance 1.5 cm. Current density 800 A/m^2.

(c) Bubble plume at cathode (left). Zp200705 electrode. Height 9.5 cm (full view). Current density A/m^2

Figure 3.1: Overview types of phenomena researched during the research project with (a) vortices observable at different heights along the channel, (b) the mist cloud reaching a certain depth inside the channel in fully developed state (60 seconds after applying current), and (c) a bubble plume originating at the cathode, filmed with a high speed camera.

4
Methods

In this chapter, the different sorts of experiments are outlined. The electrolyte used in these experiments is a solution created by dissolving 330 grams of 85% pure Potassium Hydroxide (KOH) in 5 liters of pure Milli-Q water [47]. This results in a 1M (∼ 5.3 wt.%) KOH solution, see below.

$$\text{KOH} : 56.1\ \text{g/mol} \xrightarrow{5\text{L}} \frac{280.5\ \text{g}}{0.85} = 330\ \text{g} \tag{4.1}$$

As a membrane, Zirfon is employed, specifically Zirfon PERL UTP 500, which is known to exhibit weaknesses when subjected to high voltages (approximately 10V). Fortunately, the conditions in this research project will not reach such high voltages. Furthermore, all cells housing the electrode pairs and KOH solutions are made by PMMA (Polymethyl Methacrylate) plates. These are KOH resistant [48] and see-trough to ensure good lifetime and vision on the experiment. Acryfix is used to glue these plates into an electrode pair holding cell as this glue is alkali resistant as well.

Multiple types of electrodes are examined using Particle Image Velocimetry (PIV) and Ultrasonic Doppler Velocimetry (UDV), which is elaborated more on in section 4.1. The majority of electrode samples are provided by Veco [49]. These samples have been carefully chosen based on their ability to stand independently and remain upright, along with their relatively low resistance. This minimizes hindrance from connection bolts or plates during the experiments. The characteristics of the used samples are given below in Table 4.1.

Table 4.1: Veco electrode properties.

Veco Electrode	Size (cm)	Thickness (µm)	Hole Size (µm)	Hole Shape	Open Area (%)	Resistance (Ω) for (100 x 1) cm
ZP200699	8 × 21	300	320 × 230	diamond	28	0.1186
ZP200705	3 × 15	900	320 × 230	diamond	28	0.0799
ZP200736	3 × 15	600	270 × 470	slotted	41	0.0920

As discussed in section 2.2, the maximum allowed current for these electrodes should be calculated by equation (2.7). The value for $R_{\text{electrode}}$ is calculated by:

$$R_{electrode} = \frac{R_{\text{1m,1cm}} * L}{w_{\text{e}}} \tag{4.2}$$

With L being the length of the electrode in meters and w_{e}, the width of the electrode. This leads to the maximum current density to have homogeneous electron division, see Table 4.2.

Table 4.2: Maximum current densities Veco samples.

Veco Electrode	Size (cm)	Active Area (cm * cm)	Resistance (Ω) for (100 x 1 cm)	Max Current (A)	Max. Current Density (A/m^2)
ZP200699	8 × 21	8 × 15	0.1186	6.7	558
ZP200705	3 × 15	3 × 9	0.0799	5.2	1919
ZP200736	3 × 15	3 × 9	0.0920	4.5	1684

More properties regarding the electrodes can be found in the appendix, see Figure B.1.

The influence of the placement method of the electrodes on the membrane on the bubble formation is large. In this research, in order to get an unambiguously overview of altering the fore-mentioned parameters, the porous sides of the electrodes are placed against the membrane.

4.1. Data Analysis

To analyse the flow patterns and bubble movement, two different methods are examined. The Ultrasonic Doppler Velocimetry method and Particle Image Velocimetry. Ideally, both methods are employed in parallel to ensure a comprehensive and dependable understanding of various phenomena. The strategy aimed to harness both functions simultaneously, with each serving as a mutual check to enhance reliability. Unfortunately, the UDV method did not give promising results throughout the research project. While examining a bubble mist, it turned out that the gas bubbles strongly reflect the ultrasonic waves. If one has many particles (bubbles), these reflections may affect the ultrasonic beam in both intensity and shape. Therefore, PIV is chosen as the leading analysis technique in this research. Relevant details of the PIV method are given below.

PIV In order to get a more complete overview of the flow inside alkaline water electrolysers, Particle Image Velocimetry is a commonly used tool. This method examines actual movies for its analysis. These results are then compared to simulations for validation. To ensure good stable images, a setup is made to envision the whole cell, or parts of the cell along the cathodes surface. The common (simple) configuration when using PIV analysis is given in Figure 4.1. A power source supplies the potential over the electrodes in series with a multi meter to ensure desirable current densities. A laser sheet is created by making a slit close ($\sim$ 0.5 cm) to the wall (nearest to the camera). This results in bubble analysis at a certain depth in the channel and not all the bubbles in the electrolyte.

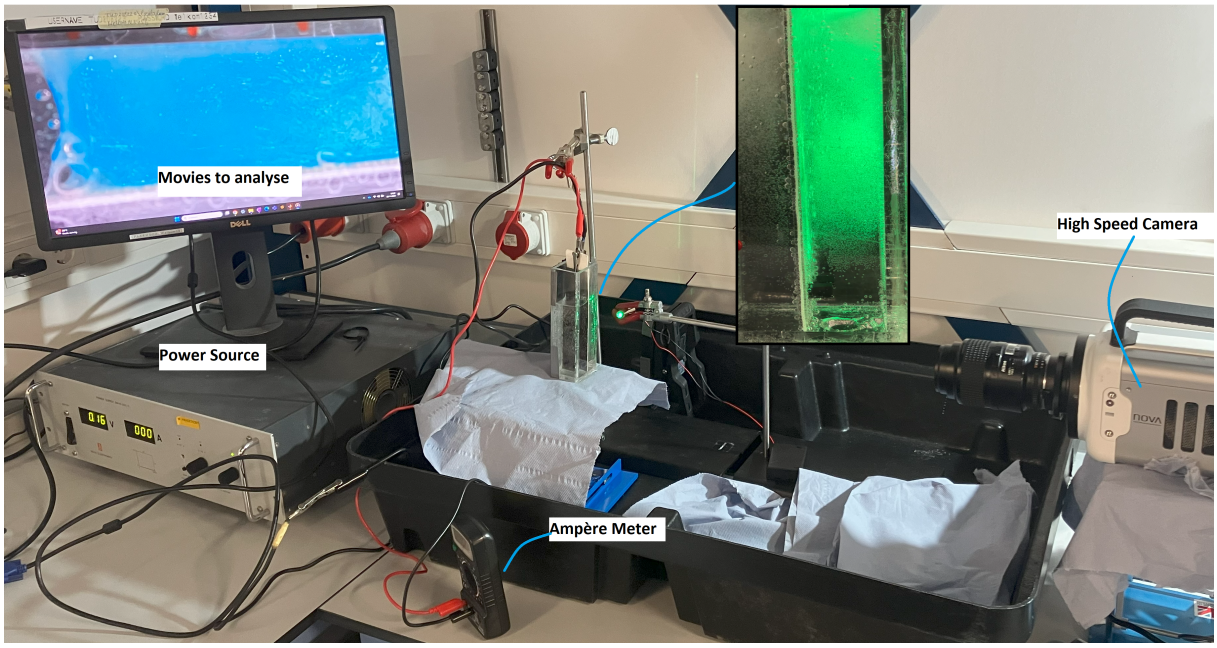

Figure 4.1: Overview of experimental setup.

With the help of a Matlab PIV script, moving bubbles can be detected and followed when comparing two successive frames of a movie. This way the direction of the bubbles is determined. From there, the fluid flow direction can be approximated as well. When reaching steady state, the average vector field is given over a number of frames, to establish the vortex formation. Additionally, the vorticity is given to enhance the overview of motions of bubbles. Vorticity, here ω [s^{-1}], is the measure of the rotation of a fluid element that moves trough the flow. Here ω is derived by $\omega_z = \frac{\partial v}{\partial x} - \frac{\partial u}{\partial y}$, with u and v being the displacement in vertical direction and horizontal direction respectively. The PIV method is used on

both a normal speed camera (with a frame rate of 30 frames per seconds) and the NOVA fastcam by Photron [50] which is able to go up to 12,800 frames per second. For high speed analysis, a trade-off is needed between light and the resolution. After analysis, a 1000 frames per second setting was found optimal for this camera. This way, the lens received enough light and it was possible to analyse bubbles individually. To summarize, the PIV method enables to get an overview of the flow by analyzing two subsequent frames and creates a vector field of bubble movement. This is done for low and high frame rates (30 to 1000 frames per second) to investigate its influence.

4.2. Vortex formation

To investigate the multiphase flow, the most important feature is the PIV analysis. For this, many movies are shot of different configurations in terms of current density, electrode height and distance from the cathode to the wall. All of these configurations are examined when having reached a fully developed state. This means a certain current is applied and after a minute, the movies are shot to perform PIV analysis. This does not mean that the process has reached a steady state. Analyzing the channels at a different timestamp will result in other vortex locations/directions or less activity visible.

The tested configurations are given below. Most of these configurations are tested with both a regular camera and the high speed camera. In section 5.1 the differences between the results for both cameras are outlined.

Table 4.3: Configuration analysed with PIV.

Electrode	**zp200705**	**zp200705**	**zp200736**
Electrode-wall distance	0.5 cm	1.0 cm	1.5 cm
Height	7.5 cm	7.5 cm	10.0 cm
Current Density (A/m^2)	200, 400, 800, 1600	100, 500, 1100, 1900	200, 400, 800, 1600

As PIV examines particles and not fluid flow, corrections must be made by accounting for the earlier described Stokes velocity in Equation 2.16. This is done by estimating the bubble size of hydrogen bubbles at the cathodic side and subtracting the presumed bubble rise speed (which moves in upward direction) over the whole frame. An example is given in Figure C.2. Here, it is seen that over the whole field a little subtraction is made. Note that apparently, the Stokes velocity is relatively small (1.1 mm/s for bubbles of 50 microns) in comparison with the actual bubble velocity (order of several centimeters per second along the cathode). Obviously, not all bubbles are the same size, and $v_{\text{Stokes}} \propto d_b^2$ so larger bubbles have significantly higher Stokes velocities. More on this is discussed in chapter 5.

Elastic Element In addition to investigating the effects of varying current density and electrode-wall distance, the impact of using an elastic element, as shown in Figure 4.2, is also explored. A comparison is made between a configuration where the elastic element is present at the cathode and another configuration without any elastic element. This comparison aims to gain valuable insights into how fluid dynamics within the electrolyte are influenced by the presence of the elastic element.

Table 4.4: Configuration analysed with PIV. This configuration is analysed for an elastic element attached to the cathode and a regular cathodic side.

Electrode	**zp200736**
Electrode-wall distance	0.6 cm
Height	10.3 cm
Current Density (A/m^2)	200, 400, 800, 1600

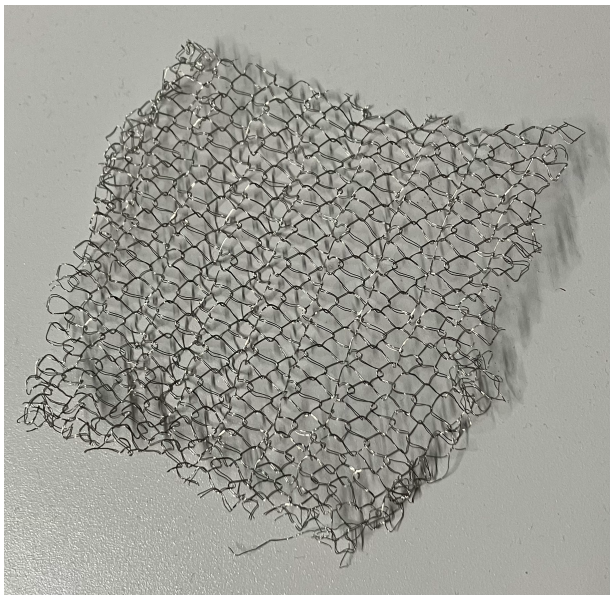

Figure 4.2: Elastic element used in channel in between cathode and opposing wall.

4.3. Mist height versus electrode-wall distance, electrode height and current density

One objective is to analyse the resulting bubble mist formation height versus the electrode-wall distance, electrode height and current density. For this analysis, the following configurations are examined, see Table 4.5. The current density used on the zp200699 electrode are 100-600 A/m^2 to ensure low voltage drop. To investigate higher current densities up to 1600 A/m^2, the zp200736 electrodes are used.

Table 4.5: Configurations Veco zp200699 and zp200736 for mist depth analysis

Electrode-wall distance (cm)	**Electrolyte Height (cm)**
1.0	9, 11, 13
1.2	14.5
1.5	9, 11, 13
2.4	14.5

(a) Zp200699, width 8.5 cm

Electrode-wall distance (cm)	**Electrolyte Height (cm)**
0.5	5, 10
1.0	5, 10
1.5	5, 10

(b) Zp200736, width 3.0 cm

The depth of this mist is analysed by determining the intensity of the light scattered by the different bubbles. Big hydrogen bubbles escape the electrolyte at the liquid-air interface. Smaller recirculating bubbles have different sizes and when bubbles are bigger they have a larger Stokes velocities and are trapped inside the vortex towards the cathode after they have travelled downwards at the opposing PMMA wall. A certain recirculating cloud would then be formed by bubbles of a certain size while smaller bubbles would be left underneath this cloud. The light intensity of this cloud is higher than that of the small bubbles below. Ideally, this means that we could link bubble size trapped into mist to current density, electrode-wall distance and height of electrolyte. To analyse the mist depth use is made of a Matlab script. Similar to the vortex formation analysis, the videos are recorded after reaching a fully developed state. As light intensity is crucial for this type of analysis, the analysis of a certain cell is done and only compared to cell configurations researched on the same time of day and same location in the lab space. This means that experimental results the zp200699 electrode experiments, see Table 4.5a, and results obtained from analyzing the zp200736 electrodes (Table 4.5b) can be difficult to compare.

4.4. Bubble Plume Analysis

For the analysis of the bubble plume originating at the cathode, a high speed camera is used. With capabilities of capturing up to thousands of frames per second, is it possible to detect bubbles independently. The images of the bubble plumes are subjected to both PIV-script as the average intensity script used for the mist depths. As these are both only convenient for average overviews of situations, discrepancies as big bubble trajectories are analyzed by reviewing footage and discussed when relevant. The influence of the elastic element on individual bubbles is reflected upon as well. This discussed in subsection 5.1.2. The intention was to identify the most effective strategy for analyzing different features of the bubble plume by exploring the various methods.

5
Results

In this chapter the results obtained from the experiments described in chapter 4 are given. The results of the vortex formation experiments, combined with elastic element examination, with the help of PIV are given in section 5.1. In section 5.2, the mist height for an electrode-wall distance of 0.5 to 2.4 cm are given while changing parameters like the exposed electrode height and current density. Findings resulting from the three-way bubble plume analysis are given in section 5.3.

5.1. Vortex formation

Firstly in Figure 5.1, an example is given of a vector field on top of an image of a certain cell. For all results the left of the figure denotes the cathode and the right indicates the opposing wall. The height of the channel is denoted by Z (mm). As the bubbles originate at the cathode and move in upward direction, we expect a velocity field towards the top in the figure at the cathode. In this example the initial liquid height was 7.5 cm (75 mm). We see that the liquid appears to be somewhat higher while filming the movies. This is a result of the volume rise which originates when applying power to the electrodes when the hydrogen and oxygen (gas) generation forms, as discussed in section 2.2.

In Figure C.3 in the appendices, an example is shown of an average velocity field of 10 frames shot by a 30 frames per second camera. This means the length of this analysis is 0.33 seconds. In Figure C.1, a 10 frame average of the 1000 frames per second (fps) camera configuration is shown. It is clear that averaging over a shorter period of time leads to better results in terms of vortex depiction. As the vortices arise and disappear (especially in the lower region of the channel) continuously and very quickly, a short measuring time is needed to gain relevant results. Taking an average over 0.33 seconds (10 frames) leads to a fairly random field of vectors without distinctive regions of motion.

5.1.1. Zp200705

Electrode-wall distance 0.5 cm Firstly, the zp200705 electrode with 0.5 cm electrode-wall distance is divided into three segments to allow better resolution of the movies. The segmented results are given below in Figure 5.2. For this low electrode-wall distance, bubble activity is present at low depths inside the channel. Only for 200 A/m^2 there is no bubble flow observed below 20 mm. Notable is that not only backflow at the opposing wall is occurring at this large depths. Even at 400 A/m^2, it seems that recirculation is taking place between 20 and 30 mm. This shows that at low electrode-wall distances, even at relatively low current densities of 400 A/m^2, vortices can from throughout the whole channel. This behaviour only gets amplified when examining higher positions in the channel. Clear vortices are visible at all current densities above 200 A/m^2. At high levels the top vortices are visible for all current densities, however at 1600 A/m^2, the top vortex is not clearly present, but the top region is filled with recirculating behaviour. At this current density, this behaviour stretches down to 20 mm above the bottom of the channel.

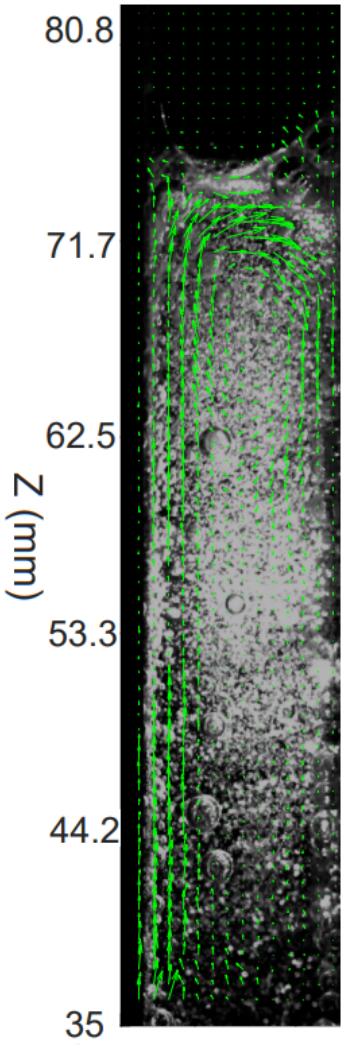

Figure 5.1: Cathodic side. 500 A/m^2. Captured at a frame rate of 1000 fps. Electrode-wall distance = 1 cm. Zp200705 electrode. 60 seconds after startup. Stokes velocity subtracted.

Electrode-wall distance 1.0 cm For an electrode-wall distance of 1.0 cm, we see in Figure 5.3 that with increasing the current density, the top vortex becomes more centered at the very top of the channel. This happens for the 1.0 cm case. However, for the various configurations at 0.5 cm we do not see the same pattern. Instead, we see several vortices at more random locations along the channel, especially at the higher (800 and 1600 A/m^2) current densities. Albeit smaller than the vortices at the top of the channel, in the bulk of the channel there is recirculating motion observable too. To emphasize this motion, the smaller vectors (lower speeds) in the figures are amplified to show the activity at lower heights in the channel as well. This can be seen in the appendices in Figure C.6, where typical movement in the bulk of the channel is visible at 500 and 1100 A/m^2. It is however visible that this activity in terms of recirculation does not resemble the 0.5 cm distance case, where at comparable current densities, more vortex formation was detectable.

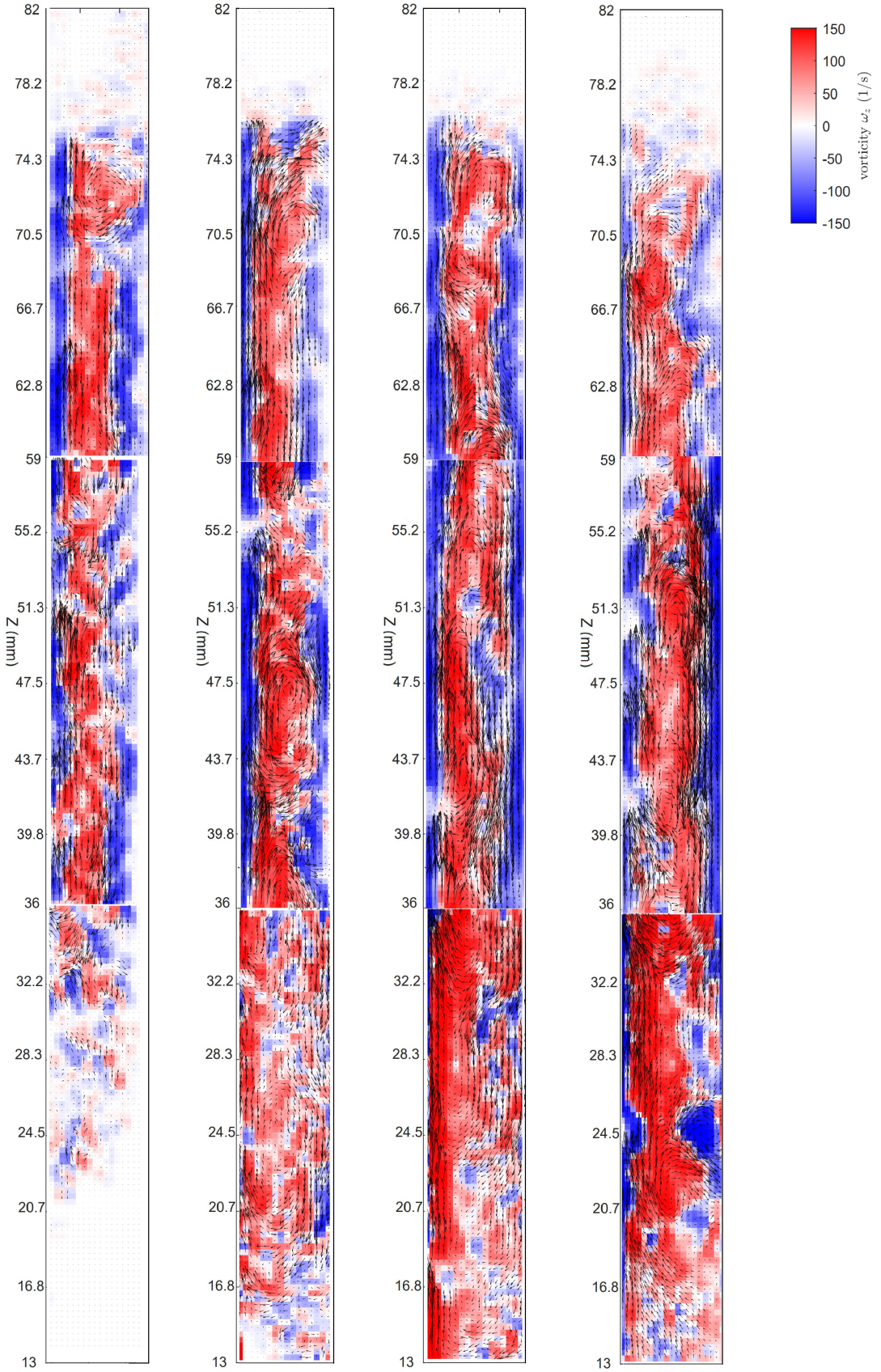

Figure 5.2: Cathodic side. From left to right: 200, 400, 800 and 1600 A/m^2. Electrode-wall distance 0.5 cm. The electrolyte level at 7.5 cm. Zp200705 electrode. 60 seconds after applying current.

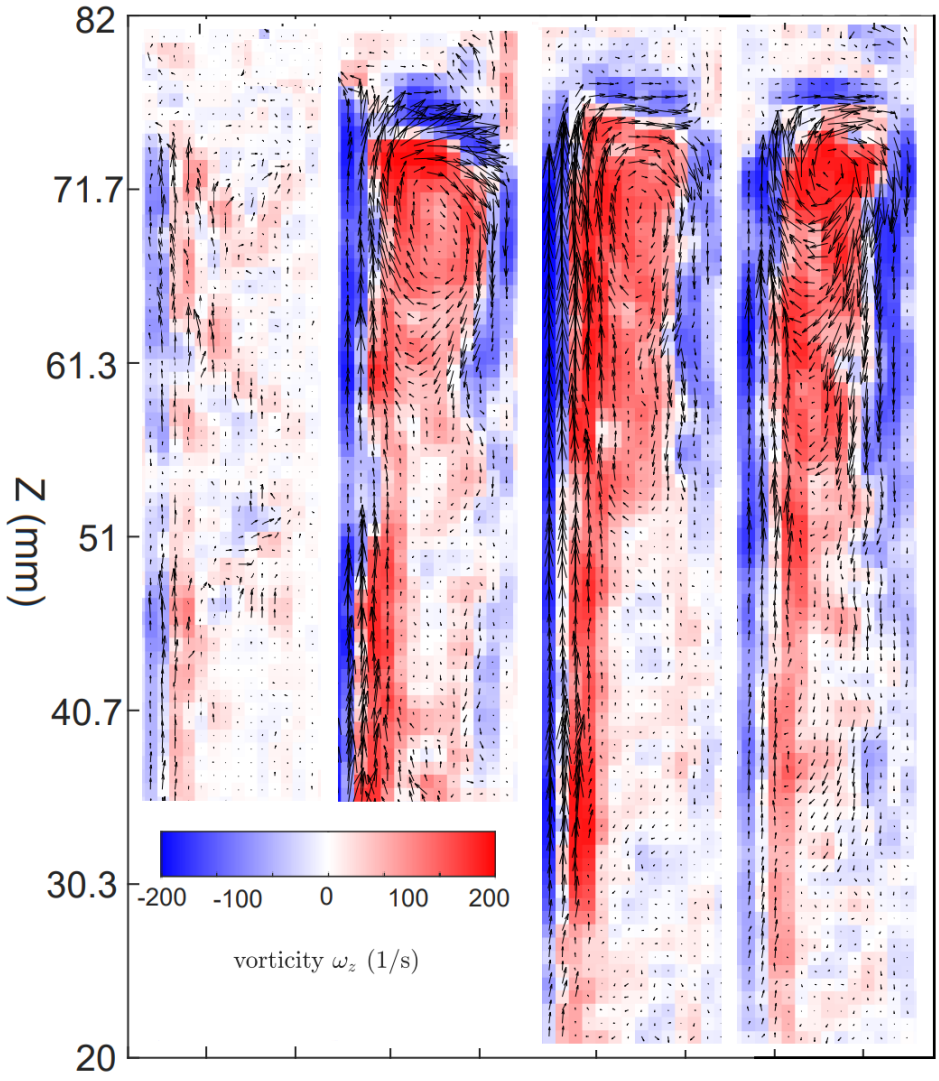

Figure 5.3: Cathodic side. Left to right: 100, 500, 1100, 1900 A/m^2. The electrolyte level at 7.5 cm. Electrode-wall distance 1.0 cm. Zp200705 electrode. 60 seconds after applying current.

5.1.2. Elastic element

Large electrode-wall distance configuration and elastic element Firstly, a comparison is shown for a 1.5 cm electrode-wall distance for current densities between 200 and 1600 A/m^2, see Figure 5.9 for the configuration with elastic element against the cathode. Here, an elastic element is placed against the zp200736 cathode but the channel is not entirely filled with the elastic element. The results of this comparison between an element-less and element configuration are given in Figure 5.4 and Figure 5.5 respectively. In Figure 5.4, we see that a relatively large current density of 1600 A/m^2 leads to the formation of a strong (high velocity) vortex in the bulk of the channel. What stands out is the difference in bubble vortex formation between the two configurations. From 400 A/m^2 on, several vortices in the channel without an elastic element can be depicted from the results. See Figure C.7, where lower depth vortices are noticeable at lower regions in the channel. These are absent in the same cases with the elastic element attached to the cathode.

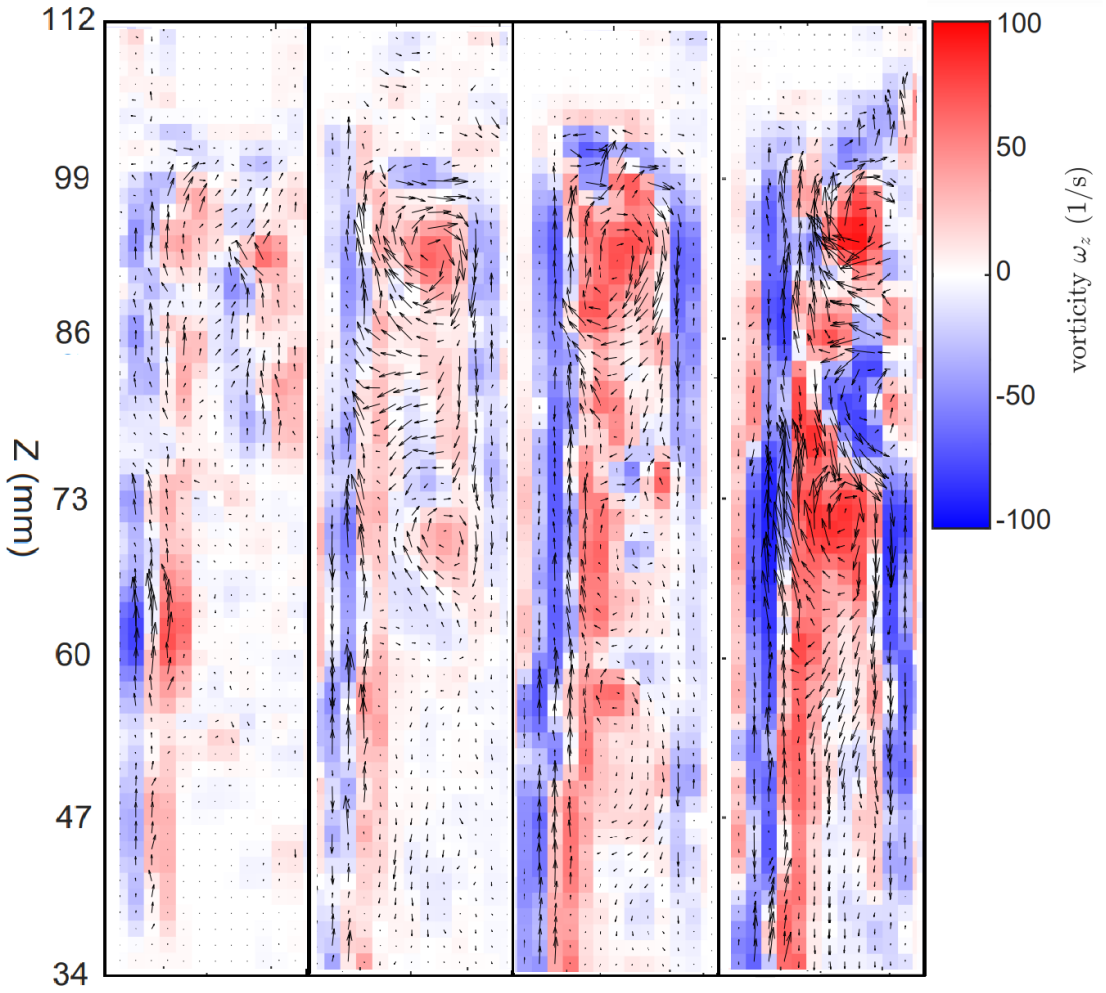

Figure 5.4: Cathodic side. 200, 400, 800, 1600 A/m^2. Electrode-wall distance 1.5 cm. The electrolyte level at 10.0 cm. Zp200736 electrode.

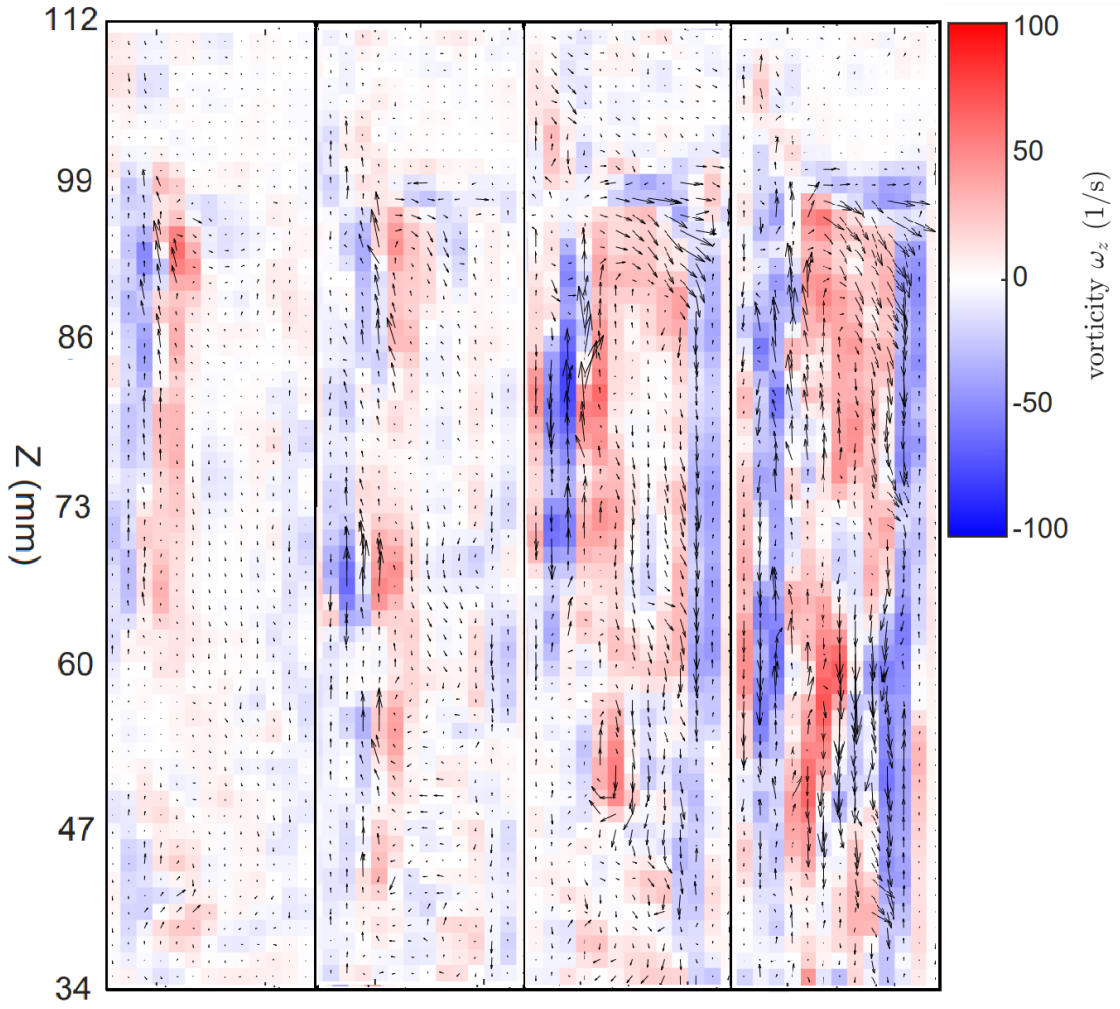

Figure 5.5: Cathodic side with elastic element attached to electrode at 200, 400, 800, 1600 A/m^2. Electrode-wall distance 1.5 cm. The electrolyte level at 10.0 cm. Zp200736 electrode.

Small electrode-wall distance configuration elastic element Secondly, an electrode-wall distance of 0.6 cm is examined and for this experiment the whole channel is filled with the elastic element. The results for the earlier described measurements are given in the figures in the appendices in Figure C.8 for the configuration without elastic element and Figure C.9 for the configuration with elastic element. Closer analysis of the 400 A/m^2 cases is given in Figure C.10. In both configurations at lower regions recirculating activity is present, where especially in around the elastic element centered vortices form. It seems even more of this activity is notable at the elastic element configuration. For 400 and 800 A/m^2, see Figure C.11, at higher positions along the cathode, more of these small vortices are spotted, which seem less present when no elastic element is in between the cathode and the wall. As discussed the assumed bubble diameter d is assumed to be 50 microns for all bubbles. This is a limitation and it is interesting to see the effect on the smaller (in terms of velocity) vortices. Therefore, the effect of assuming a bigger bubble size is examined on the small vortex positioned in the 800 A/m^2 channel of Figure C.11. The effect of having an assumed bubble size of 100 microns leads to a Stokes velocity of 0.45 cm/s which is a 4 times higher Stokes velocity. This larger upward velocity is subtracted from all grid points in the frame. In Figure C.12, the effect of this is significant, see the blue marked vectors for examples. Although the vectors are influenced by the shift in bubble size, even the small vortices are still noticeable, albeit less significant. Additionally, the centre of the vortex (green dot) in the 100 micron case seems to be shifted a bit more towards the cathode. Even bigger bubbles sizes and therefore bigger Stokes velocities can lead to different results.

Except for these small differences, we see that no significant distinctions can be made between the reg-

ular configuration and the one with the elastic element between the cathode and the wall, at least when considering the average vector field for an electrode-wall distance of 0.6 cm. In conclusion, when the electrode-wall distance increases, as in in Figure 5.5, much fewer vortex formations occur in the elastic element configuration than the regular cathodic side case. However, for lower current densities in the 0.6 cm configuration, this pattern is less pronounced, and even more small vortices are observable for the elastic element case.

Big bubbles Visually some observations can be made. Bigger bubbles have a higher chance to get stuck inside the elastic element or between the electrode and the element. This impedes smaller bubbles (and fluid itself) from following their initial direction causing these smaller bubbles to deflect as well. This behaviour is illustrated in Figure 5.6. It is interesting to investigate the influence of bubble coalescence in a manner where eventually, a bubble covers a significant portion (around half the width) of the channel, similar to slug flow as described in section 2.2. In Figure 5.7, the effect of a bubble on the fluid below itself is visible. Here the bottom of the frame denotes the cathode, and bubbles rise towards the liquid-air interface towards the left. This video is filmed in the same circumstances as the 1600 A/m^2 case in Figure C.8. The passing of the large rising bubble causes the liquid in its path to create space and be drawn underneath (to the right in the figure) the bubble. This is caused by the pressure difference in the channel between the fluid behind and in front of the bubble (where the pressure is higher at that moment). In Figure 5.8, it is visible that the bubble flow at the cathode indeed goes in the opposite (downwards) direction compared to a situation without big bubbles. Behind large bubbles, bubble vortices arise as well. We also see an uniform upward flow direction well behind the bubble (see the bottom snapshot in Figure 5.8). In addition to larger bubbles getting trapped, they frequently collide with the element, leading to a change in their direction. Subsequently, these larger bubbles follow a meandering path. To indicate this, an example is made of this situation without the opposing wall nearby the cathode Figure 5.9. This way, the bumping is clearly visible. At the bottom, we see a large bubble getting detached from the elastic element entering "free" electrolyte. It remains close to the cathode until it finds the elastic element again and starts a wavy trajectory.

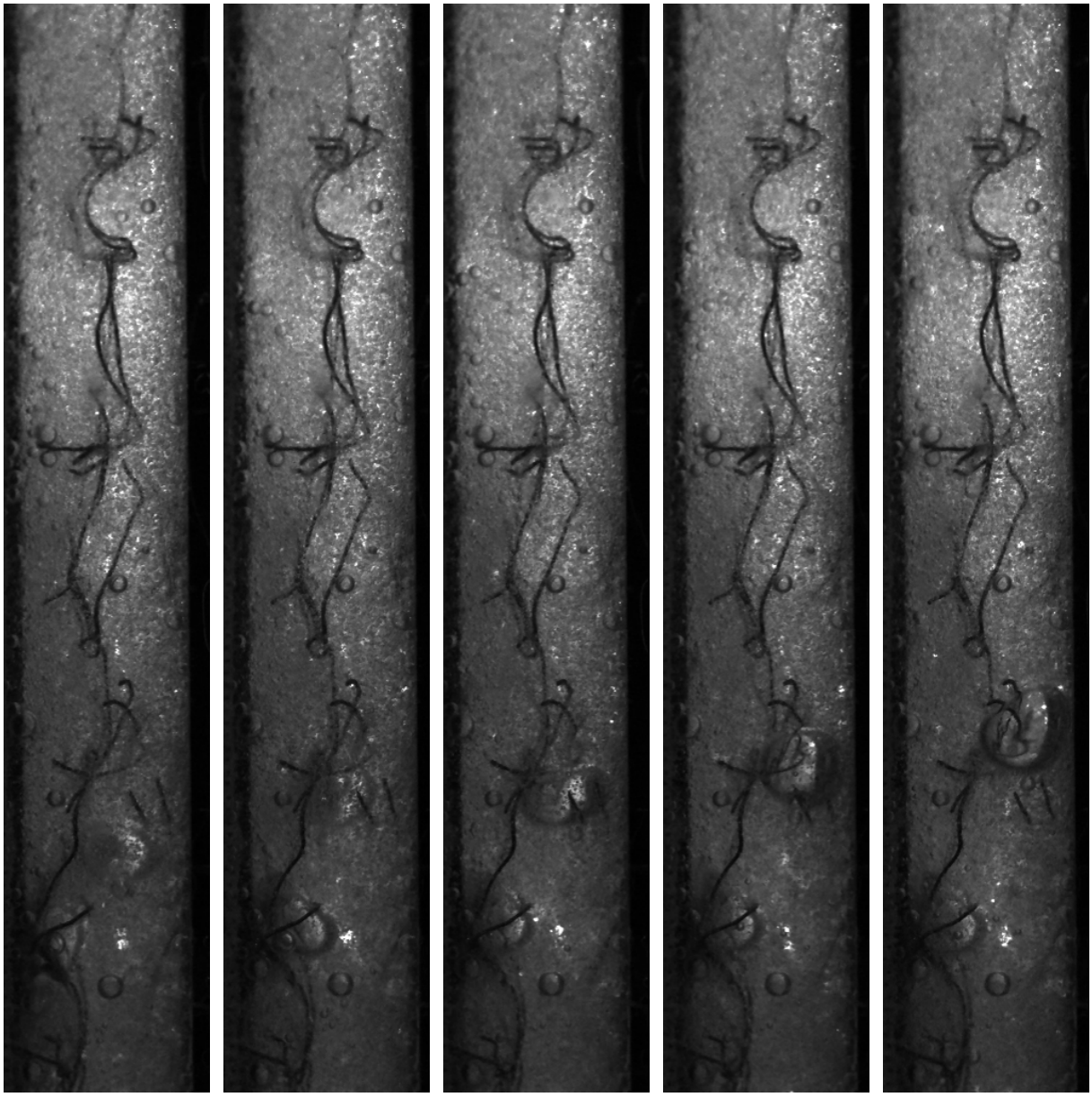

Figure 5.6: Cathodic side. 1600 A/m^2. Electrode-wall distance 0.6 cm. Bubble encountering elastic element in bottom of channel.

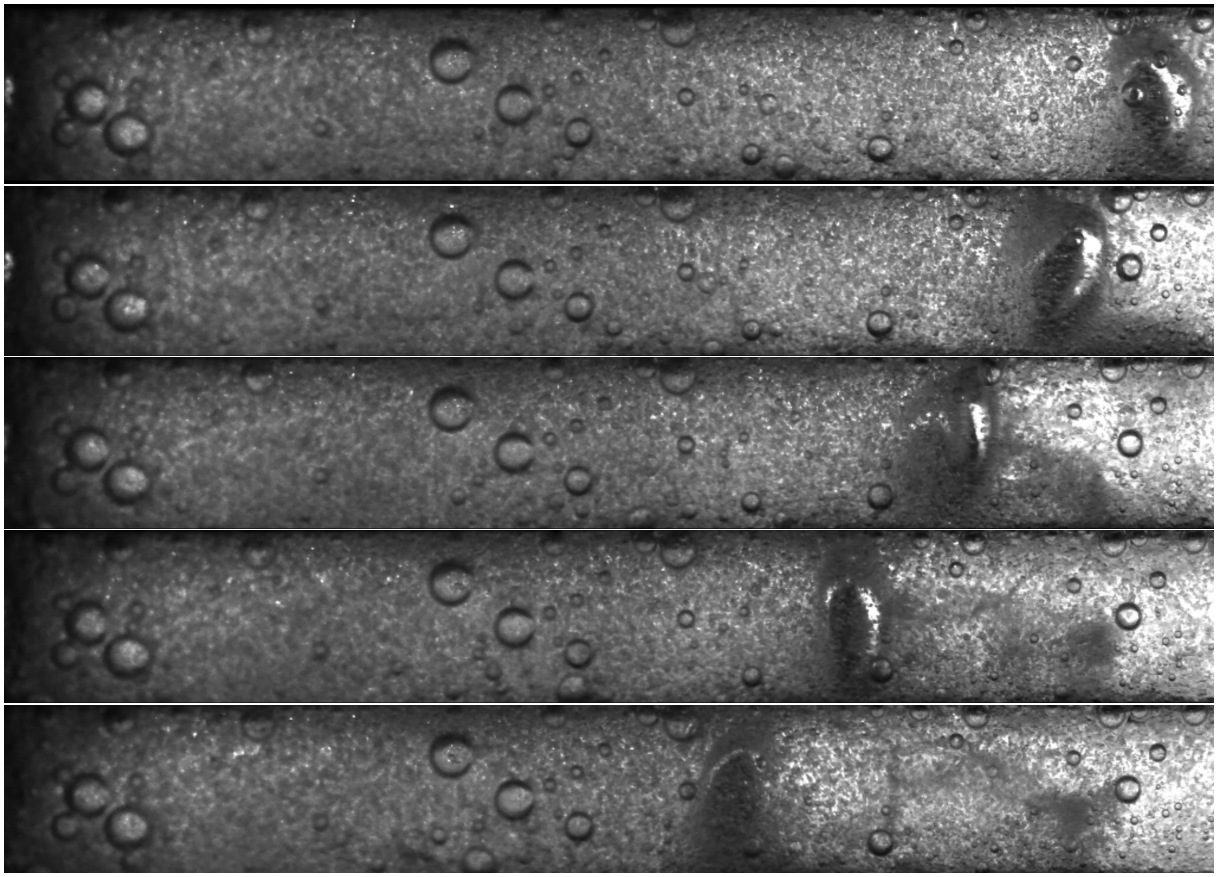

Figure 5.7: Cathodic side. Five different time stamps with big bubble propagating trough the channel upwards (left in figure). 1600 A/m^2. Electrode-wall distance 0.6 cm. 20 frames (0.02 seconds) in between successive frames. Zp200736.

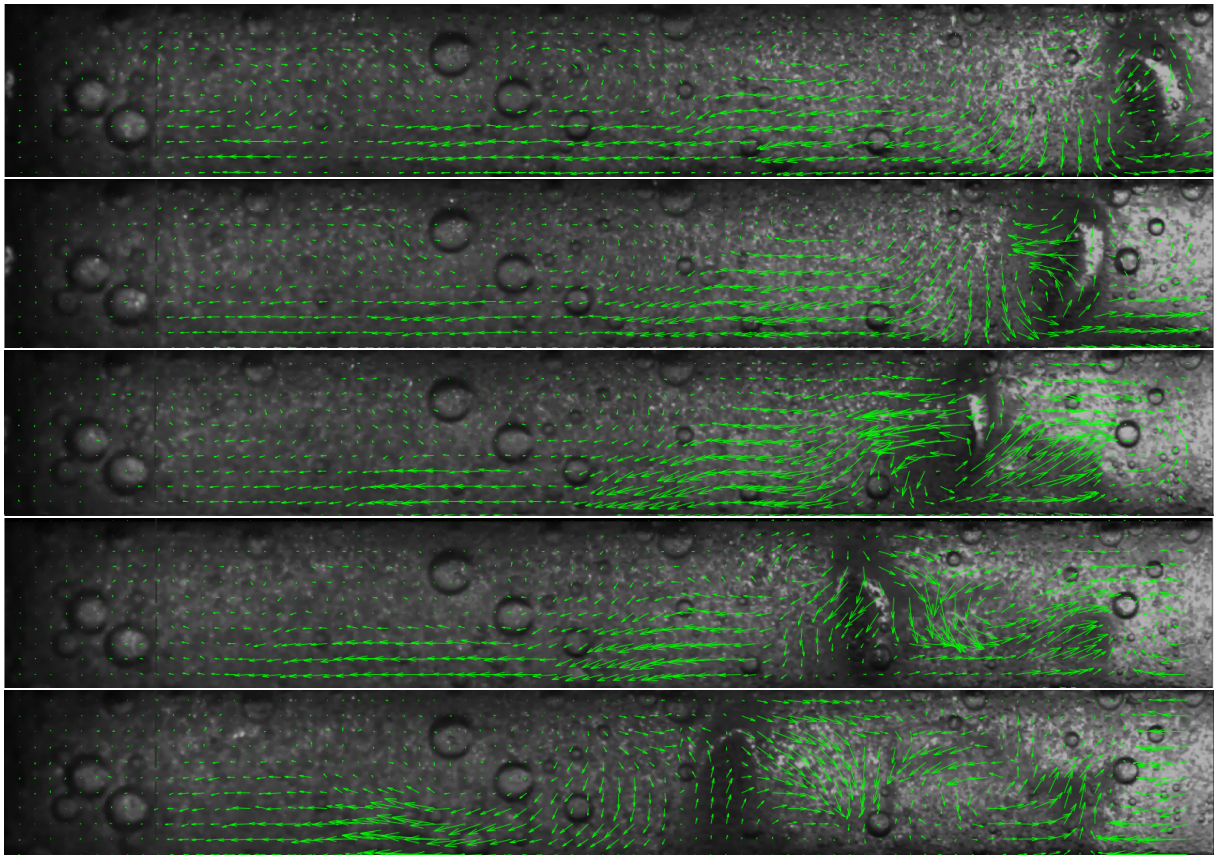

Figure 5.8: Cathodic side. Five different time stamps with big bubble propagating trough the channel upwards (left in figure). 1600 A/m^2. Electrode-wall distance 0.6 cm. 20 frames (0.02 seconds) in between successive frames. Effect on velocity field visible. Zp200736.

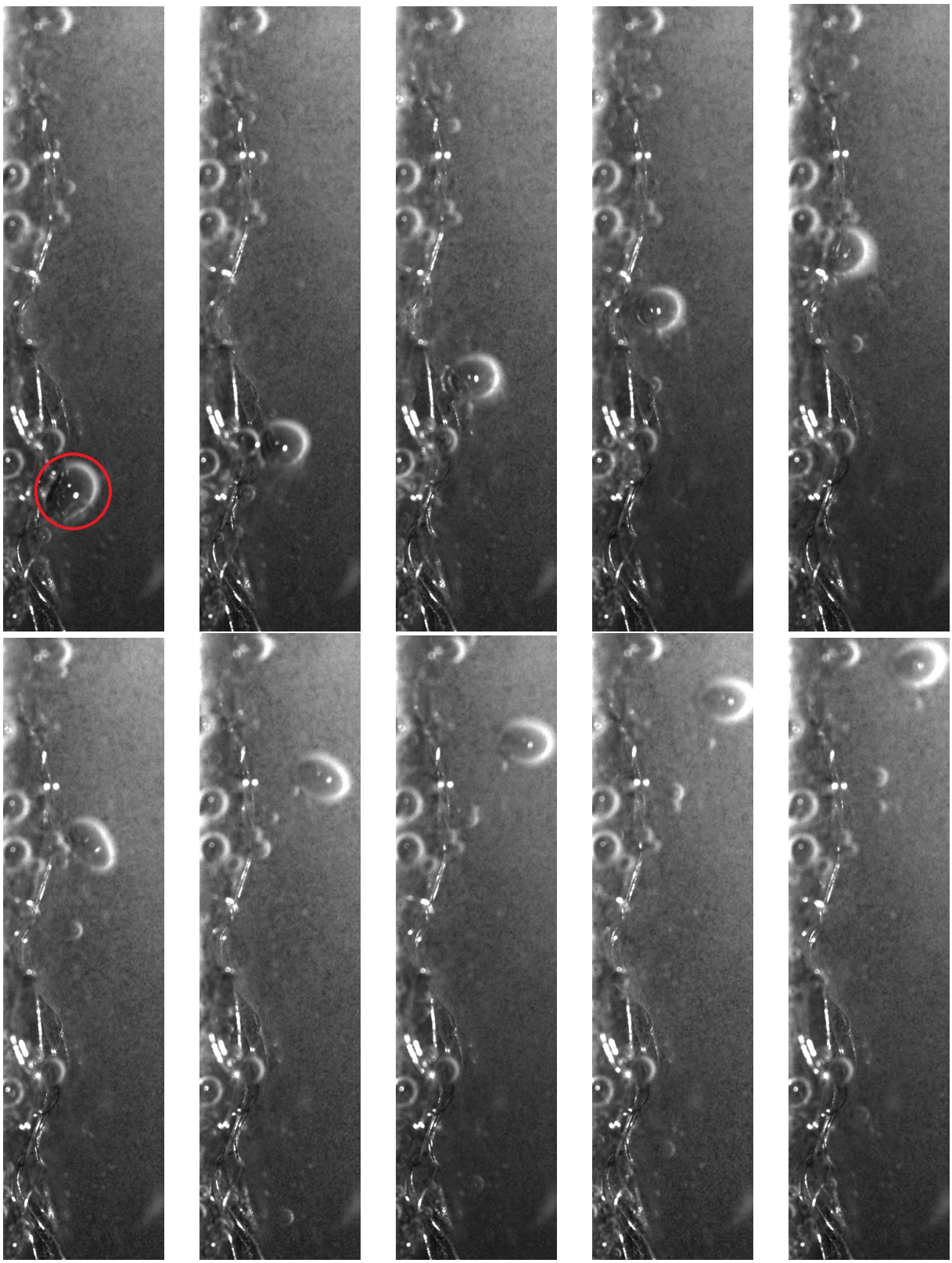

Figure 5.9: Cathodic side. Typical bump against elastic element. Current density of 1000 A/m^2. Large electrode-wall distance to have clear view of elastic element effect. Zp200736 electrode.

5.2. Mist height versus electrode-wall distance, electrode height and current density

In Figure 5.10, an example is given of a series of experiments. This configuration in particular is the zp200699 electrode pair with a distance of 1.2 cm from the cathode to the opposing wall. The electrolyte height is 14.5 cm. An illustrative example of the light intensity analysis can be observed in Figure 5.11. All the examined electrolysis configurations are given in Appendix D. These are used to determine the depth of all mist plumes. For the first set of experiments, the different vortex heights for the different configurations are shown in Figure 5.12. These are all made when analyzing the zp200699 cathodic side see Table 4.1. This analysis is done to see what the mist depth behaves like for low current densities. Most notable is that for the lower electrode-wall distance configuration, the mist reaches a relatively deeper level (ratio around 0.5 the electrode height) than the bigger electrode-wall distance configuration. Higher current densities are examined with the zp200736 electrode setup. When reaching higher current densities, see Figure 5.13b, the influence of changing the electrode-wall distance seems lower than that of changing height of the electrolyte. Additionally, we observed that the mist depth reached a maximum value at around 800 A/m^2, after which it seemed to stabilize. The mist never reaches the bottom of the channel. Obviously, these two different sets of experiments should not be compared thoroughly with each other, as the lighting and sets of electrodes differ. The shortcomings of this measurement method are elaborated on more extensively in chapter 6.

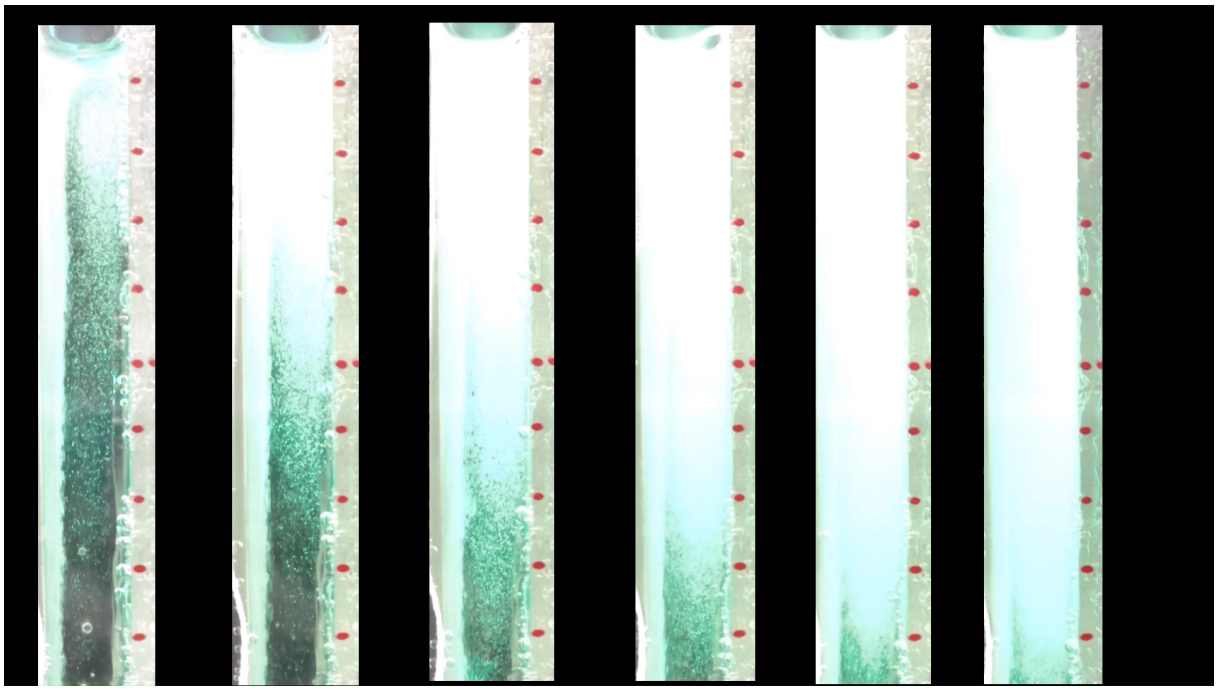

Figure 5.10: Cathodic side. Fully developed electrolysis, from left to right, 100 - 600 A/m^2. Electrode-wall distance 1.2 cm. Electrolyte height 14.5 cm. Zp200699 electrode. 60 seconds after applying current. Red dots denote centimeters.

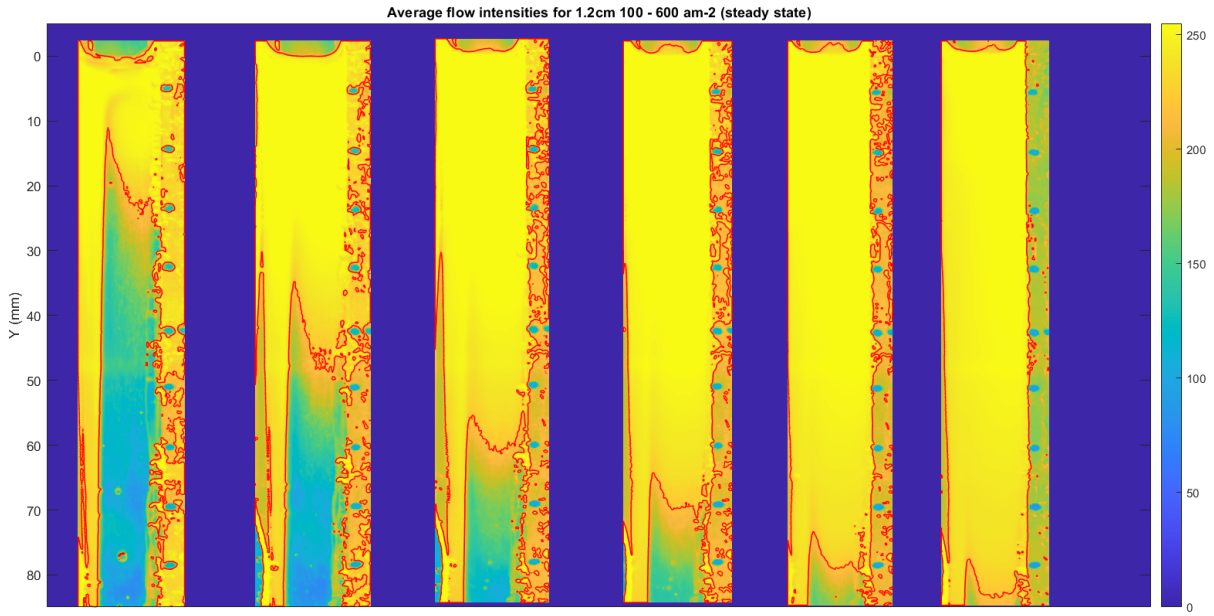

Figure 5.11: Cathodic side. Intensity overview of fully developed electrolysis, 100 - 600 A/m^2 with contour lines. Zp200699 electrode. Electrolyte height 14.5 cm. 60 seconds after applying current.

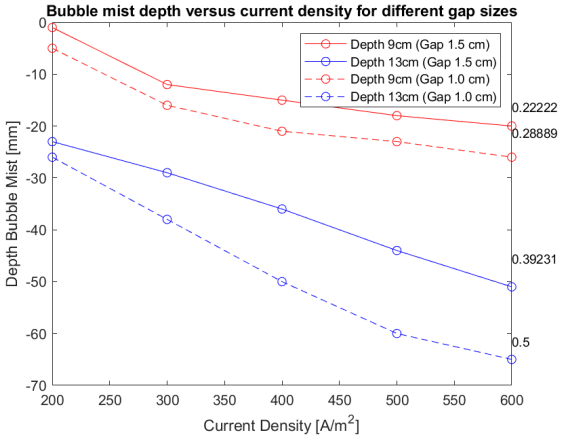

(a) Mist heights for the different electrode-wall distances 1.0 and 1.5 cm, different electrolyte heights (9.0 and 13.0 cm) for a range of current densities. The electrode is placed on the bottom of the cell. Zp200699 electrode.

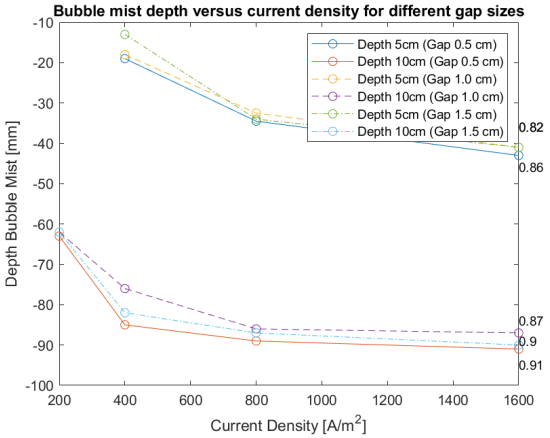

(b) Mist heights for the different electrode-wall distances 0.5 - 1.5 cm, different electrolyte heights (5.0 and 10.0 cm) for a range of current densities. The electrode is placed on the bottom of the cell. Zp200736 electrode.

Figure 5.13: Comparison for lower current densities up to 600 A/m^2 (a) and higher current densities to 1600 A/m^2 (b). The ratio of the maximum depth divided by the channel depth is provided next to the respective value.

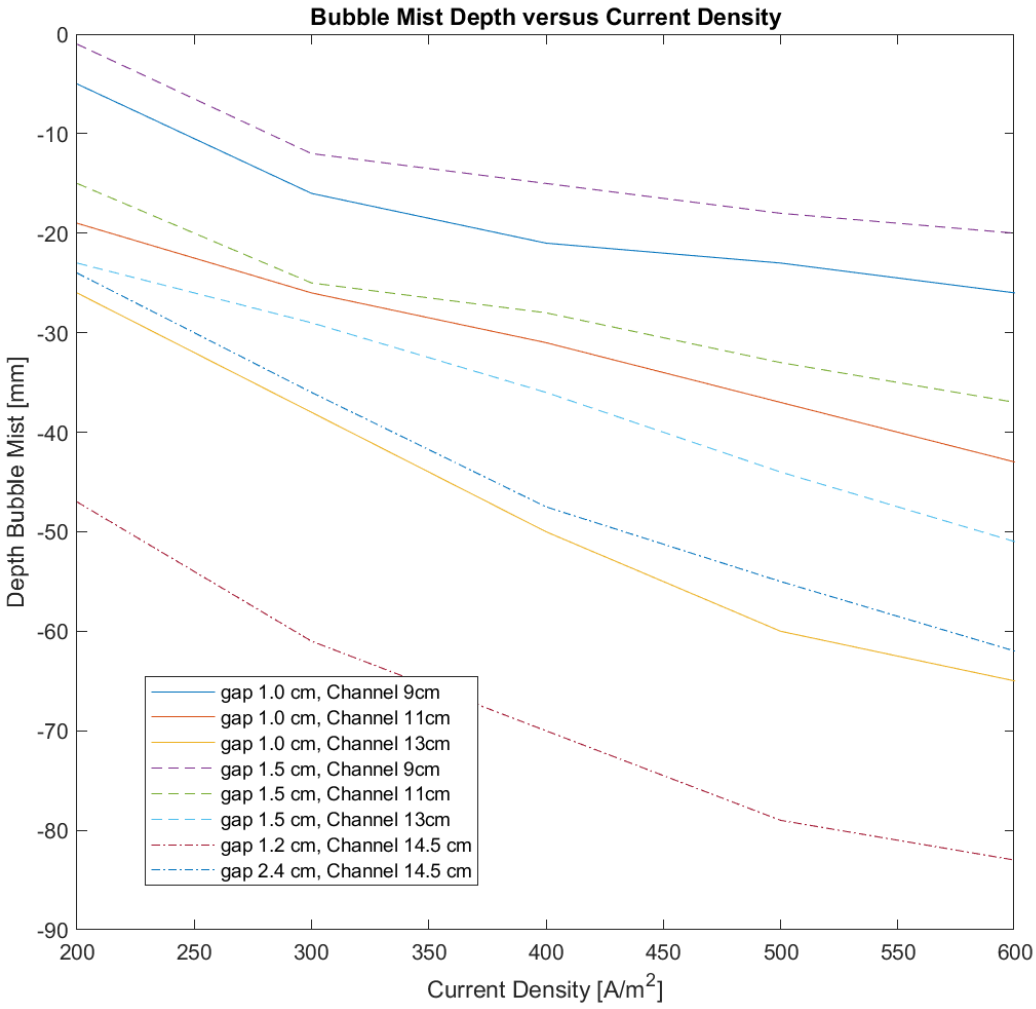

Figure 5.12: Mist heights for the different electrode-wall distances 1.0 - 2.4 cm, different electrolyte heights (9 - 14.5 cm) for a range of current densities. The electrode is placed on the bottom of the cell.

5.3. Bubble Plume Analysis

With the help of the high speed camera both PIV tracking and the average light intensity method have been examined. In Figure 5.15, the bubble plume created by analyzing the light intensity. In Figure 5.16, the results of 200 and 550 A/m^2 are given from analysis with the PIV strategy. Albeit difficult to quantify, it is clearly visible that for the different current densities, different heights can be depicted as heights where turbulent behaviour occurs. Besides computational analysis, the movies are also analysed visually to depict abnormalities or on the other hand structural phenomena happening at certain configurations. For different heights along the zp200699 cathode, the bubble plumes are given in Appendix E. These plumes are examined for current densities of 20, 70, 200 and 550 A/m^2. Some configurations showed abnormalities that need to be in discussed in particular. Already at a relatively low height between 5 and 8 cm high, at 550 A/m^2, irregularities were found when analyzing the plumes more thoroughly, see Figure 5.14a. It is clear more of these 'bursts' are occurring for higher current densities, which might be caused by turbulence in the channel. It is too inconsistent however to link these turbulent phenomena to any of the parameters (height, current density or electrode-wall distance).

Bubble trajectories A detached larger bubble's trajectory is shown in Figure 5.14c. The earlier described meandering path is again visible, here with an amplitude of approximately 0.5 cm and a wavelength between 2.5 cm and 3.0 cm. The estimated bubble diameter is 2.1 mm. The rise velocity is around 20 cm/s. For a higher current density of 2000 A/m^2, the bubble trajectory of a 1.8 mm bubble consisted of an amplitude of 0.3 cm, a wavelength of 2.0 cm and an upward velocity of approximately 18 cm/s. These trajectories are in agreement with earlier findings of Baczyzmalski [25], described in subsection 2.2.2, although the velocities of the big bubbles at higher current densities are slightly higher than the corresponding bubble velocities found in Figure 2.7.

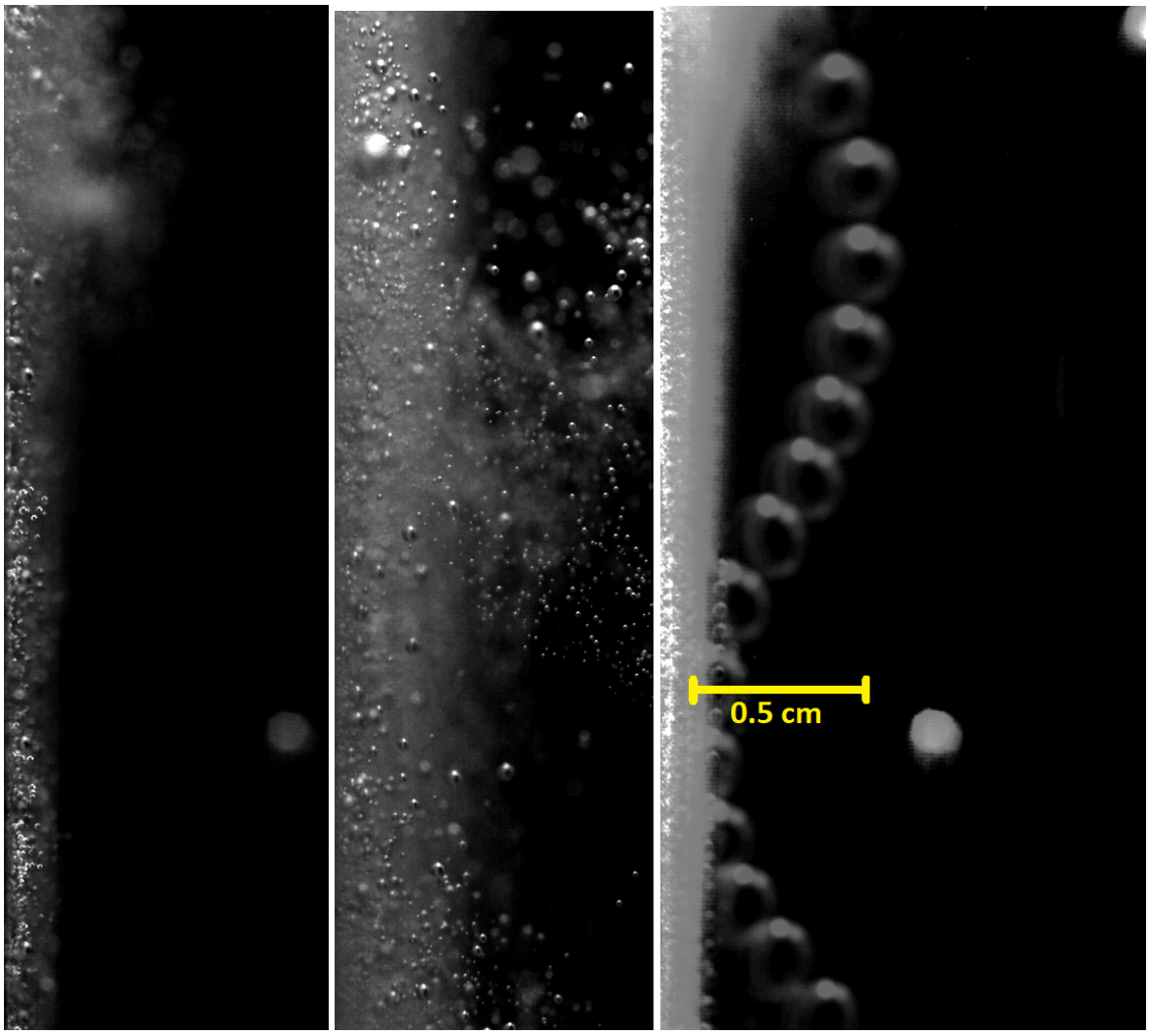

(a) Bubble burst in bubble plume 5-8 cm

(b) Bubble burst in bubble plume 11-14 cm

(c) Big bubble trajectory at 5-8 cm

Figure 5.14: Zp200699 cathode. Irregularities in the form of bubble bursts at different heights along the cathode at 550 A/m^2. A large bubble ($\sim$ 2.1 mm) trajectory is shown in (c). Time between first and last frame equals 0.15 seconds

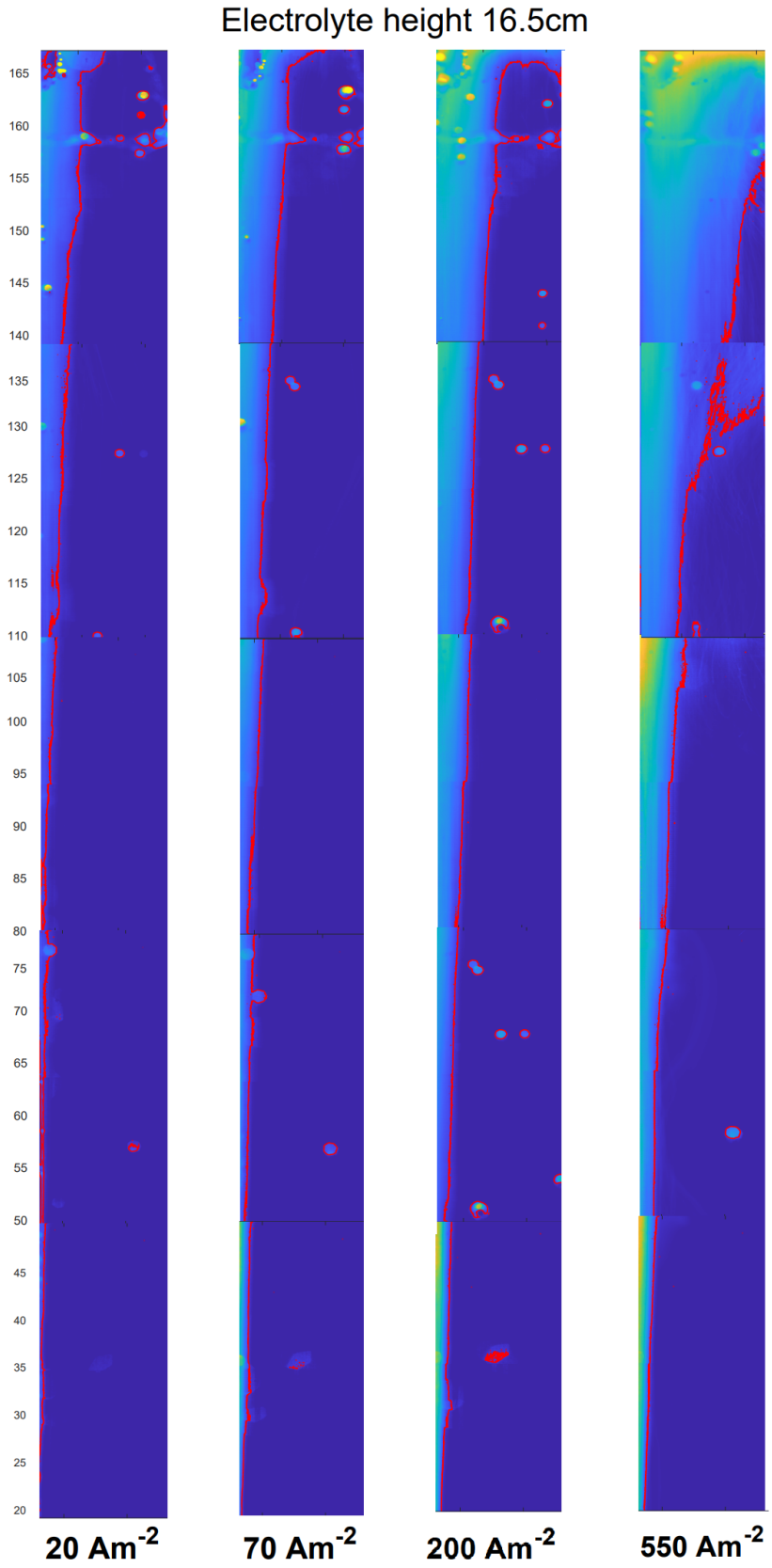

Figure 5.15: Cathodic side. Bubble plume when using the average light intensity over a whole 0.6 second movie. Electrode-wall distance large (∼ 3 cm) to prevent back-flow interference. Zp200699 electrodes.

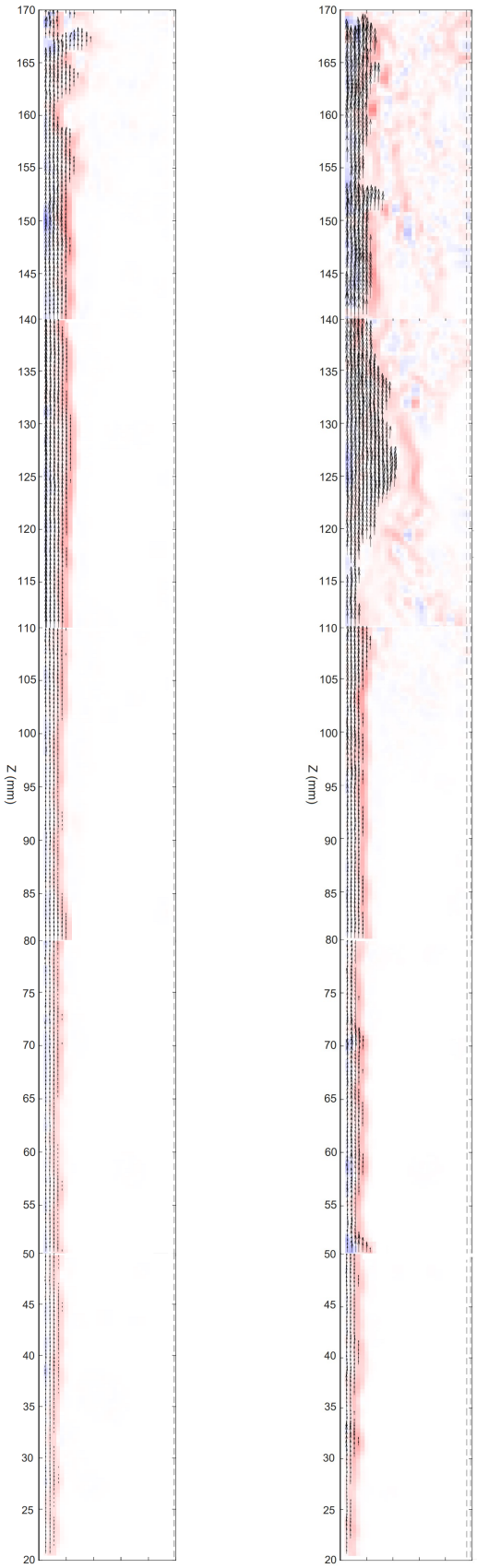

Figure 5.16: Cathodic side. Bubble plume PIV. Current densities of 200 (left) and 550 (right) A/m^2. Electrode-wall distance large ($\sim$ 3 cm) to prevent back-flow interference. Zp200699 electrodes.

6
Conclusions and Discussion

6.1. Conclusions

Vortex formation For this part of the research the research question is:

- How does manipulation of current density, electrolyte height and electrode-wall distance influence the quantity, size, and shape of vortices within the electrolyte during zero-gap water electrolysis?

First of all, there are various conclusions that can be made. The PIV method is a convenient tool to track bubbles in electrolysis, when working with ambient lighting and/or a laser, depending on the purposes of the measurements. Highly recommended, especially for analysis of higher current densities (> 400 A/m^2), is the use of a high speed camera with capabilities of at least around 1000 fps to be able to track single bubbles. With the help of PIV, some knowledge is gained concerning the formation of vortices at the cathodic side of alkaline water electrolysers. Bubble vortices are notably present at the top of the channel in many of the examined configurations. Analyzing fully developed electrolysis configurations showed a significant number of vortices visible in the lower regions of the channels as well. In general, a lower electrode-wall distance resulted in more recirculating activity throughout the channel. This is clear when comparing similar current densities for the cases of 0.5 and 1.0 cm with equal electrode heights of 7.5 cm, see Figure 5.2 and Figure 5.3 respectively. Additionally, in these figures, we see that higher current densities lead to more activity in the bulk (lower region) as well and caused bubble circulation at deeper levels within the channel. It becomes clear that the top vortex becomes denser and smaller at higher current densities when having a larger electrode-wall distance of 1.0 cm. This is clearly visible in Figure 5.3. In this figure there is also less activity noticeable in the bulk of the channel. Different current densities were also examined for a 1.5 cm electrode-wall distance. Here, a higher current density seemed to lead to more vortices in the bulk as well. However, also lower current densities showed vortex formation, see Figure C.7, albeit containing lower bubble velocities than the top vortex in such channels. The results when applying an elastic element against the cathode were significantly different. When performing the exact same measurement configurations, the elastic element seemed to counteract much of the activity in the bulk. Hardly any flow directions other than upwards or downwards are visible. For a smaller electrode-wall distance (0.6 cm) configuration, where the elastic element covered the entire cathode-wall distance, this was different. Especially when looking at lower velocity regions, lots of small vortices where present in the bulk, also at lower current densities of 400 A/m^2. While the vortex formation experiments have provided some insights, it remains challenging to establish a direct correlation between specific parameters and the stimulation or damping of vortices.

Mist depth analysis The second research question of this thesis is:

- How do variations in electrode-wall distance, current density, and electrode height influence mist height in zero-gap electrolysers?

Some observations can be safely obtained from the bubble mist depth measurements. We see that bubble mist increases (gets deeper in the channel) when increasing the current density. Also decreasing the electrode-wall distance leads to deeper mist plumes. Most interestingly, we see that increasing the height of the electrolyte directly leads to an increase in the mist depth as well. Even when dividing the mist depth by channel length, this ratio is biggest for larger electrolyte heights. When analyzing the larger current densities with the other electrode pair (zp200736 electrodes with slotted apertures instead of the diamond apertures in the zp200699 electrodes), there is almost no distinction between the bubble

mists when varying the electrode-wall distances. As we do not even see big differences for this electrode pairing in their influence on mist depths when altering electrode-wall distances at lower current densities, we can conclude that the differences in measurement circumstances and configuration cause the lack of reproducibility. Gas bubbles can recirculate to 90 percent of the channel depth in certain configurations. The bubble mist never reaches the bottom of the channel during examining the configurations in this research.

Bubble plume analysis The final research question:

- How does varying parameters like current density and height along the cathode influence the thickness of the bubble plume originating and turbulent behaviour?

Firstly, we see what we would expect from rising bubble plumes as they grow thicker with increasing height along the cathode, see Appendix E. The thickness of the bubble plume is also influenced by increasing the current density. Additionally, some turbulent behaviour is definitely observed, especially at higher current densities. After analyzing some separated larger bubbles, agreement was found with earlier studies regarding amplitude and wavelength of the wavy trajectory of these bubbles. Regarding analysis strategy, the PIV method tracking individual bubbles gives a decent overview of the bubble plumes thickness and the overall stability of the plume versus height, see Figure 5.16. It is however not easy to depict a certain height where turbulence instigates. Additionally, implementing the average intensity of light seems a promising method to facilitating the analysis of these plumes. Intriguing was analysing bubble trajectories visually to get an overview of several discrepancies like big bubble trajectories or bubble burst, which seem to indicate turbulent behaviour. These can be missed if just analyzing movies computationally.

6.2. Discussion and Further Research

Vortex formation When analyzing the average velocities over 0.01 seconds, many vortices and interesting behaviour can be depicted. However, it remains the question to what extend these vortices in the bulk can be linked to turbulence. The lower electrode-wall distances result in less reproducible results in terms of concrete conclusions, but that can actually be caused by occurrence of turbulent behaviour. There are also some practical limitations to the PIV method. Firstly, the Stokes velocity is subtracted from the average flow field. A certain bubble size (50 microns) is assumed here for all bubbles. Assuming one bubble size is obviously a big limitation to the validness of the results, as we see that even a bubble size of 100 microns already has effect on the depicted vortices in Figure C.12. Therefore, a separate bubble recognizing script should be implemented on the videos. This way, a more accurate Stokes velocity can be subtracted from the bubble velocities to create values closer to the fluid velocities. Being able to recognize bubble sizes helps researchers to accurately model bubble and fluid flows in the future. Additionally, at locations in the channel where no bubbles are present, there is a vector added in the current script. Another issue is the lighting helping the experiments. For an accurate view of one sheet of bubbles a laser is used. This sometimes caused issues as the light of the laser was centered at the point closest to the source, which led to brighter mist in the bulk of the channel. A more versatile light source may improve the images. When the script is updated for bubble tracking and a light sheet is evenly spread, further research can really extend the created data during this project. As we want to accurately link parameters like electrode-wall distance, electrolyte height and current density to vortex formation or turbulent behaviour, these criteria are essential.

Mist depth analysis There are several shortcomings to the bubble mist experiments unfortunately. The use of two different sets of electrodes led to differences in basic findings. This means no universal conclusions can be made regarding adjusting the electrode-wall distance and the results on the bubble mist plume. As can be seen in the results, a certain brightness is set to compare different current densities. It is believed a certain size of bubbles correlates with the light intensity. Picking a slightly different value to calibrate the mist depth with, can lead to significantly other results. This might be the reason for the differences between the outcomes of the two separate experiments. Firstly, the lighting in the room where the second part of the experiments was performed was much less bright than the more ambient lighting present at the first experiment's location. Picking a brighter or less bright value for calibration can cause

different sizes of bubbles to be included as "mist". As mentioned, the different electrode pairing might lead to overall different sizes of bubbles and therefore different light intensities. Because of this, a different approach should be chosen. Due to the significance of bubble sizes for this part of the project, it would help if one would be able to fit a bubble recognition script on this as well.

Bubble plume analysis The plume analysis consisted of many unknowns towards the best strategy to analyze turbulent behaviour. The two predominantly used computational strategies leading to the vortex formation and the mist height results gave varying results in terms of quality. The PIV method did show qualities in tracking the width of a bubble plume. It shows turbulent behaviour but it remains unclear where exactly the bubble bursts or other turbulent phenomena occur when averaging over a couple of frames. When refining the average light intensity method, significant potential for improvement becomes evident. Again, a more evenly distributed lighting over the whole frame would be beneficial. Thereby, a high resolution camera that is able to film the whole cell at once (so not the segmented videos as made use of during this project), would lead to more reliable results. In the average light intensity figure, Figure 5.15, it is evident that there exists a disparity in brightness between the upper region of one frame and the lower portion of the subsequent frame. This discrepancy results in an uneven appearance of the plume at the point where two frames intersect. When having high electrode-wall distances, less recirculating bubbles interfere with the bubble plume, so if one is solely invested in bubble plume behaviour, a large electrode-wall distance compared to electrode height is beneficial. To gain actual correlations between parameters and turbulence in the form of bursts of bubbles out of the plume, much more movies and different configurations need to be tested.
In summary, to establish definitive correlations between parameters and turbulent behaviour, future investigations should conduct a wider range of experiments, varying electrode-wall distances, electrolyte heights, and current densities. Additionally, the use of a high-speed camera with full-view recording capabilities in combination with better lighting equipment will allow researchers to capture critical events, such as bubble bursts, contributing to a more in-depth understanding of turbulence in the system. A method to track bubbles and their sizes would be a significant improvement to this research.

Appendices

A
Gas Fraction

Figure A.1: Gas evolution in channels. Anodic (electrode-wall distance 6 mm) and cathodic (electrode-wall distance 5 mm) side at the left and right of the membrane respectively. Current densities of 100 (left), 1000 (middle) and 6000 A/m^2.

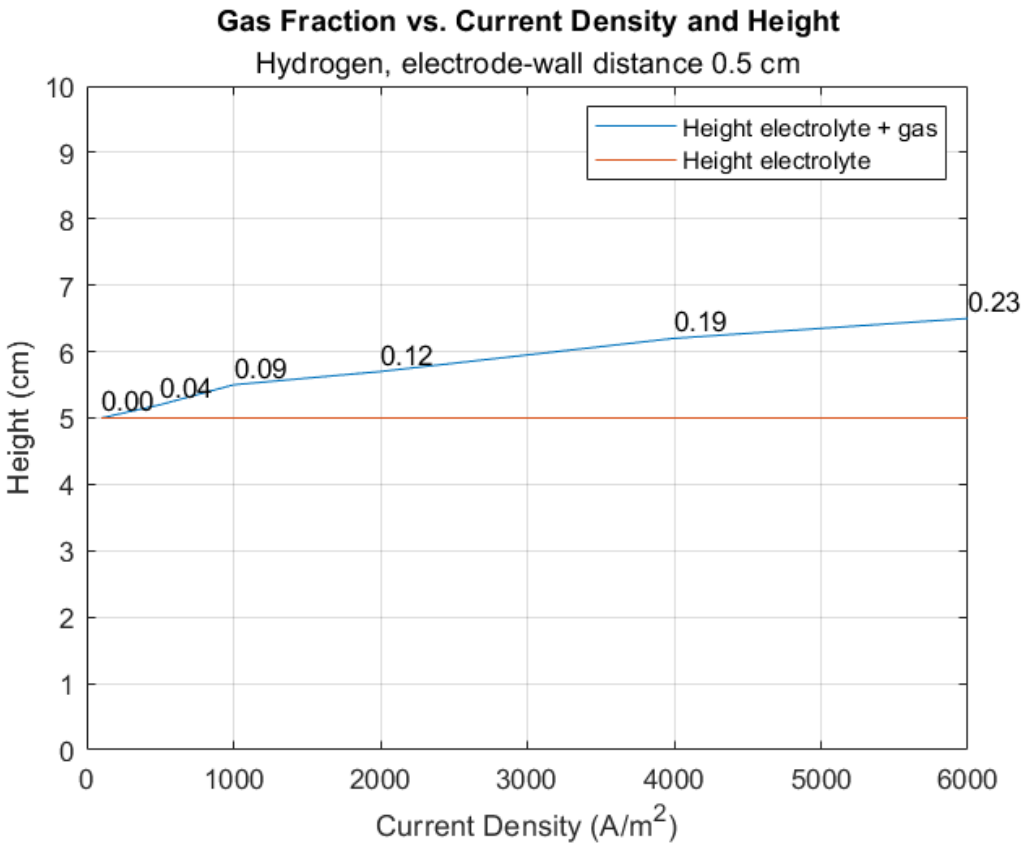

Figure A.2: Gas fraction ϵ for a range of current densities of 0 to 6000 A/m^2. Gas fraction values given at different j.

B

Veco Samples

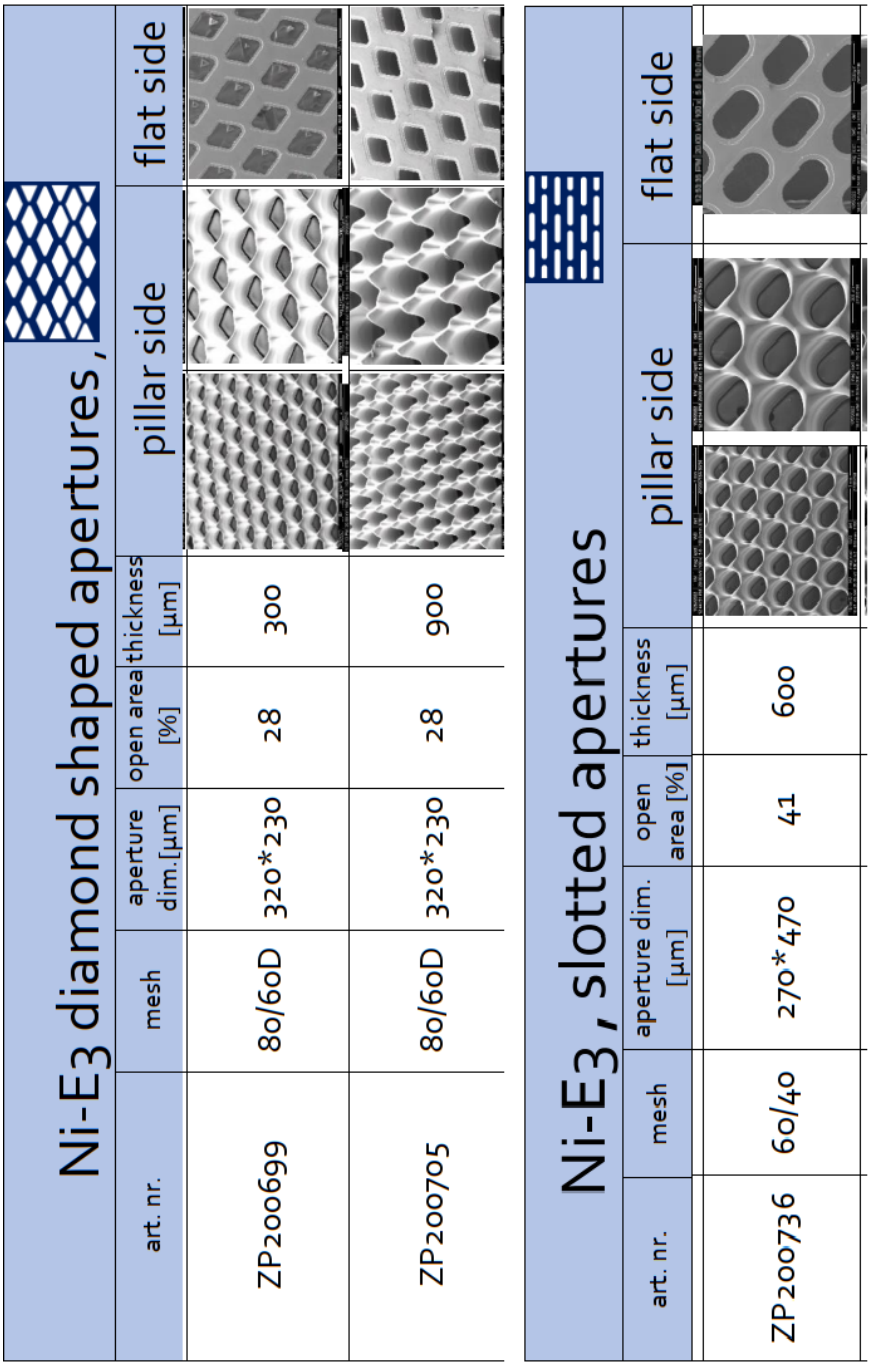

Figure B.1: Veco Samples properties

C
Vortex Analysis

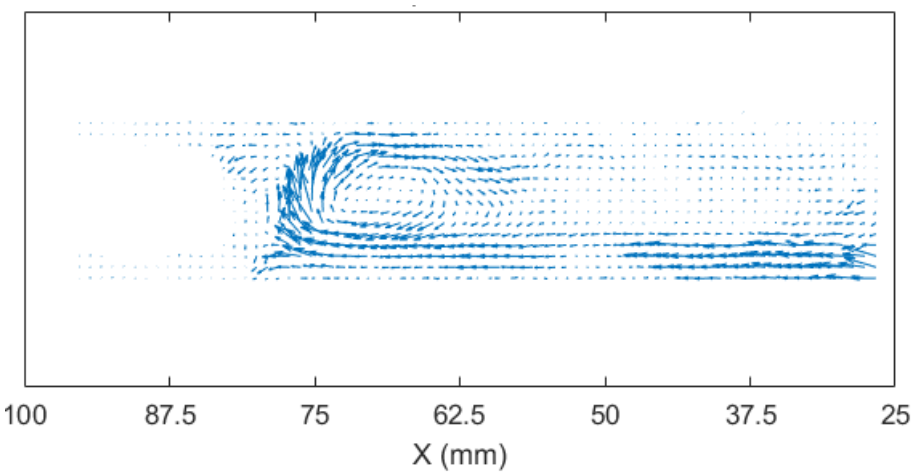

Figure C.1: Cathodic side. Average vector field 500 A/m^2. Captured at a frame rate of 1000 fps. Gap to wall = 1 cm. No subtraction Stokes velocity

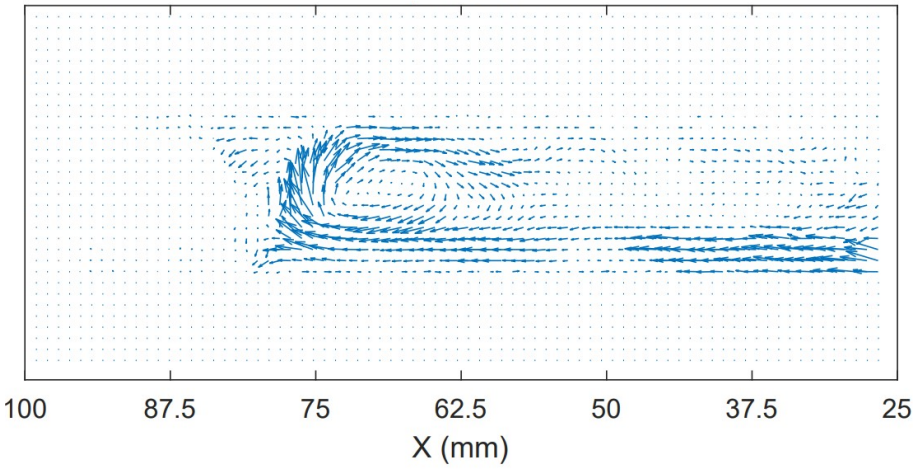

Figure C.2: Cathodic side. Average vector field 500 A/m^2. Captured at a frame rate of 1000 fps. Gap to wall = 1 cm. Stokes velocity subtracted.

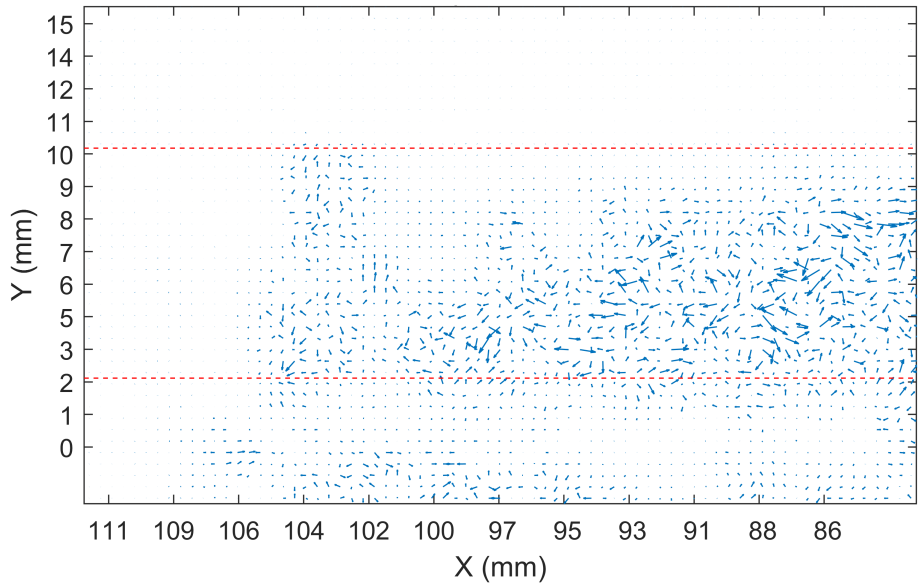

Figure C.3: Average vector field 400 A/m^2. Captured at a frame rate of 30 fps. The red lines denote the location of the wall (top) and the cathode (red). Velocities are also notable below the cathode as also a small portion of the anodic side is filmed. The electrolyte level was at 105 mm.

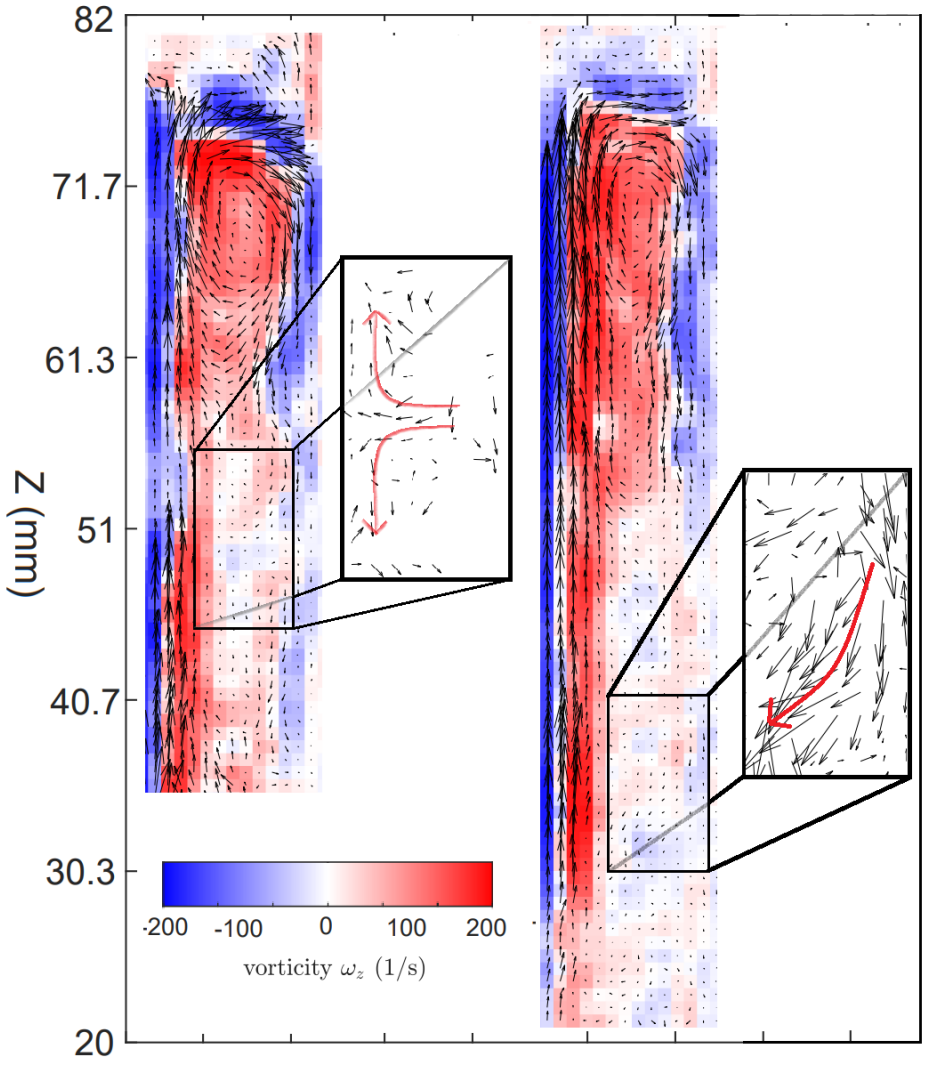

Figure C.6: Cathodic side. Left: 500 A/m^2. Right: 1100 A/m^2. Electrode-wall distance 1.0 cm. The electrolyte level at 7.5 cm. Zp200705 electrode. Lower area highlighted. Different movement patterns visible.

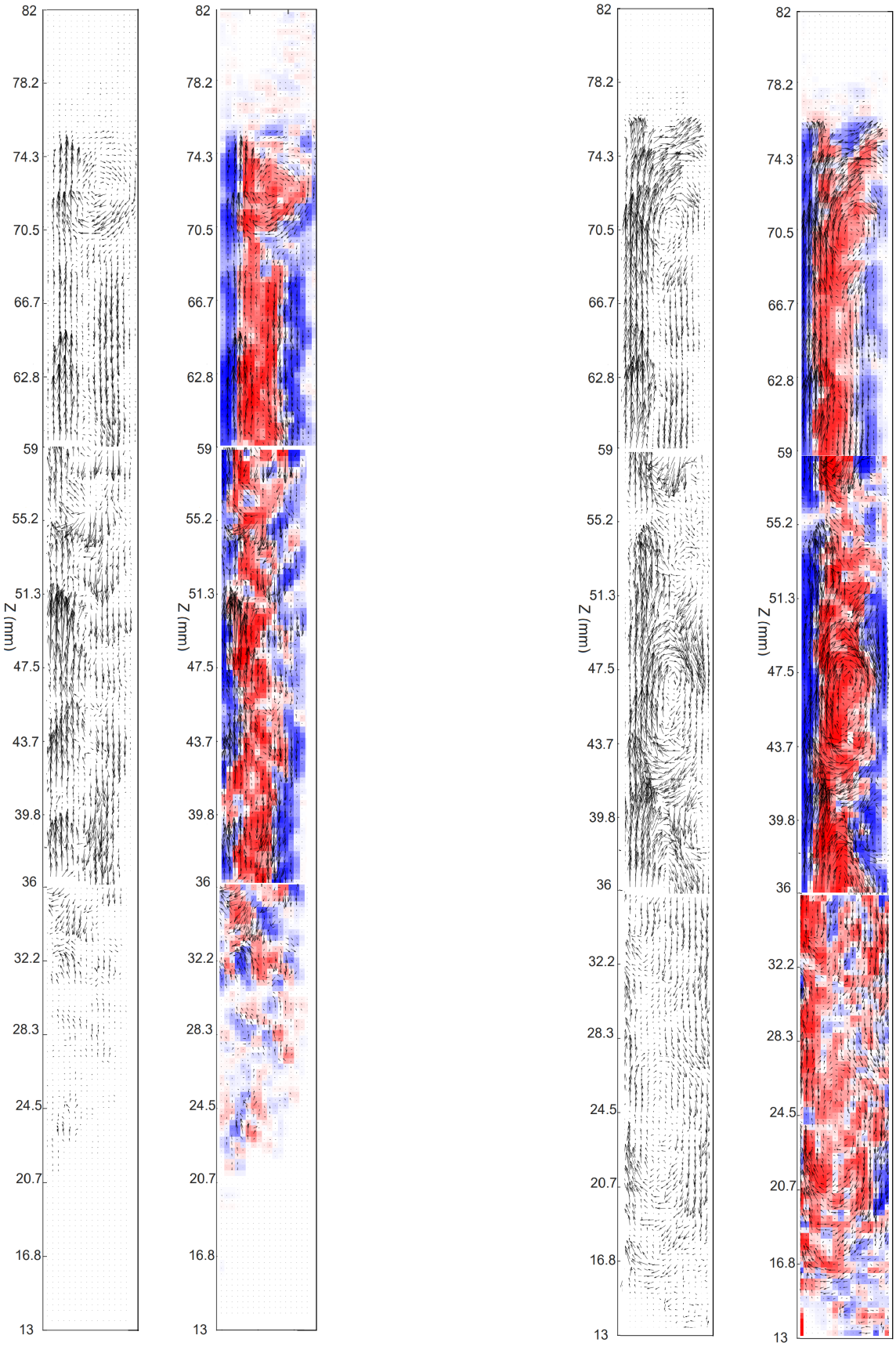

Figure C.4: Cathodic side. Left: 200 A/m^2. Right: 400 A/m^2. Electrode-wall distance 0.5 cm. The electrolyte level at 7.5 cm. Zp200705 electrode. Additionally, the results without color map are given.

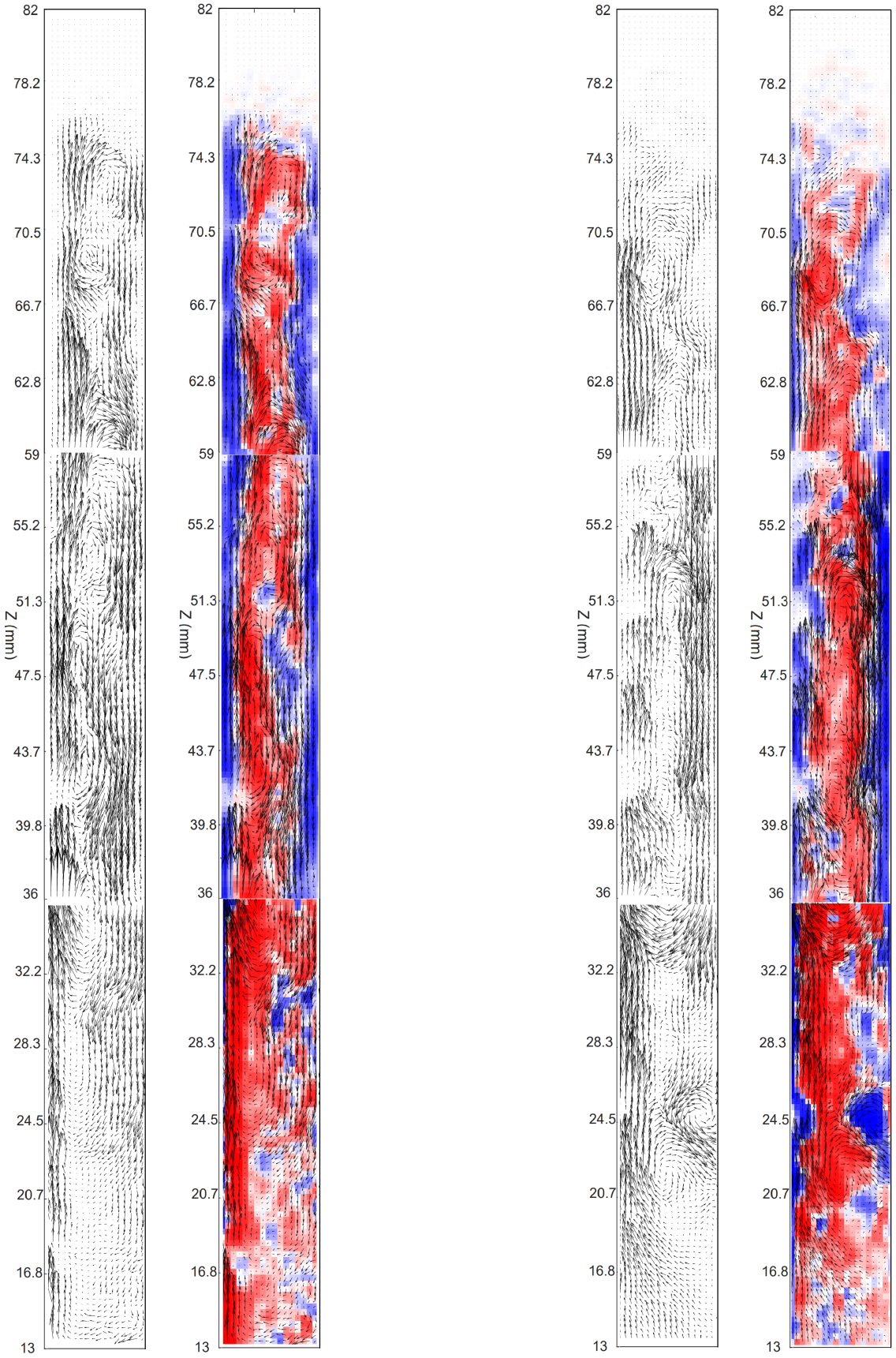

Figure C.5: Cathodic side. Left: 800 A/m^2. Right: 1600 A/m^2. Electrode-wall distance 0.5 cm. The electrolyte level at 7.5 cm. Zp200705 electrode. Additionally, the results without color map are given.

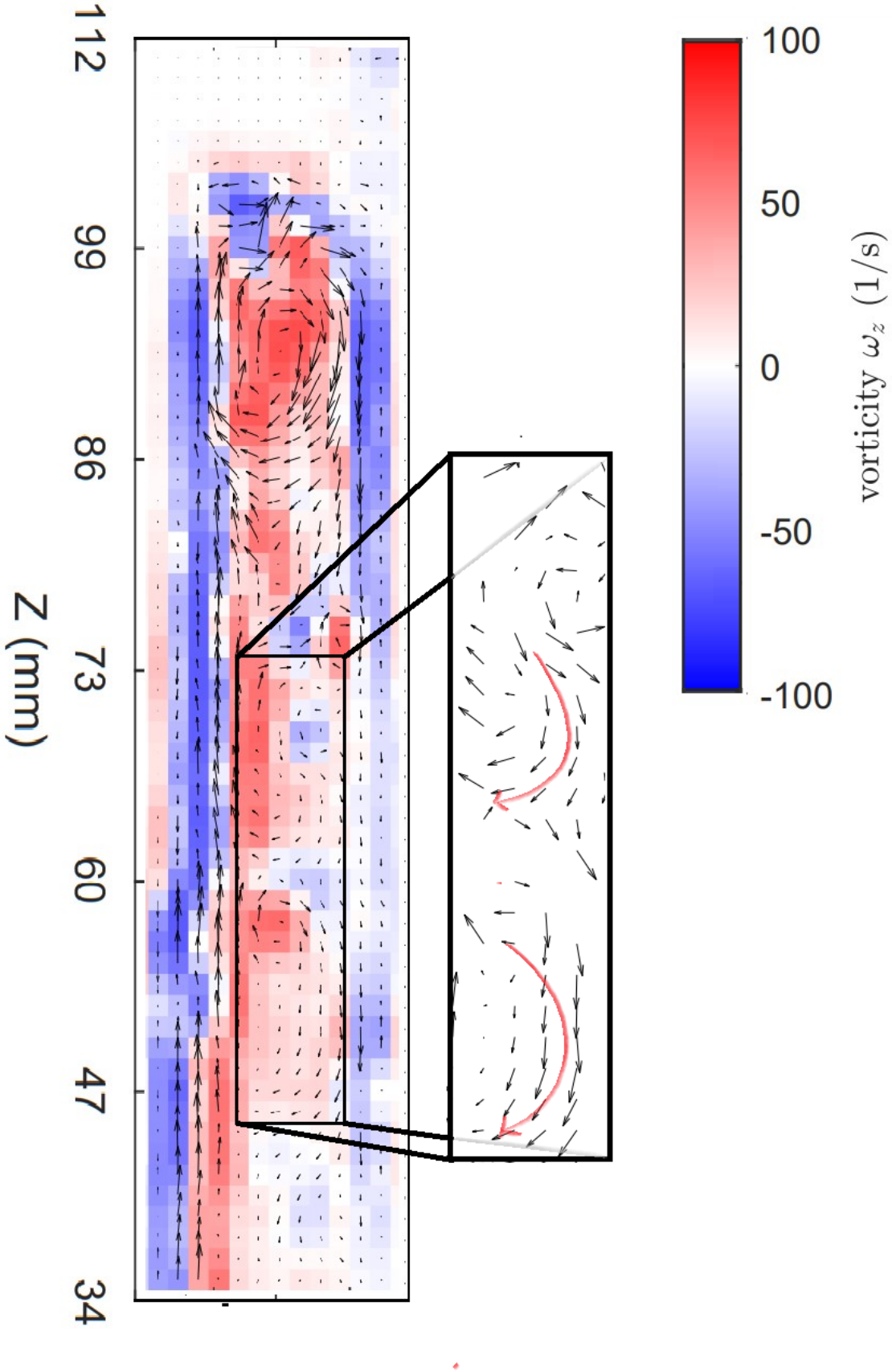

Figure C.7: Cathodic side. 800 A/m^2. No elastic element. Electrode-wall distance 1.5 cm. 60 seconds after applying current.

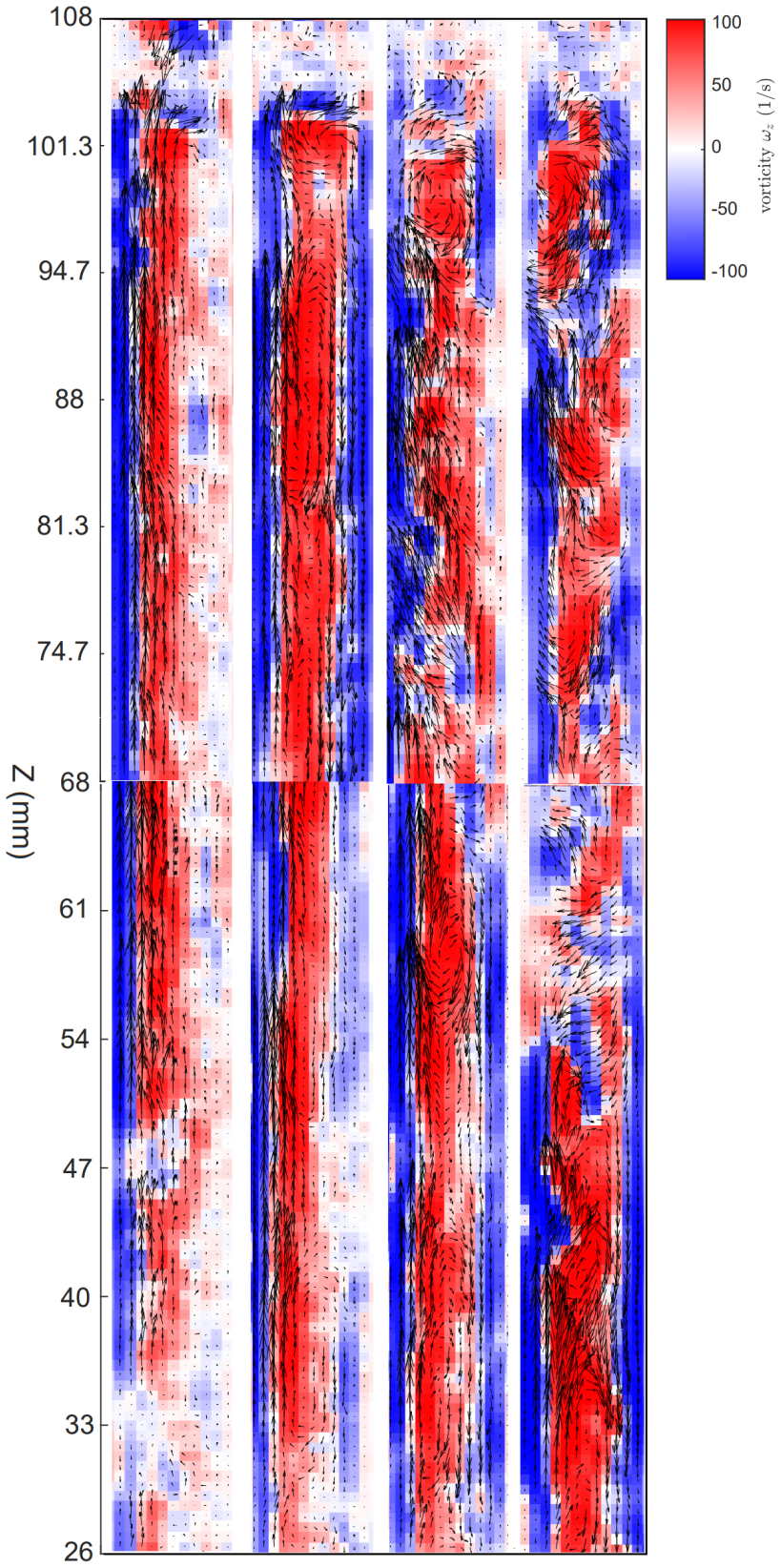

Figure C.8: Cathodic side. From left to right: 200, 400, 800, 1600 A/m^2. No elastic element. Electrode-wall distance 0.6 cm. 60 seconds after applying current.

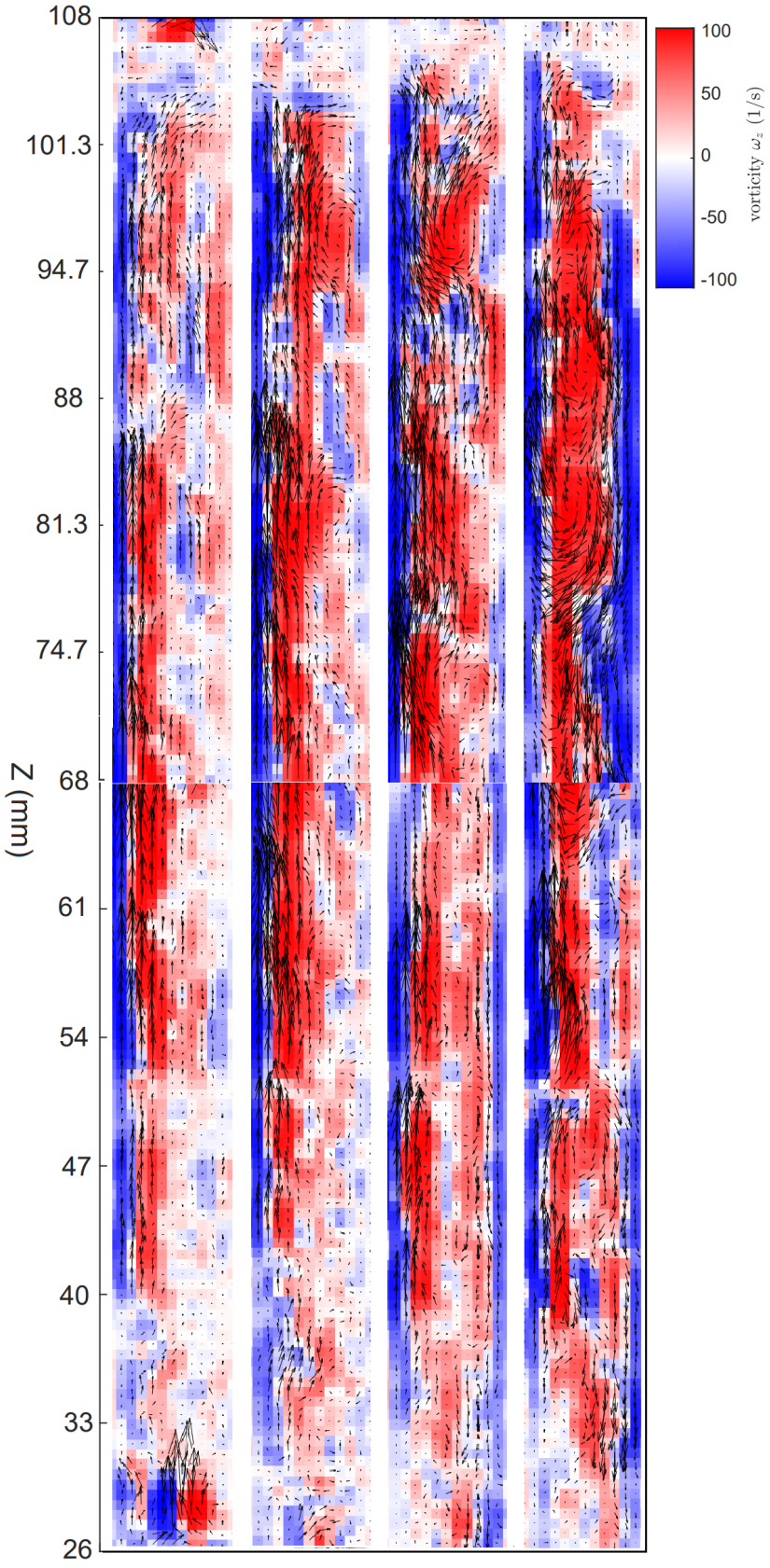

Figure C.9: Cathodic side. From left to right: 200, 400, 800, 1600 A/m^2. Elastic element. Electrode-wall distance 0.6 cm. 60 seconds after applying current.

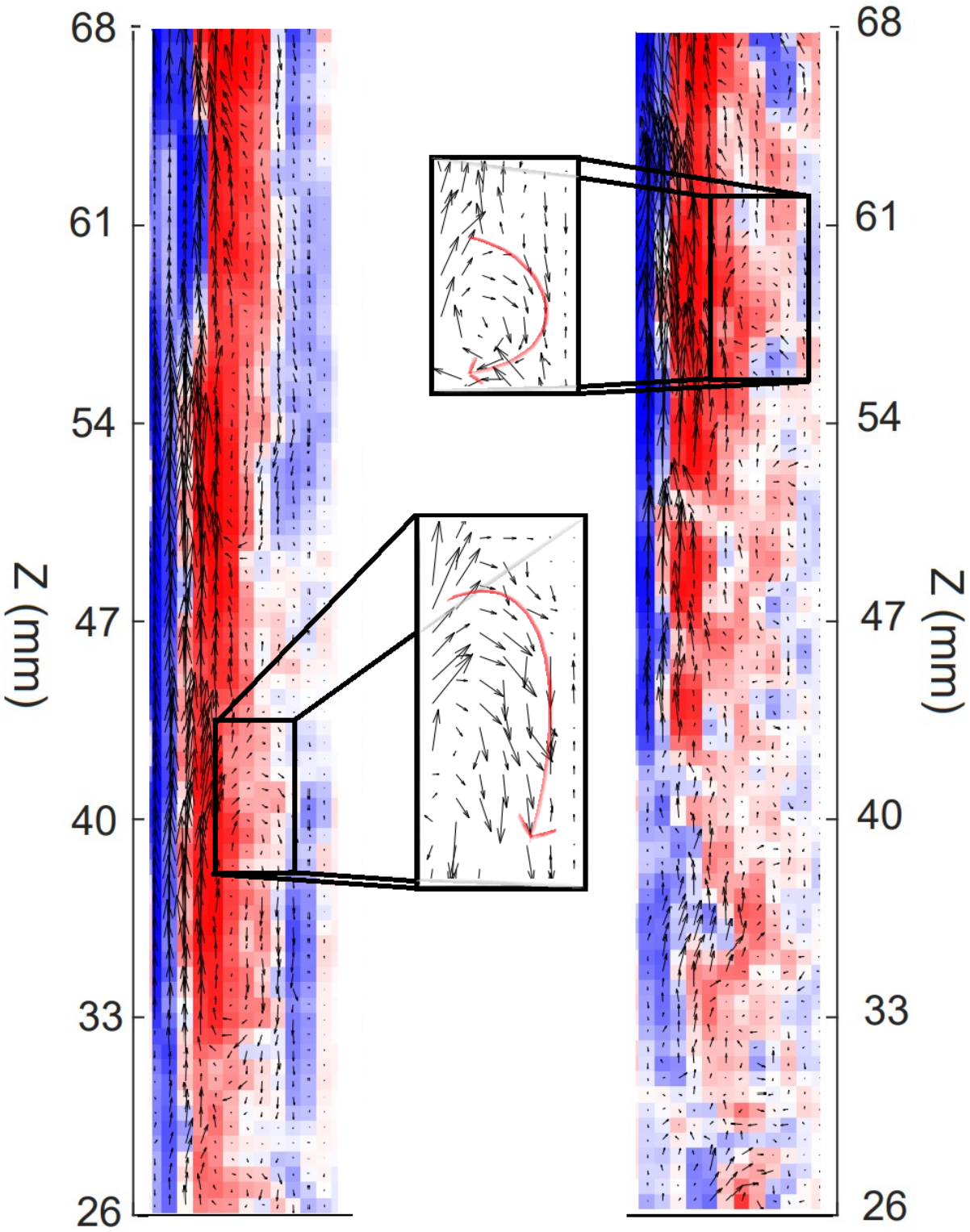

Figure C.10: Cathodic side. 400 A/m^2. Left: no elastic element. Right: elastic element. Electrode-wall distance 0.6 cm. 60 seconds after applying current.

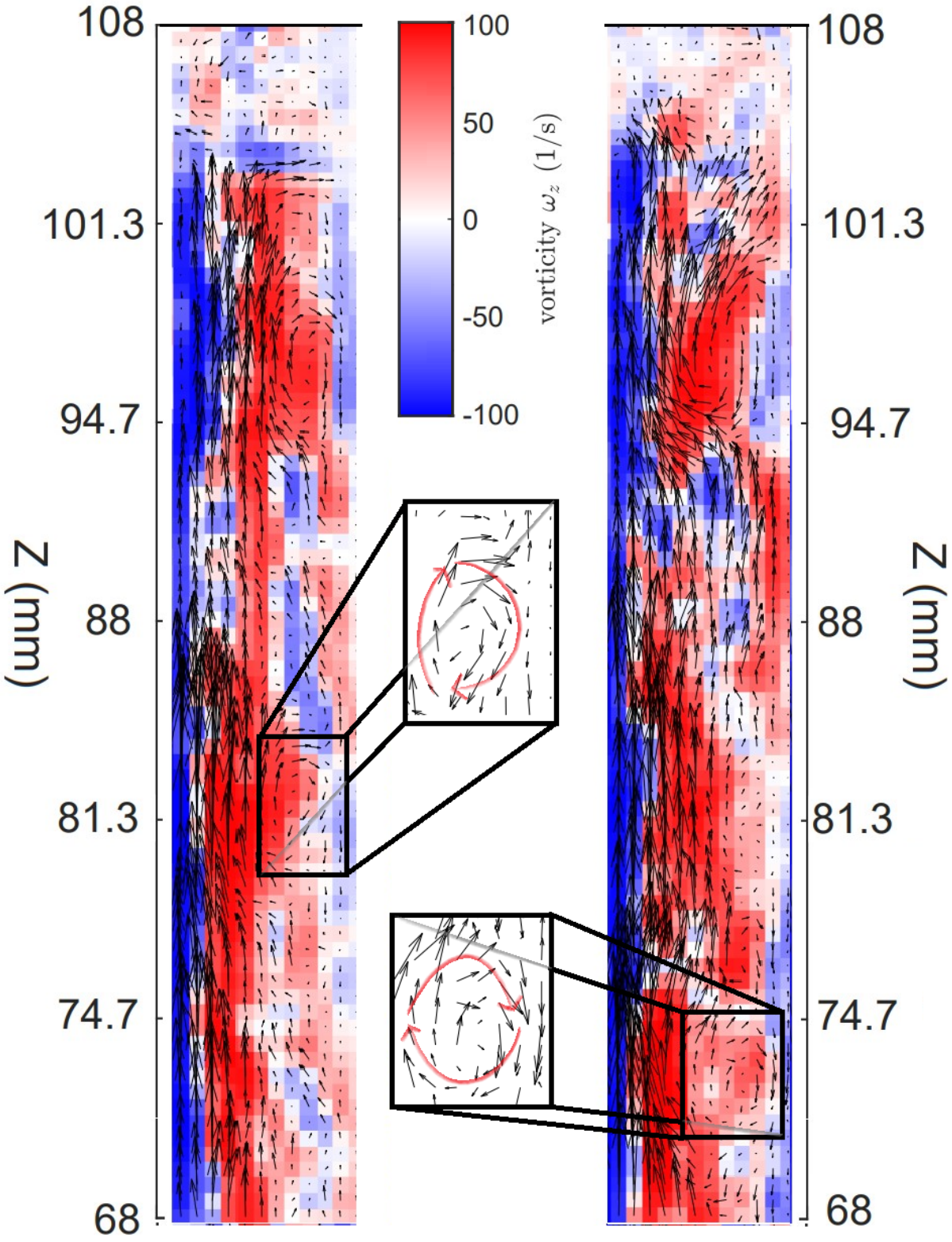

Figure C.11: Cathodic side. Elastic element. Left: 400 A/m^2. Right: 800 A/m^2. Electrode-wall distance 0.6 cm. 60 seconds after applying current.

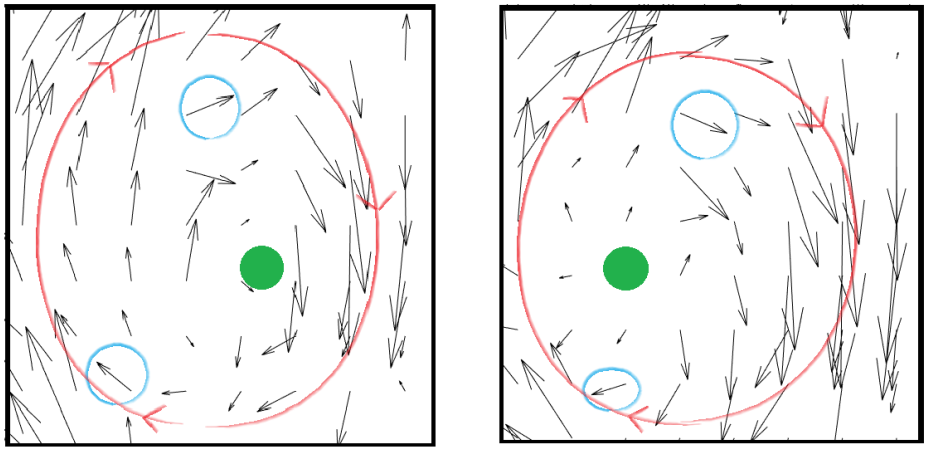

Figure C.12: Cathodic side. Elastic element. 800 A/m^2. Left: 50 microns diameter bubbles. Right: 100 microns diameter bubbles. Electrode-wall distance 0.6 cm. 60 seconds after applying current. Stokes velocity 4x higher for 100 microns. Clear effect on the vectors. Vortices still visible. Centre of vortices depicted in green.

D

Mist Height Analysis

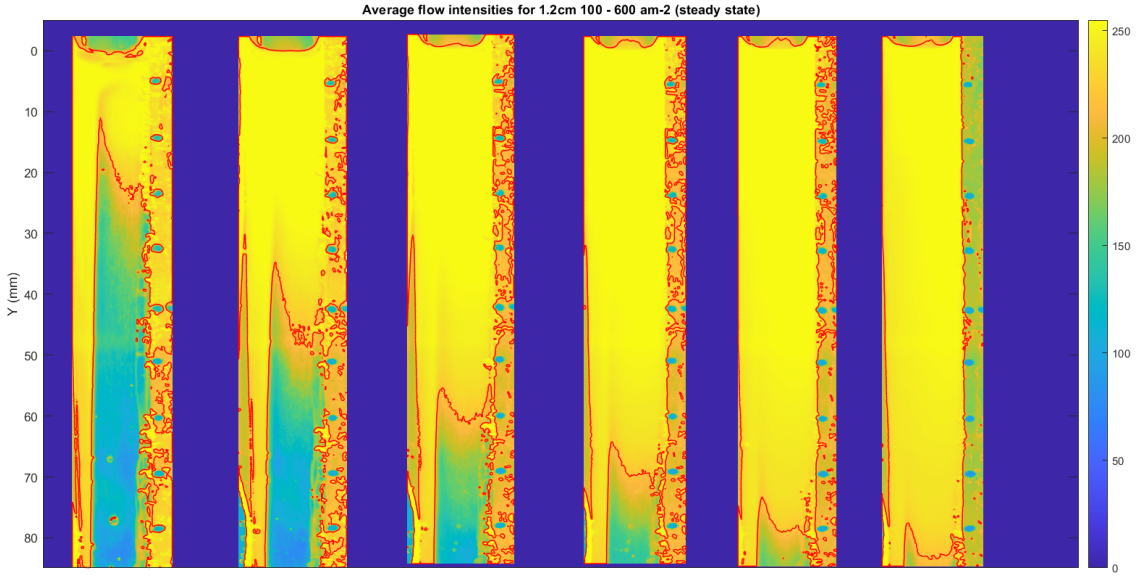

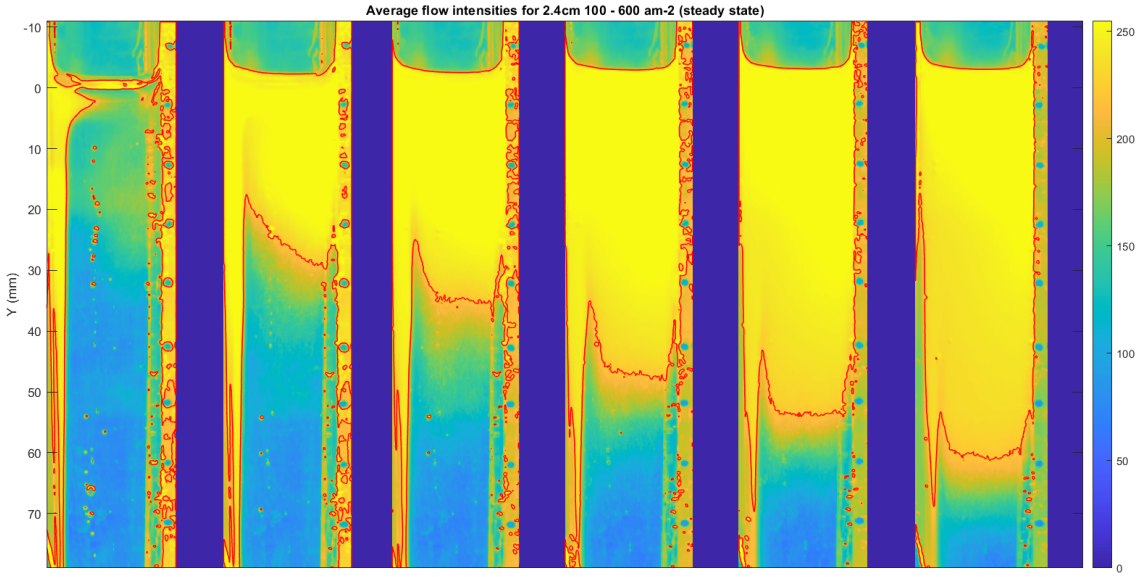

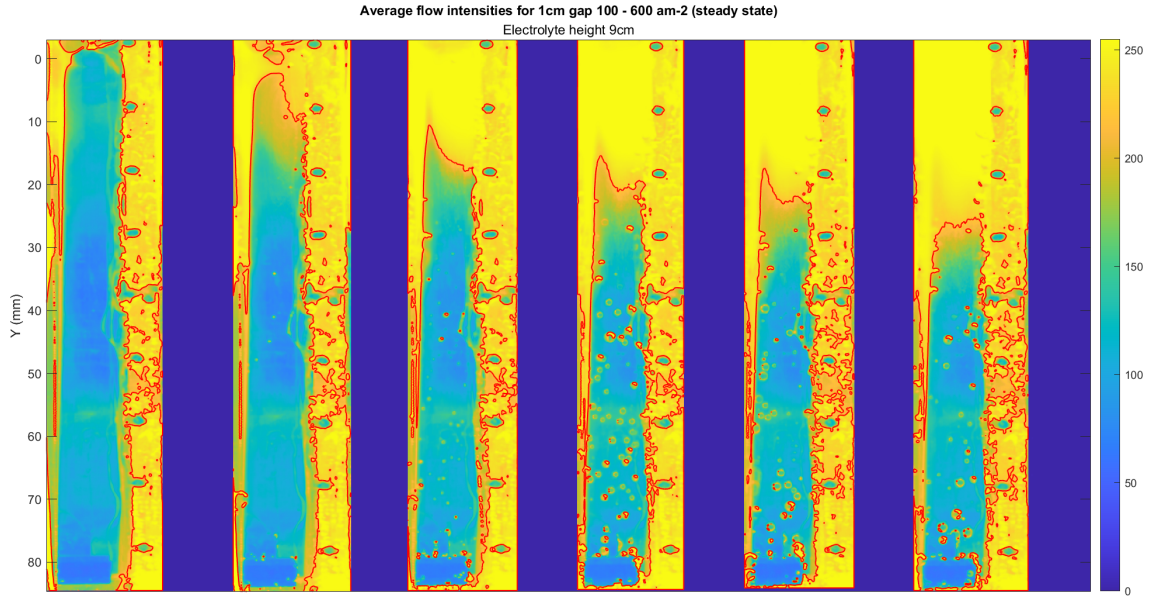
Average flow intensities for 1cm gap 100 - 600 am-2 (steady state)
Electrolyte height 9cm
Y (mm)
0
10
20
30
40
50
60
70
80
250
200
150
100
50
0

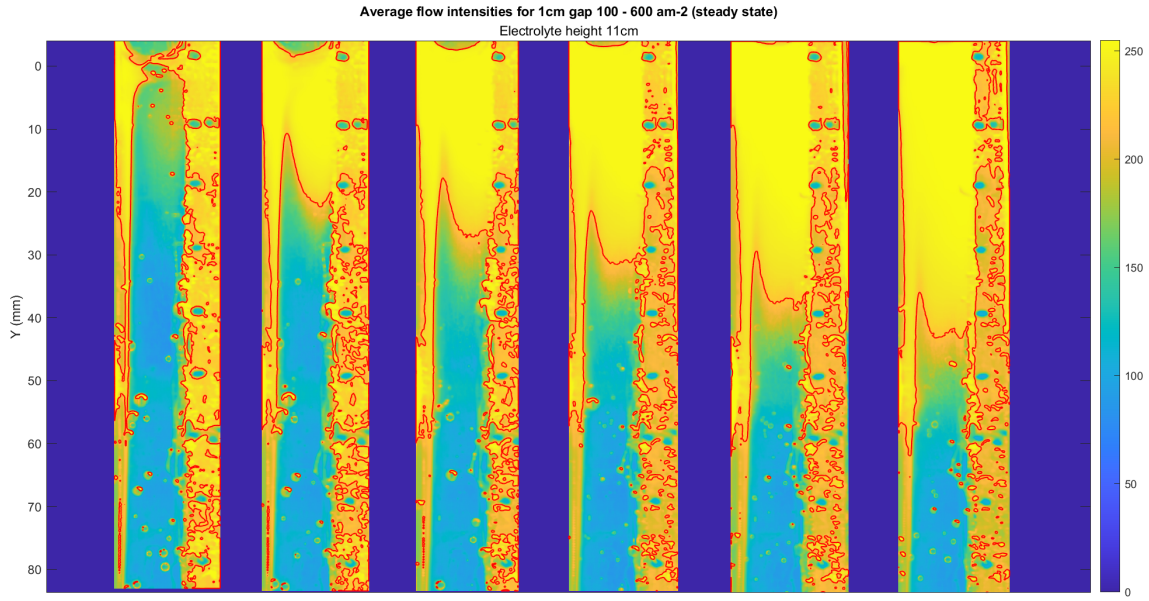
Average flow intensities for 1cm gap 100 - 600 am-2 (steady state)
Electrolyte height 11cm
Y (mm)
0
10
20
30
40
50
60
70
80
250
200
150
100
50
0

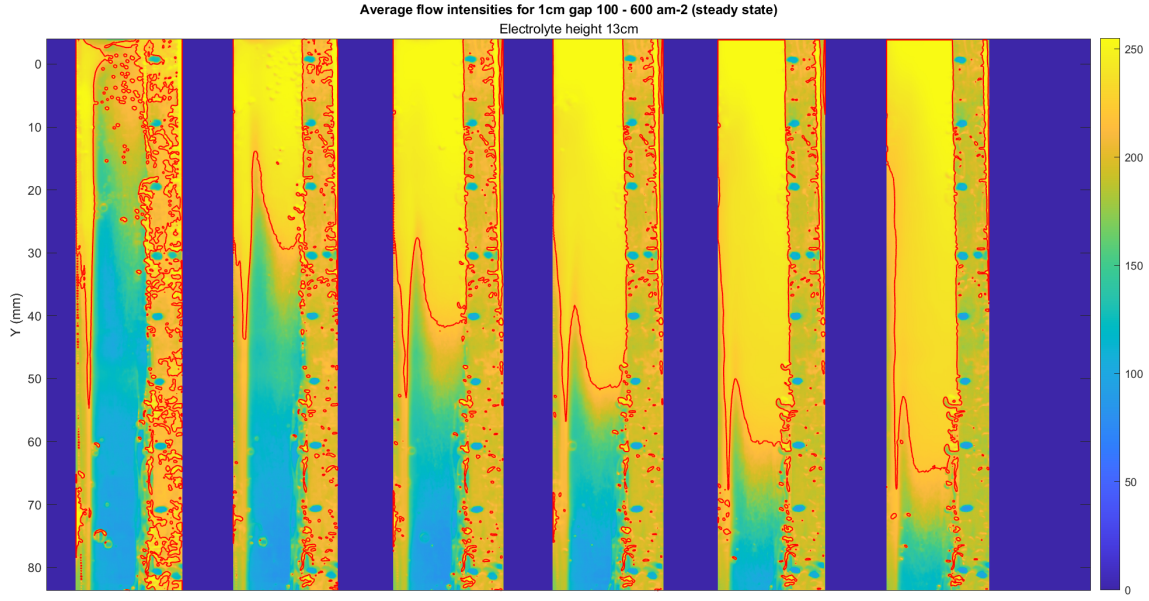
Average flow intensities for 1cm gap 100 - 600 am-2 (steady state)
Electrolyte height 13cm
Y (mm)
0
10
20
30
40
50
60
70
80
250
200
150
100
50
0

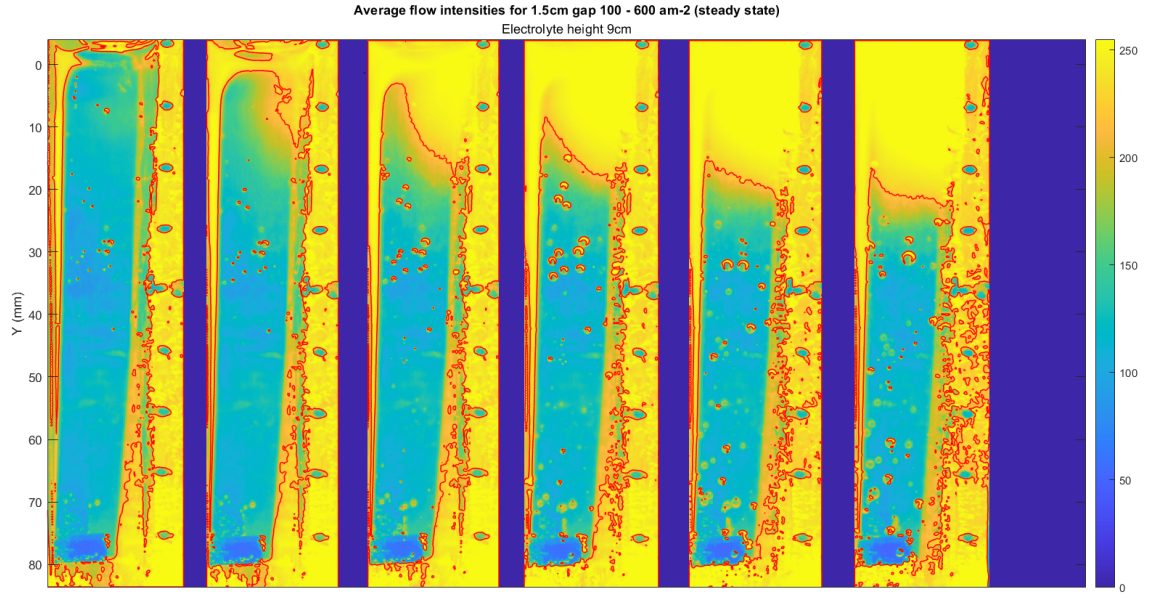
Average flow intensities for 1.5cm gap 100 - 600 am-2 (steady state)
Electrolyte height 9cm
Y (mm)
0
10
20
30
40
50
60
70
80
250
200
150
100
50
0

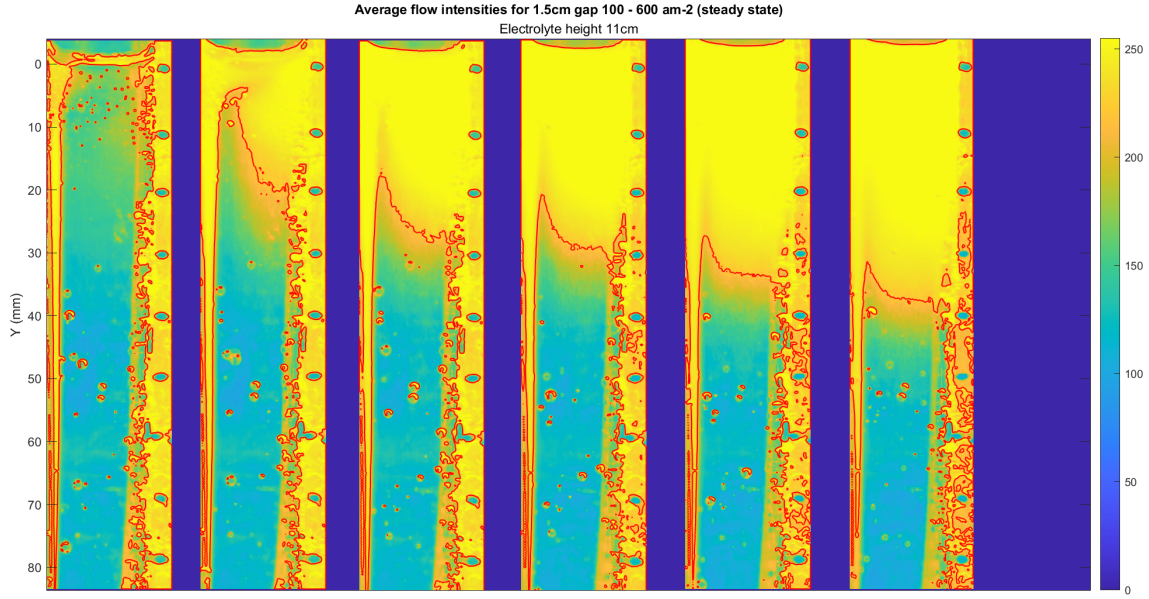
Average flow intensities for 1.5cm gap 100 - 600 am-2 (steady state)
Electrolyte height 11cm
Y (mm)
0
10
20
30
40
50
60
70
80
250
200
150
100
50
0

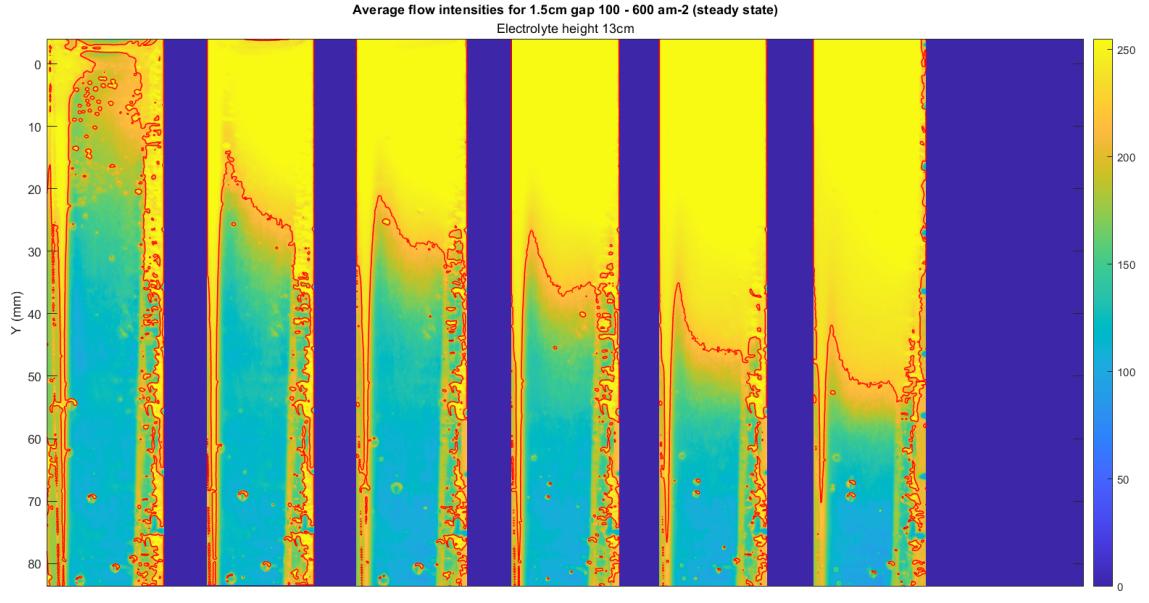
Average flow intensities for 1.5cm gap 100 - 600 am-2 (steady state)
Electrolyte height 13cm
Y (mm)
0
10
20
30
40
50
60
70
80
250
200
150
100
50
0

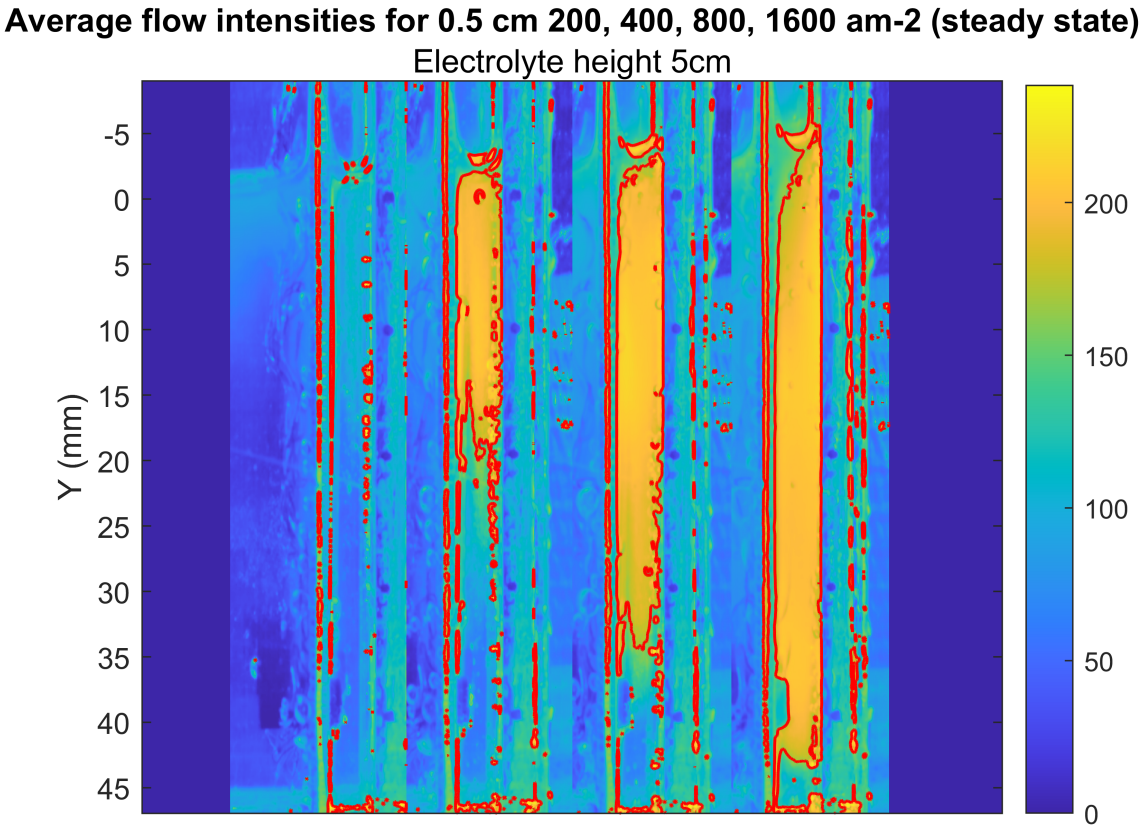
Average flow intensities for 0.5 cm 200, 400, 800, 1600 am-2 (steady state)
Electrolyte height 5cm
Y (mm)
-5
0
5
10
15
20
25
30
35
40
45
200
150
100
50
0

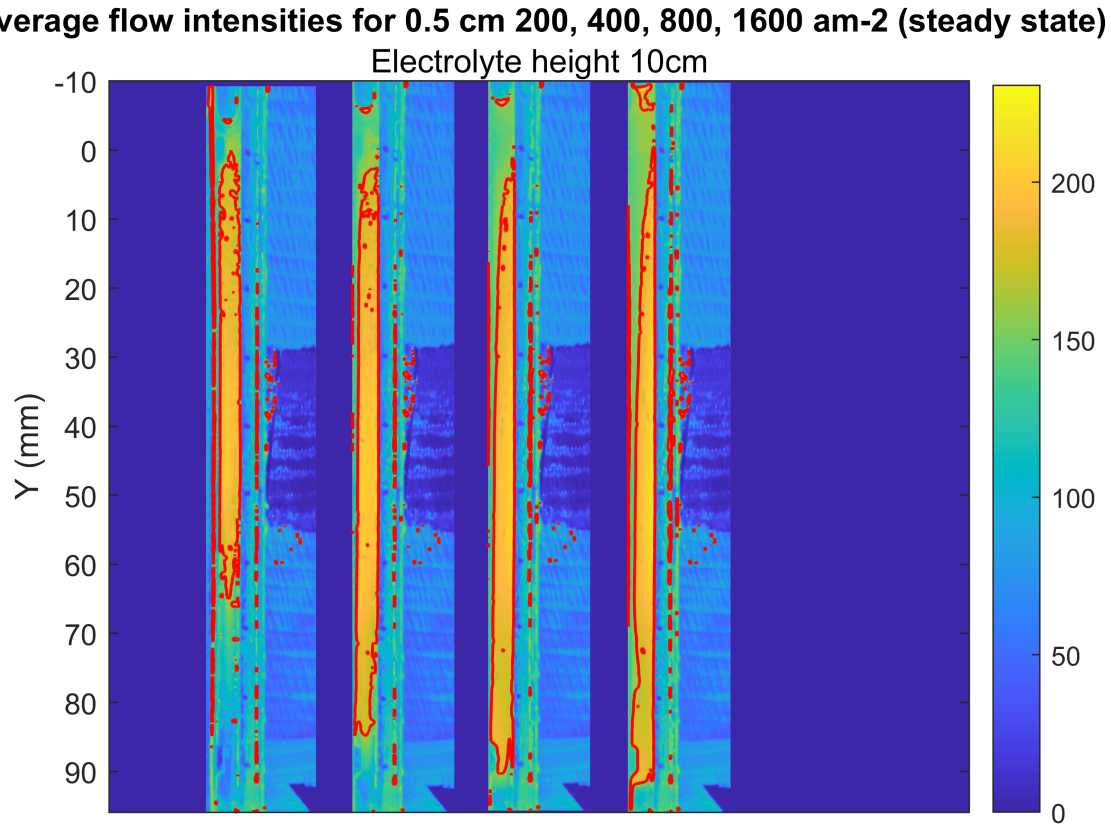
Average flow intensities for 0.5 cm 200, 400, 800, 1600 am-2 (steady state)
Electrolyte height 10cm
Y (mm)
-10
0
10
20
30
40
50
60
70
80
90
200
150
100
50
0

Average flow intensities for 0.5 cm 200, 400, 800, 1600 am-2 (steady state)

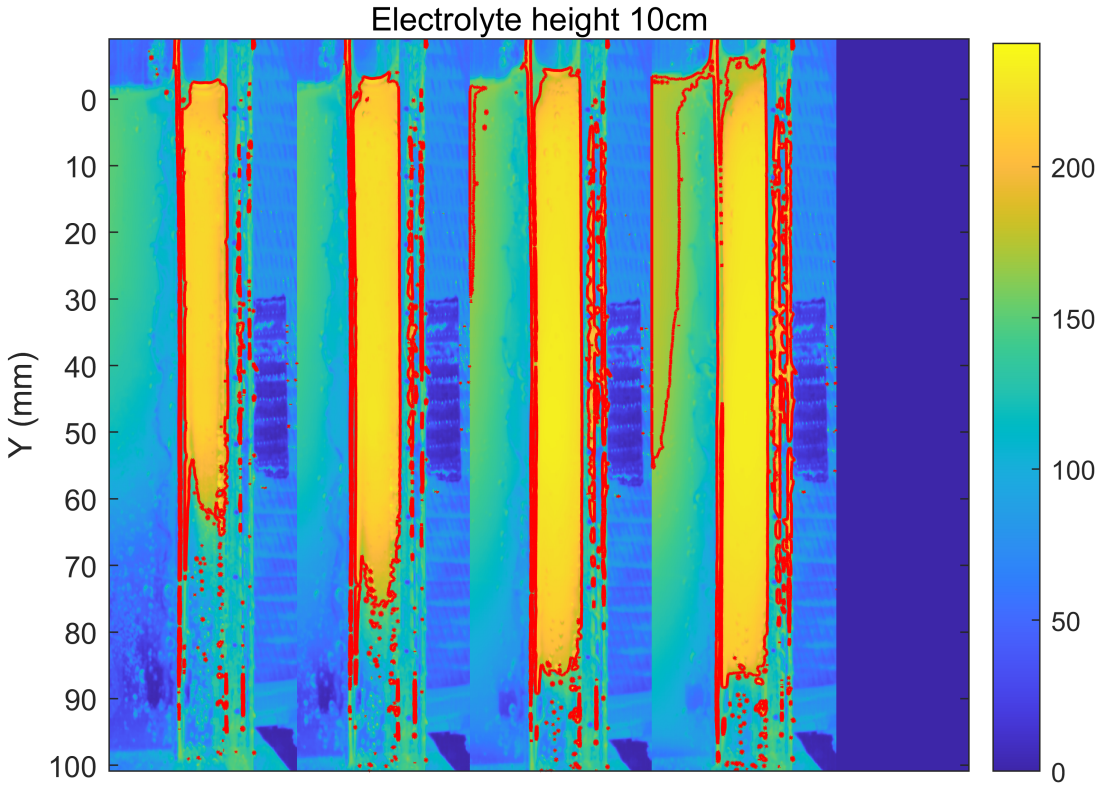

Average flow intensities for 0.5 cm 200, 400, 800, 1600 am-2 (steady state)

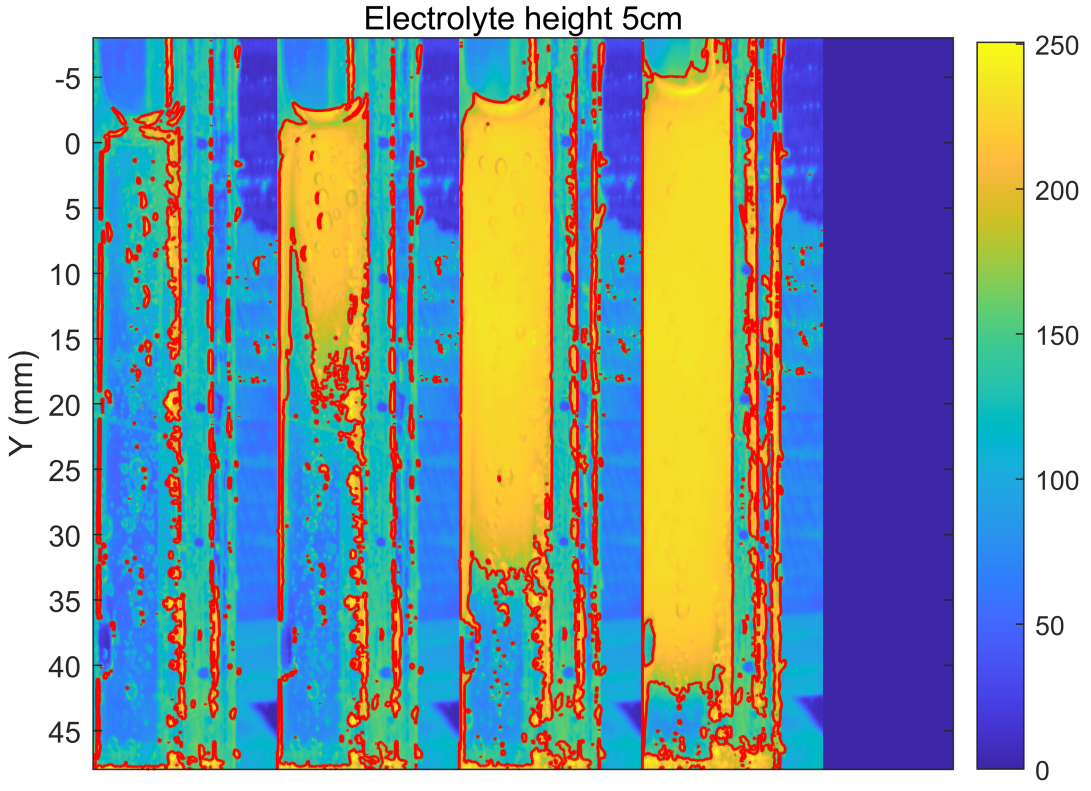

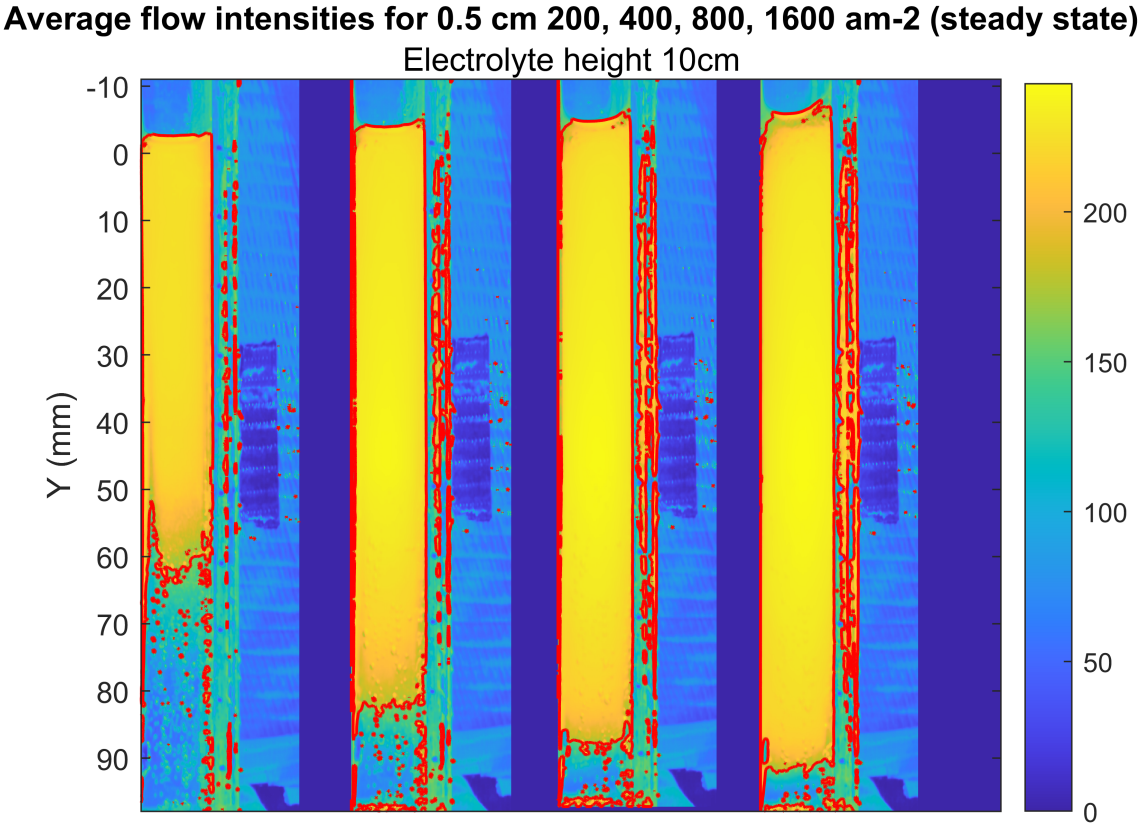
Average flow intensities for 0.5 cm 200, 400, 800, 1600 am-2 (steady state)
Electrolyte height 10cm
Y (mm)
-10
0
10
20
30
40
50
60
70
80
90
200
150
100
50
0

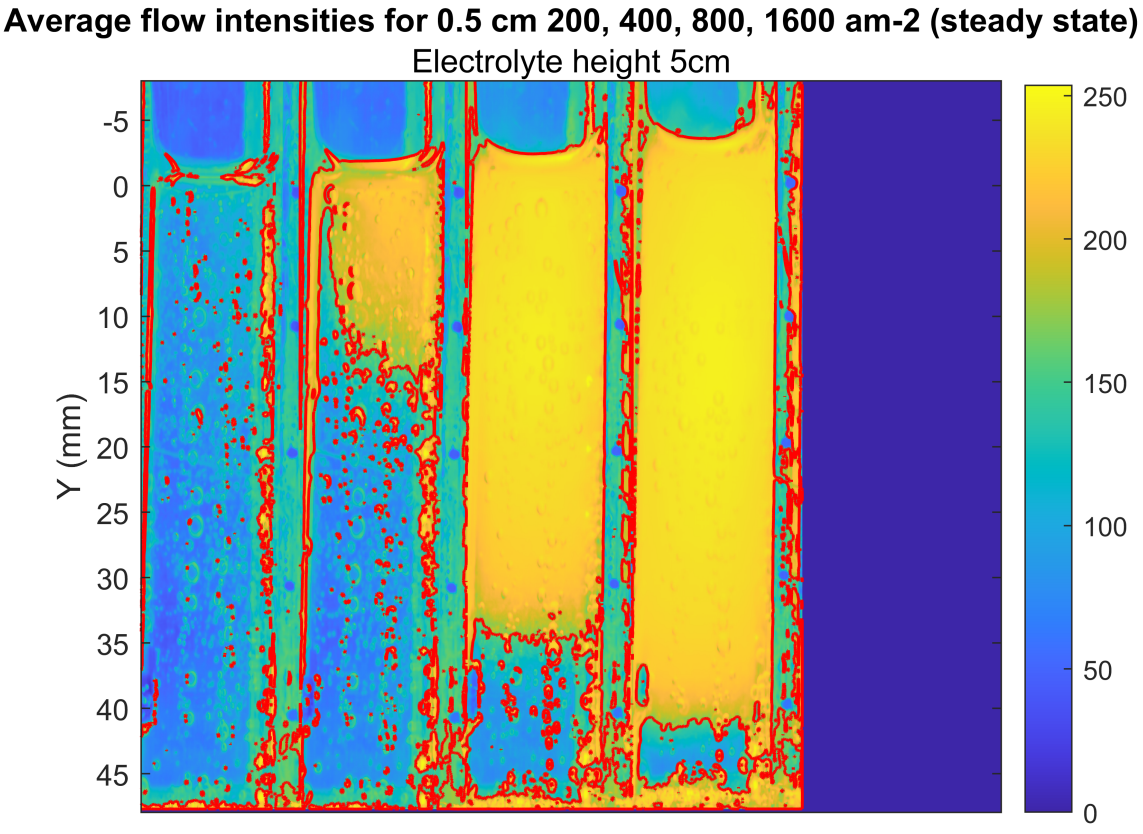
Average flow intensities for 0.5 cm 200, 400, 800, 1600 am-2 (steady state)
Electrolyte height 5cm
Y (mm)
-5
0
5
10
15
20
25
30
35
40
45
250
200
150
100
50
0

E

Bubble Plume Analysis

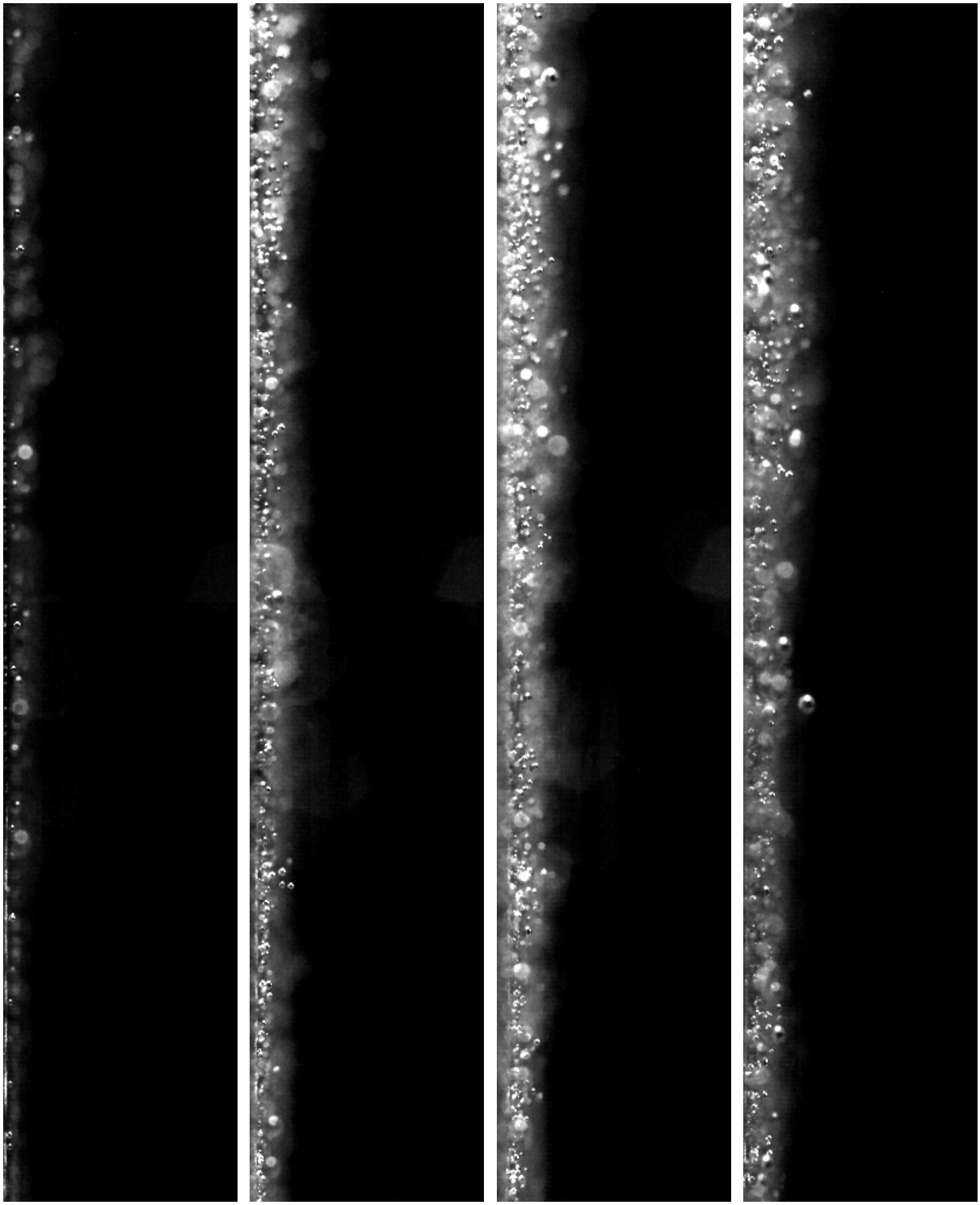

Figure E.1: Bubble plume 20, 70, 200, 550 A/m^2. Electrode height 2-5 cm.

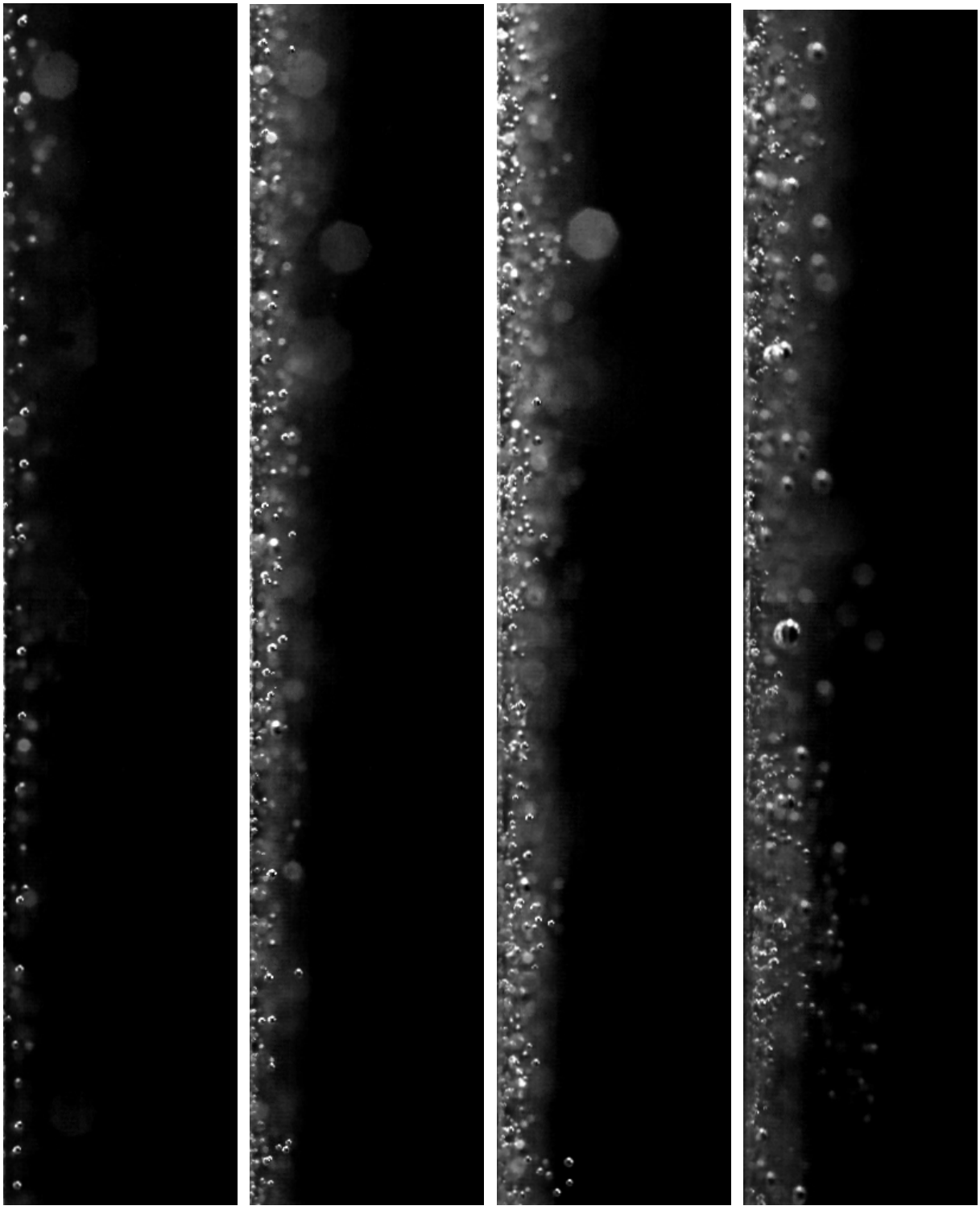

Figure E.2: Bubble plume 20, 70, 200, 550 A/m^2. Electrode height 5-8 cm.

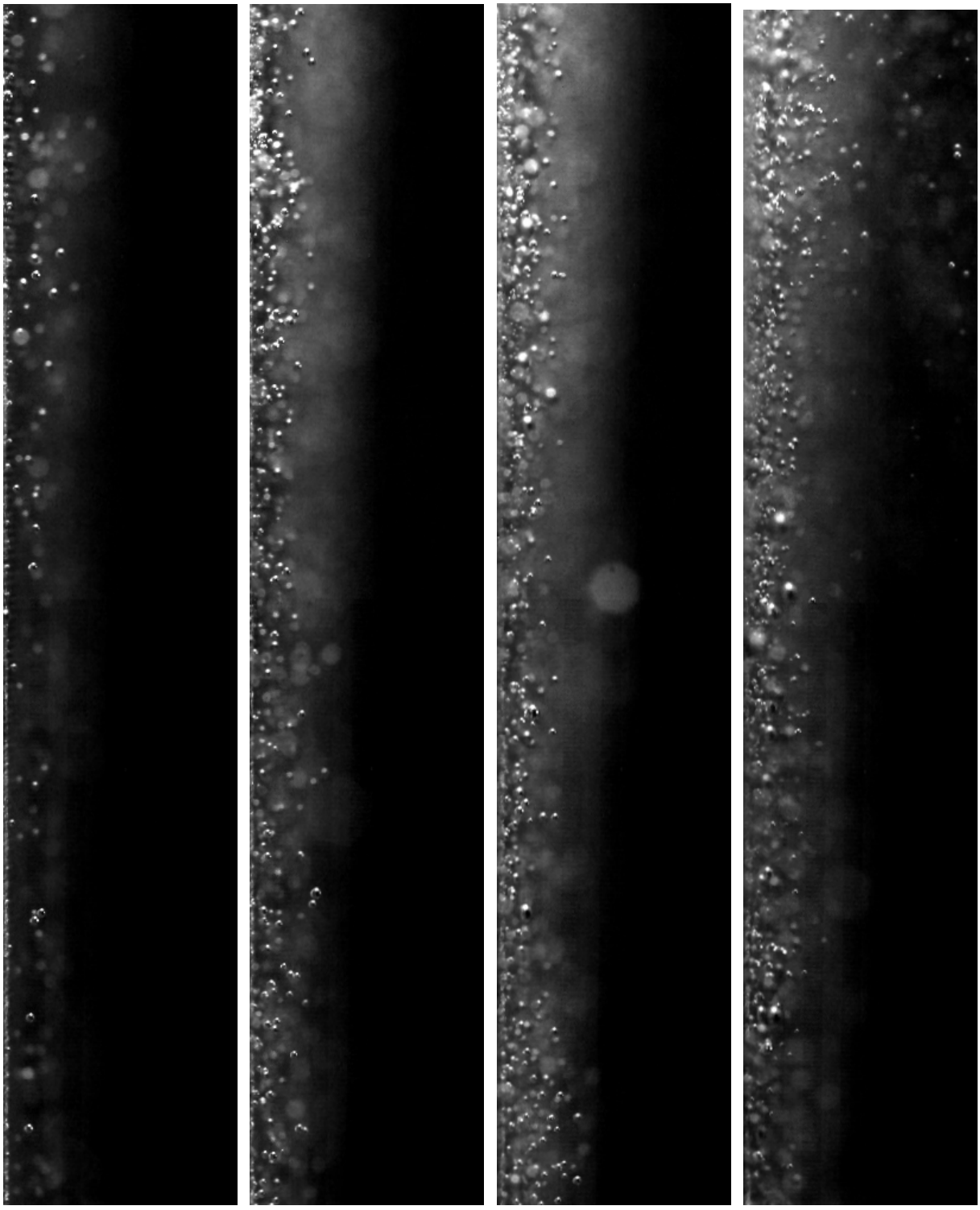

Figure E.3: Bubble plume 20, 70, 200, 550 A/m^2. Electrode height 8-11 cm.

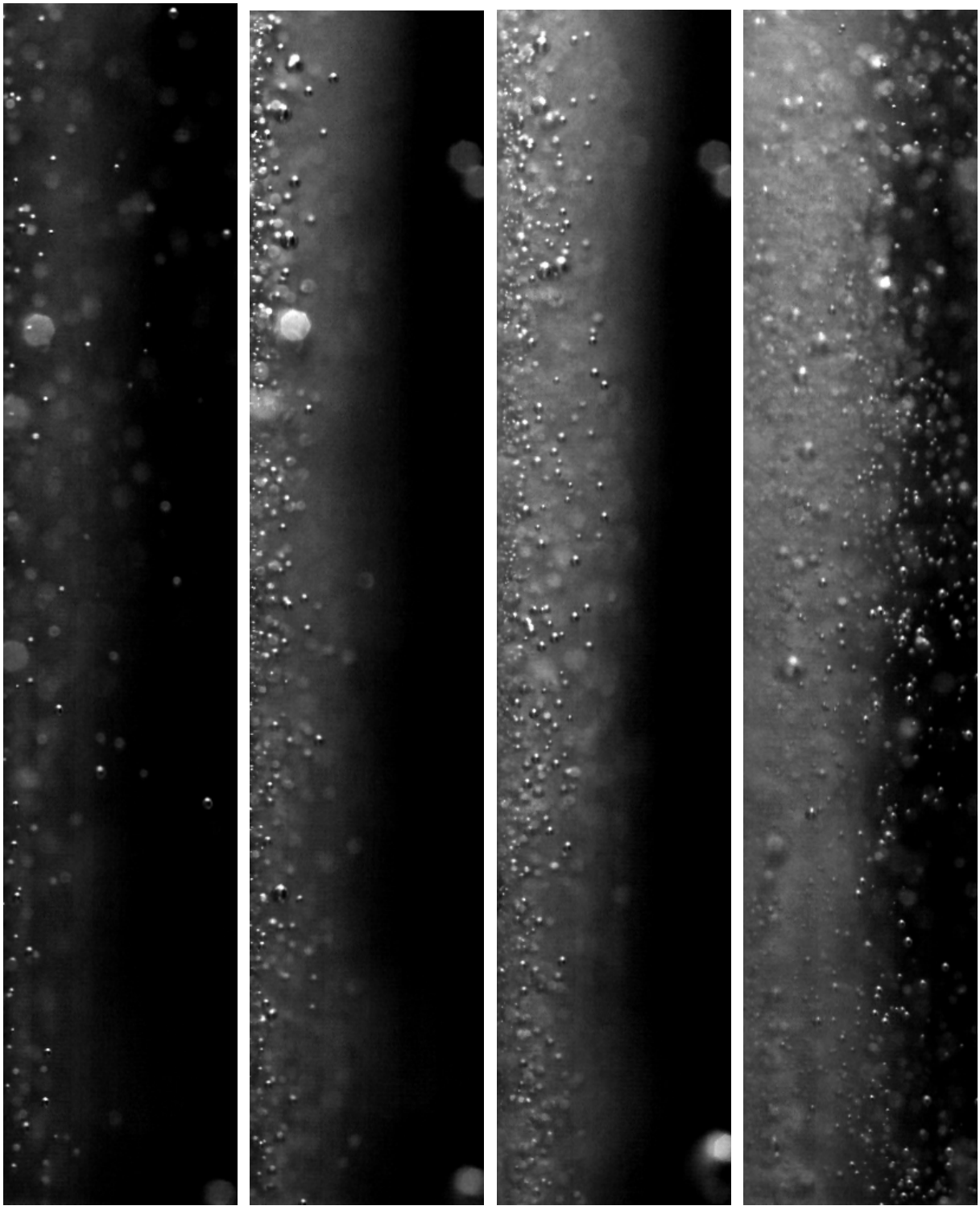

Figure E.4: Bubble plume 20, 70, 200, 550 A/m^2. Electrode height 11-14 cm.

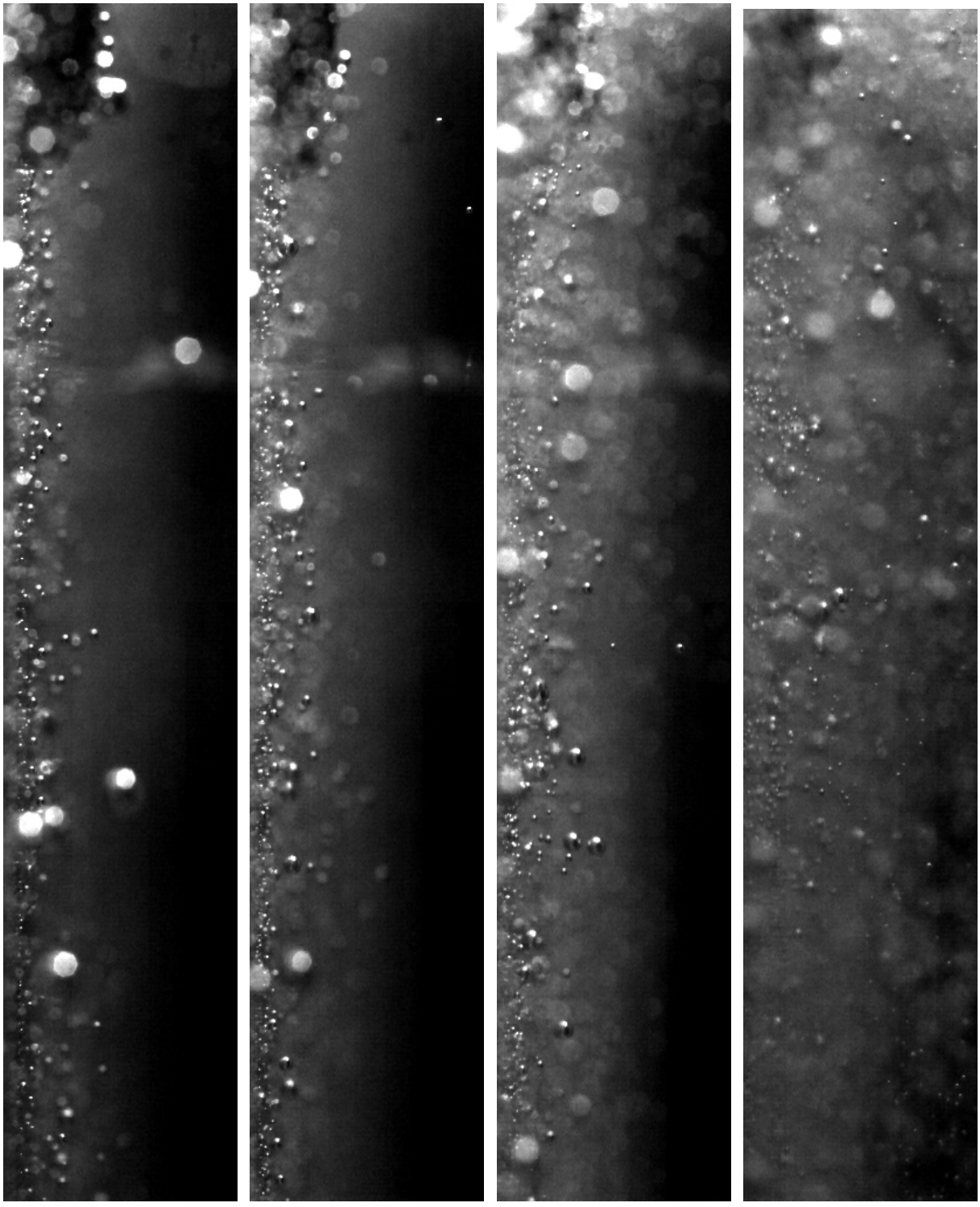

Figure E.5: Bubble plume 20, 70, 200, 550 A/m^2. Electrode height 14-17 cm. At the top, one of the bolts connecting the cathode to the membrane and anode is visible.

Bibliography

[1] European Bank for Reconstruction and Development (EBRD), "What is the Paris Agreement." https://www.ebrd.com/paris-agreement, Accessed on: 02-02-2023.

[2] A. Godula-Jopek, *Hydrogen Productionby Electrolysis*. John Wiley & Sons, Ltd, 2015.

[3] S. S. Kumar and V. Himabindu, "Hydrogen production by pem water electrolysis–a review," *Materials Science for Energy Technologies*, vol. 2, no. 3, pp. 442–454, 2019.

[4] Qyyum, M.A., et al., "Availability, versatility, and viability of feedstocks for hydrogen production: Product space perspective," *Renewable and Sustainable Energy Reviews*, vol. 145, 2021.

[5] M. Rashid, M. K. Al Mesfer, H. Naseem, and M. Danish, "Hydrogen production by water electrolysis: a review of alkaline water electrolysis, pem water electrolysis and high temperature water electrolysis," *International Journal of Engineering and Advanced Technology*, 2015.

[6] F. Allebrod, C. Chatzichristodoulou, P. L. Mollerup, and M. B. Mogensen, "Electrical conductivity measurements of aqueous and immobilized potassium hydroxide," *International Journal of Hydrogen Energy*, vol. 37, no. 21, pp. 16505–16514, 2012.

[7] R. Gilliam, J. Graydon, D. Kirk, and S. Thorpe, "A review of specific conductivities of potassium hydroxide solutions for various concentrations and temperatures," *International Journal of Hydrogen Energy*, vol. 32, no. 3, pp. 359–364, 2007.

[8] S. Coutanceau, C. Baranton and T. Audichon, *Hydrogen Electrochemical Production*. Elsevier Ltd, 2018.

[9] A. B. T. Nelabhotla, D. Pant, and C. Dinamarca, "Chapter 8 - power-to-gas for methanation," in *Emerging Technologies and Biological Systems for Biogas Upgrading* (N. Aryal, L. D. M. Ottosen, M. V. W. Kofoed, and D. Pant, eds.), pp. 187–221, Academic Press, 2021.

[10] Marini. S, et al., "Advanced alkaline water electrolysis," *Electrochimica Acta*, vol. 82, 2012.

[11] S. Ye, C. Ding, and C. Li, "Artificial photosynthesis systems for catalytic water oxidation," in *Advances in Inorganic Chemistry*, vol. 74, pp. 3–59, Elsevier, 2019.

[12] T. Shinagawa, A. T. Garcia-Esparza, and K. Takanabe, "Insight on tafel slopes from a microkinetic analysis of aqueous electrocatalysis for energy conversion," *Scientific reports*, vol. 5, no. 1, p. 13801, 2015.

[13] I. Abe, "Alkaline water electrolysis," *Energy carriers and conversion systems*, vol. 1, 2009.

[14] Fokko Mulder, Hans Geerlings, "Lecture notes in hydrogen technology," 4 2021.

[15] J. Huot, M. Trudeau, and R. Schulz, "Low hydrogen overpotential nanocrystalline ni-mo cathodes for alkaline water electrolysis," *Journal of The Electrochemical Society*, vol. 138, no. 5, p. 1316, 1991.

[16] R. Phillips and C. W. Dunnill, "Zero gap alkaline electrolysis cell design for renewable energy storage as hydrogen gas," *RSC advances*, vol. 6, no. 102, pp. 100643–100651, 2016.

[17] S. A. Grigoriev, V. N. Fateev, and P. Millet, "Alkaline electrolysers," in *Comprehensive Renewable Energy* (T. M. Letcher, ed.), pp. 459–472, Elsevier, second edition ed., 2022.

[18] De Nora, "De nora electrodic package for alkaline water electrolysis." https://www.denora.com, 2018. Accessed: 2023-08-01.

[19] J. E. Julia, Y. Liu, T. Hibiki, and M. Ishii, "Local flow regime analysis in vertical co-current downward two-phase flow," *Experimental thermal and fluid science*, vol. 44, pp. 345–355, 2013.

[20] R. Wetind, *Two-phase flows in gas-evolving electrochemical applications*. PhD thesis, Mekanik, 2001.

[21] M. Lokanathan and T. Hibiki, "Flow regime, void fraction and interfacial area transport and characteristics of co-current downward two-phase flow," *Nuclear Engineering and Design*, vol. 307, pp. 39–63, 2016.

[22] J. Luo, P. Jiao, N. Duan, F. Xu, and L. Jiang, "Flow field characterization in the vicinity of vertical plane electrodes in a bench-scale zinc electrowinning cell," *Hydrometallurgy*, vol. 181, pp. 103–112, 2018.

[23] Shah, A. and Jorne, J., "Mass Transfer under Bubble-Induced Convection in a Vertical Electrochemical Cell," *Journal of The Electrochemical Society*, vol. 136, pp. 144–153, 1989.

[24] P. Chandran, S. Bakshi, and D. Chatterjee, "Study on the characteristics of hydrogen bubble formation and its transport during electrolysis of water," *Chemical Engineering Science*, vol. 138, pp. 99–109, 2015.

[25] Baczyzmalski, D. et al, "Near-wall measurements of the bubble- and lorentz-force-driven convection at gas-evolving electrodes," *Exp. Fluids*, vol. 56, no. 162, 2015.

[26] C.-C. Wang, C.-Y. Chen, *et al.*, "Water electrolysis in the presence of an ultrasonic field," *Electrochimica Acta*, vol. 54, no. 15, pp. 3877–3883, 2009.

[27] K. Mazloomi, N. B. Sulaiman, and H. Moayedi, "Electrical efficiency of electrolytic hydrogen production," *International Journal of Electrochemical Science*, vol. 7, no. 4, pp. 3314–3326, 2012.

[28] D. M. Santos, C. A. Sequeira, and J. L. Figueiredo, "Hydrogen production by alkaline water electrolysis," *Química Nova*, vol. 36, pp. 1176–1193, 2013.

[29] N. Mazloomi, K. Sulaiman, "Hydrogen production by alkaline water electrolysis," *International Journal of Applied Electronics in Physics & Robotics*, vol. 1, pp. 1–4, 2013.

[30] M. Fouad and G. Sedahmed, "Effect of gas evolution on the rate of mass transfer at vertical electrodes," *Electrochimica Acta*, vol. 17, no. 4, pp. 665–672, 1972.

[31] M. Renardy and Y. Renardy, "Stability and instability in viscous fluids," *Handbook of Mathematical Fluid Dynamics*, vol. 2, pp. 223–287, 2003.

[32] Smith, R. et al, *Chapter 8 - Heat Transfer and Finite-Difference Methods*. Supercritical Fluid Science and Technology, 2013.

[33] Y.-J. Guo, H.-B. Xu, G. Fen, S.-L. Zheng, and Y. Zhang, "Density and viscosity of aqueous solution of k2cro4/koh mixed electrolytes," *Transactions of Nonferrous Metals Society of China*, vol. 20, pp. s32–s36, 2010.

[34] P. Boissonneau and P. Byrne, "Experimental investigation of bubble-induced free convection in a small electrochemical cell," *Journal of Applied Electrochemistry*, vol. 30, pp. 767–775, 07 2000.

[35] Pang, X., et al., "Framework for evaluating the performance limits of membraneless electrolyzers," *Energy & Environmental Science*, vol. 13, pp. 3663–3678, 07 2020.

[36] G. Vliet and D. Ross, "Turbulent natural convection on upward and downward facing inclined constant heat flux surfaces," *Heat Transfer*, 1975.

[37] N. Hawkes, "Hydrostatics," in *Thermopedia*, Begel House Inc., 2011.

[38] T. Weier and S. Landgraf, "The two-phase flow at gas-evolving electrodes: Bubble-driven and lorentz-force-driven convection," *THE EUROPEAN PHYSICAL JOURNAL*, vol. 220, pp. 313–322, 2013.

[39] Riegel, H. et al., "Role of mass transfer on hydrogen evolution in aqueous media," *Journal of Applied Electrochemistry*, vol. 28, pp. 10–17, 1998.

[40] H. Vogt, "The instability problem of the bubble street in vertical interelectrode gaps," *PHYSICOCHEMICAL HYDRODYNAMICS*, vol. 8, no. 4, pp. 373–382, 1987.

[41] Vogt, H., "Instability of the two-phase flow in vertical interelectrode gaps," *Journal of Applied Electrochemistry*, vol. 29, pp. 1155–1159, 1999.

[42] L. Sigrist, "Verfahrenstechnische aspekte von elektrolysezellen mit stark gasenden elektroden," *diss.*, 1978.

[43] Alexiadis, A., Dudukovic, M.P., Ramachandran, P. et al., "On the stability of the flow in multi-channel electrochemical systems," *J Appl Electrochem*, vol. 42, pp. 679–687, 2012.

[44] Alexiadis, A., Dudukovic, M.P., Ramachandran, P. et al., "Transition to pseudo-turbulence in a narrow gas-evolving channel," *Theor. Comput. Fluid Dyn.*, vol. 26, pp. 551–564, 2012.

[45] K. T. Møller, T. R. Jensen, E. Akiba, and H.-w. Li, "Hydrogen-a sustainable energy carrier," *Progress in Natural Science: Materials International*, vol. 27, no. 1, pp. 34–40, 2017.

[46] K. Aldas, N. Pehlivanoglu, and M. D. Mat, "Numerical and experimental investigation of two-phase flow in an electrochemical cell," *International journal of hydrogen energy*, vol. 33, no. 14, pp. 3668–3675, 2008.

[47] Y. Huang, P. Leblanc, and V. Apostolou, "Comparison of milli-q pf plus water to," *Biotechniques Billing Exempt*, vol. 19, pp. 656–661, 1995.

[48] Industrial Specialties Mfg. & IS Med Specialties, "Acrylic aka pmma chemical compatiblity chart." https://www.industrialspec.com/resources/acrylic-aka-pmma-chemical-compatiblity-chart, 2015. Accessed: 2023-08-01.

[49] United Nations, "Veco Precision, world leader in Electroforming." https://www.vecoprecision.com/, Accessed on: 27-3-2023.

[50] Photron, "FASTCAM NOVA S-Series." https://photron.com/fastcam-nova-s, Accessed on: 01-06-2023.